Frazil Ice Formation in the Polar Oceans

Nikhil Vibhakar Radia

Department of Earth Sciences, UCL

A thesis submitted for the degree of Doctor of Philosophy

Supervisor: D. L. Feltham

August, 2013

I, Nikhil Vibhakar Radia, confirm that the work presented in this thesis is my own. Where information has been derived from other sources, I confirm that this has been indicated in the thesis.

SIGNED

Abstract

Areas of open ocean within the sea ice cover, known as leads and polynyas, expose ocean water directly to the cold atmosphere. In winter, these are regions of high sea ice production, and they play an important role in the mass balance of sea ice and the salt budget of the ocean. Sea ice formation is a complex process that starts with frazil ice crystal formation in supercooled waters, which grow and precipitate to the ocean surface to form grease ice, which eventually consolidates and turns into a layer of solid sea ice. This thesis looks at all three phases, concentrating on the first. Frazil ice comprises millimetre-sized crystals of ice that form in supercooled, turbulent water. They initially form through a process of seeding, and then grow and multiply through secondary nucleation, which is where smaller crystals break off from larger ones to create new nucleii for further growth. The increase in volume of frazil ice will continue to occur until there is no longer supercooling in the water. The crystals eventually precipitate to the surface and pile up to form grease ice. The presence of grease ice at the ocean surface dampens the effects of waves and turbulence, which allows them to consolidate into a solid layer of ice. The ice then mostly grows through congelation ice forming beneath the layer of ice. A mathematical model describing the above processes is formulated and used to simulate ice growth. The model consists of conservation equations for mass and heat, with an imposed momentum budget. Simulations are realistic and numerical sensitivity experiments are used to investigate the dependence of ice growth on the ambient environment.

Acknowledgements

First and foremost I want to thank my supervisor, Prof. Daniel Feltham, whose support and guidance was invaluable. Even when times were tough, I always came out of our meetings feeling like the work was worthwhile and that we were making good progress.

I would also like to thank my fellow PhD colleagues, who understood the difficulties of undertaking a PhD and helped keep me motivated. Their interest in the field was inspiring.

I could not have completed this work without my partner David, who kept me grounded throughout my research.

Finally I want to thank my family and friends for their support and love.

Contents

1 Introduction

1.1 Overview

The Earth is warming at a faster rate than it has done in recent history, and this is happening more rapidly at the poles. The 2007 IPCC Report documents evidence that the linear warming trend of the 50 years to 2005 was twice that of the trend of the 100 years to 2005.

Global Climate models are mathematical models that are used to simulate the Earth's climate, and are made up of many components including AGCMs (atmospheric GCMs) and OGCMs (oceanic GCMs), which are coupled. Other components that can be present describe sea ice, which is frozen seawater and will be described at length further on, and the land surface. The oceanic and atmospheric components are based on the Navier-Stokes equations for fluid flow, and include other fluid dynamical, chemical and biological equations. We will mostly be interested in the sea ice component, and its effect on the ocean and the atmosphere.

In the Arctic, most GCMs have underoverestimated the sea ice summer ice extent minimum in recent times (Fig. 1.1). Miller et al (2006) found that the uncertainty in stand-alone sea ice models is enough to account for the model-data discrepancies. This strongly suggests that more work needs to be carried out on the sea ice models, and this motivates the research carried out for this thesis, which is specifically about lead and polynya refreezing and frazil ice formation. Leads and polynyas are open ocean areas in the sea ice cover which are in direct contact with the atmosphere and are known to be regions of high frazil ice production.

1.2 Sea Ice in the climate system

At any one time, sea ice covers approximately 7% of the ocean, and affects the dynamics and thermodynamics of the ocean and the atmosphere (Houghton et al 1997). The Arctic

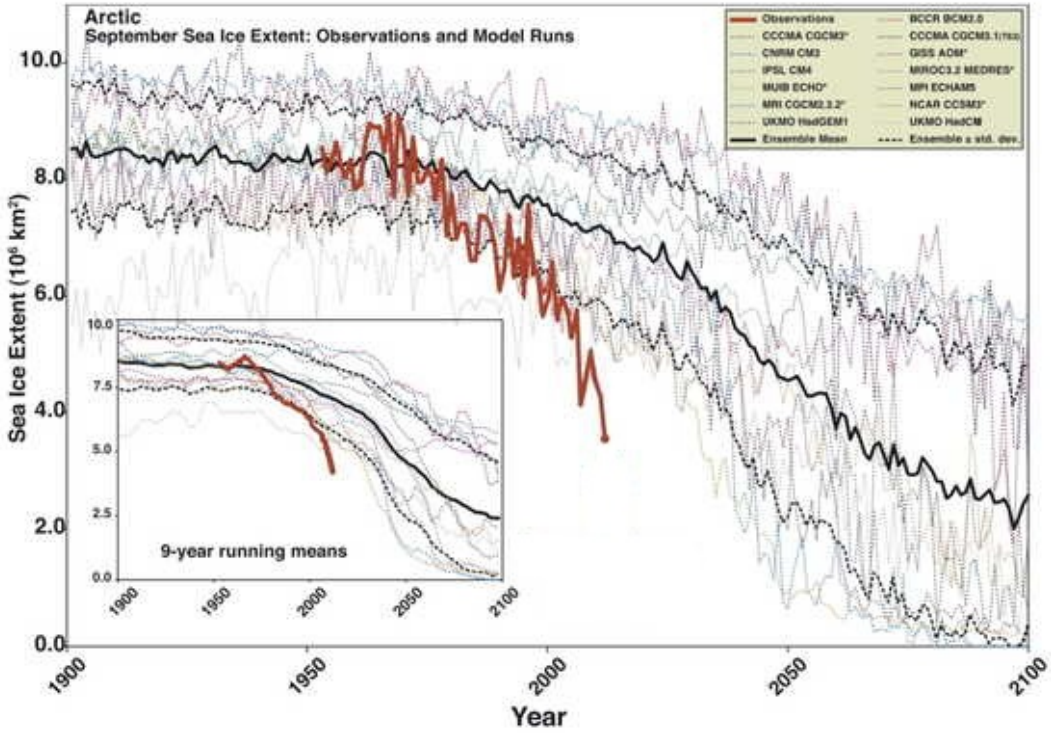

Figure 1.1: Observations of September Arctic sea ice extent (thick red line), and 13 models, with the mean (thick black line), and the standard deviation of the models (dashed black line).

ocean can be entirely covered in sea ice, whilst in the Antarctic sea ice can only be present around Antarctica. The sea ice extent of both the Arctic and the Antarctic varies greatly from the summer to the winter, due to its melting and freezing. Each year the summer sea ice extent minimum of both the Arctic and the Antarctic are recorded, and it is the decrease in the Arctic, which has seen a rapid decline in recent years, culminating in the 2012 Arctic sea ice extent minimum.

Figure 1.2: Average Monthly Arctic Sea Ice Extent - September 1979 to 2012 (NSIDC)

Satellite data since 1978 has shown that the average annual Arctic sea ice extent has decreased by 2.7% per decade, with the largest decrease in summer (7.4%). Fig. 1.2 shows the decline of the average September sea ice extent from 1979 to 2012, with the trend in blue clearly showing the decline. If we continue to lose sea ice at the same rate, we could have a ice-free Arctic summer within a few decades (NSIDC).

Sea ice can be split into first year and multi-year sea ice. First year ice is no longer than one year old, and multi-year ice is ice that has survived one or more years. First year ice forms in the region known as the seasonal ice zone, which is the area that changes between being solid in winter and liquid in summer. Multi-year ice exists all year round. First year ice is generally thinner than multi-year ice, but multi-year ice is fresher.

Sea ice affects the rest of the polar regions and consequently the Earth's climate in several ways, some of which we will now describe. Albedo is a measure of the reflectivity of a surface, and the albedo of sea ice (0.5-0.7) is higher than that of open water (0.06). This means that more energy is reflected off the surface of the sea ice than off the surface of the water. Melting sea ice is a component of the positive albedo feedback mechanism: when sea ice melts, the albedo of the surface decreases, leading to more heat being absorbed by the ocean and consequently more sea ice melting. If sea ice melts at the edge, it runs off into the ocean, but surface melt can result in melt ponds being formed. These are areas within the sea ice cover covered in relatively fresh water caused by melting sea ice and snow, and can cover up to 50% of the Arctic cover (Flocco & Feltham 2007).

Figure 1.3: The Great Ocean Conveyor Belt (Watson, 2001)

Another way in which the presence of sea ice affects the global climate is the effect on the thermohaline circulation (figure 1.3), which is an overturning circulation in which warm water flows poleward near the surface and is subsequently converted into cold water that is denser and so sinks and flows equatorward in the interior (Toggweiler & Key, 2003). The thermohaline circulation is responsible for transporting heat around the oceans, through the polar regions where it is affected by the melting and freezing of sea ice. Drastic changes in the amount of sea ice in the Arctic may have a great effect on this process, since more

sea ice melting in the Arctic will make the water less dense and so it will not sink as deep and circulate at depth as easily. This could disrupt the downwelling and could even stop it completely.

One more way in which the presence or lack of sea ice affects the global climate is that it acts as an insulating layer between the ocean and the atmosphere, and with less sea ice present the fluxes between these two increases, hence warming the atmosphere and cooling the water or vice-versa. Leads and polynyas are areas in the sea ice cover in which the open ocean is in contact with the atmosphere, and although they represent only 3-4% of the sea ice cover, they are estimated to be responsible for about half of the heat loss (Maykut 1982).

1.3 Sea Ice Growth

Sea water has a typical salinity of 35 psu (practical salinity units) and freezes at about -1.8°C to form sea ice. Sea ice is a complex mixture of ice crystals, brine pockets and air pockets. The first stage of sea ice formation involves frazil ice, which are millimetre-sized crystals (typical size of 0.1-4 mm diameter and 1-100 µm thickness) which form in super-cooled turbulent water (Kivisild 1970).

When frazil ice precipitates to the ocean surface, the mixture of frazil and water is called grease ice. The evolution of grease ice, as shown in table 1, depends on mixing. In calm conditions, a thin layer (<10 cm) of ice forms at the surface due to the rising and agglomeration of the crystals in the water, known as nilas. In turbulent or windy conditions, the frazil ice congeals into pancake ice, which are circular blocks of ice which form in this way due to collisions with each other, and can be up to 3–5 m in diameter and 50–70 cm thick (Weeks & Ackley 1986). Both nilas and pancake ice eventually form a layer of young ice which is thicker than 10 cm. From this, ice growth happens downwards from beneath the ice layer, known as congelation ice

Since pure ice has zero salinity, when sea ice is forming, the salt from the water is

Table 1: Evolution of frazil ice in natural bodies (Daly, 1994)

rejected into the surrounding water. As a consequence, the water around the ice crystals becomes saltier and hence has a lower freezing temperature. Some of this water can become trapped to form pockets of brine within the sea ice which have high salinity and hence remain liquid. Once the ice is thick enough, due to differences of density between the brine in the pockets and the ambient water beneath, these pockets can form channels and release the brine into the water below the ice. This, together with the salt being released directly at the sea ice bottom, contribute to the desalination of sea ice.

1.3.1 Frazil Ice

Two areas of interest within the sea ice cover with which we are concerned are leads and polynyas. These are ice-free areas within the sea ice cover in which the ocean is in contact with the cold atmosphere, and they can form due to warm water upwelling (sensible heat polynya), katabatic winds or ocean currents which drive new formed ice away (latent heat polynyas) or when the ice breaks due to internal stresses (leads). They are areas of rapid frazil ice production in winter, due to the large heat fluxes from the water, which is close to the freezing temperature, to the air, which is normally a lot colder.

The formation of the initial frazil ice crystals is an area of some discussion. It is gener-

ally agreed that nucleation is not homogeneous, since this has been shown to happen only when supercooling reaches 40 ℃ (Mossop 1955). Field observations of frazil ice formation have found that the most supercooling that will ever occur before the onset of frazil ice is about 0.1 ℃ (Carstens 1966, Osterkamp et al 1973), so there must be another way to explain nucleation. Another possible theory is that since sea water has impurities, organic and inorganic, these may act as nucleii, and it was shown that silver iodide nucleates with a supercooling of about 3 to 4 ℃ (Fletcher 1968), and some bacteria can nucleate at supercooling of about 1 ℃ (Lindow et al 1978). These values are still too high to explain nucleation. The accepted theory is that the initial nucleus is an ice crystal which is introduced into the water. The crystal can come from water vapour sublimating as it encounters cold air (Osterkamp et al 1974), or drops of water which are ejected into the air, and freeze before they drop back into the water (Gosink & Osterkamp 1986).

The shape of frazil ice crystals has been observed and studied (Kumai & Itagaki 1953, Arakawa 1955, Williamson & Chalmers 1966), and most studies have found that the crystals take the form of a disk. While they can start out in the shape of six-pointed stars, hexagonal plates, spheres, or dendritic ice, they all evolve into disk shapes in turbulent water (Daly 1994). The size of the crystals has been observed to be in the range of 0.05 mm to several millimeters (Daly & Colbeck 1986). Experiments have shown that the crystal becomes unstable if the diameter or the supercooling is too large, and hence there is a limit on the maximum crystal size.

Once there is an initial seed, the number of frazil crystals may grow quickly through secondary nucleation, also known as collision breeding. This process breaks smaller ice crystals off from larger ones through collisions, either between two larger crystals or between crystals and hard surfaces. The new smaller crystals then act as new nuclei for crystal growth. This creates a positive feedback process, since a higher number of crystals will create more collisions.

The other process contributing to frazil formation directly is crystal growth. If the wa-

ter is supercooled, the ice crystals grow to quench the supercooling, releasing latent heat, and increasing the ice volume concentration. Conversely, if the water is not supercooled, the crystals melt, decreasing ice volume concentration. Both crystal growth and secondary nucleation contribute to the increase of frazil ice until the water temperature reaches the freezing temperature.

1.4 Sea Ice Models

Sea ice models are based on dynamic and thermodynamic equations, and are solved using finite difference methods. In the last decade or so, several climate model sea ice components have been created, such as Fichefet & Morales Maqueda (1997), Bitz et al (2001), Zhang & Rothrock (2003) and Hunke & Lipscomb (2004). Comparison studies between GCMs have shown that there are still large differences in the sea ice predictions of different climate models (Stroeve et al, 2007).

Sea ice thermodynamics are controlled by the heat flux at the ice-ocean interface and the ice-air interface, penetration of solar radiation into the snow/ice, conduction of heat inside the snow and ice, melting and freezing, and the vertical transport of liquid water and moist air in the snow pack (Vihma & Haapala, 2009). Dorn et al (2007) noticed how simplifications in the thermodynamic component of their coupled model may have lead to overestimation in the amount of ice.

In the first stages of new ice formation, most models assume a thin layer of ice forms which then grows (Maykut 1986, Lepparanta 1993). However, in the ocean, most initial ice formation is related to frazil ice formation. Studies on cold seas during the last decades have demonstrated its importance. The major sea ice forming process in the Wedell Sea, Antarctica, is due to frazil ice that is transformed to pancake ice at the surface (Wadhams et al 1987) and in leads, polynyas and the ice edge, frazil ice is the main process of ice formation (Ushio & Wakatsuchi 1993, Wadhams et al 1996). Recently, more complex frazil ice models have been developed including Jenkins & Bombosch 1995 (JB), Svensson &

Omstedt 1998 (SO), Smedsrud & Jenkins 2004 (SJ) and Holland & Feltham 2005 (HF).

1.5 Thesis Objectives and Structure

The main objective of this PhD is to create a model of frazil ice formation in leads and polynyas and build upon previous models with new formulations of the processes involved, and compare the results with experiments and observations. The main model I will be using as a basis will be the Holland & Feltham model, which is of frazil ice formation beneath an ice shelf. Since we are now dealing with leads and polynyas, most of the new elements of the model will relate to the surface of the water and the different thermodynamics there.

In chapter 2, we will describe the mathematical model of ice growth in full, including all the formulations and assumptions. This is split into the different stages, starting with frazil ice forming in open water, followed by the grease ice layer, and finally congelation ice growth and desalination of ice once we have a full cover.

Chapter 3 is based entirely on the model of Holland & Feltham and is a very simplistic approach, where we consider the domain to be well-mixed and only consider the frazil crystal dynamics. It is an important exercise to check whether the model is behaving as expected at the most basic level of crystal growth/melting. We also include a study of some experimental results compared to results from our model.

Chapter 4 presents the full results of our new model with all new formulations included. Plots are shown for ice concentration, water temperature and salinity throughout the entire run, and we end the run with a considerable amount of thick congelation ice. We finish by looking at a study of observations of frazil ice formation and try to recreate the same scenario with our model to compare the results.

In Chapter 5 we include sensitivity studies where we choose a selection of parameters to vary and compare the results to a reference run to deduce the relevance of these parameters

to ice growth.

We conclude, in chapter 6, with a summary of our main research results and short discussion of their implications.

2 A Model of Frazil Ice and Sea Ice Growth

We will now describe some previous frazil ice models. We will then describe in detail the equations used in our model, and some parameterizations of physical processes which are included in the model.

2.1 Frazil Ice Models

2.1.1 Svensson & Omstedt (1994) and Svensson & Omstedt (1998)

The Svensson & Omstedt (1994) model is a zero dimensional, well-mixed model which includes a crystal number continuity equation with the following processes included: initial seeding (when the first ice crystals are formed), secondary nucleation (where new crystal nucleii are formed from collisions between crystals), crystal rising (the effect of gravity on the ice crystals which forces them towards the surface), crystal growth/melting (when ice crystals grow/melt due to the water being supercooled or not) and flocculation/break up (where crystals break up and form smaller crystals). These equations are formulated with a resolution in time and crystal radius. The crystals are split into N different size classes and the parameterization of the secondary nucleation and flocculation/break up terms include parameters which are then used to calibrate the model. The crystal rise velocities are taken from Daly (1984). To validate the model, they used experiments by Hanley & Michel (1977), specifically their measurements of the relation between time to maximum supercooling and surface cooling (also known as supercooling curves), and the results were in agreement. They also used preliminary results from Daly (1992) of mean radius and number of crystals, and found that the maximum value of the mean diameter and the rapid increase in the number of crystals after the maximum supercooling were common features.

The Svensson & Omstedt (1998) model was an extension of the 1994 model which included some new formulations. The model was one dimensional in space, occupying the Ekman layer. The water turbulence was modelled with a 2-equation system for calculating turbulent diffusivity coefficients. Some conclusions from this model were that a large number of ice crystals are formed in suspension in the ocean during freezing, but they

only represent a small volume of ice at the surface, and that smaller crystals mix deeper, whereas larger crystals are found only at the top, close to the surface.

2.1.2 Jenkins & Bombosch (1995)

The Jenkins & Bombosch model is of frazil ice formation under an ice shelf, and models the ocean as a two-layer system, with turbulent ISW (ice-shelf water) above an ambient water mass. The aim of the model is to show how the formation of ice crystals within the ISW plume influences the dynamics and thermodynamics of the plume. The properties of the plume are averaged and the equations are reduced to one dimension by depth integration.

The processes modelled are: entrainment rate from the ambient water to the ISW plume, the melt rate at the ice-ocean interface, the diffusion of heat and salt towards and away from the ice-ocean interface, the freezing and melting of ice crystals, and the deposition of ice crystals from the turbulent suspension, also known as crystal precipitation. The size of the ice crystals is used as the calibration paramater, and sensitivity studies were carried out for several of the parameters used in the model. The results from the simulations showed that the addition of frazil ice in the plume has a thermodynamic effect, by keeping the supercooling very low since the growing crystals release latent heat, and a dynamic effect, since crystals in suspension give the plume more buoyancy, which affects the plume velocity.

2.1.3 Smedsrud & Jenkins (2004)

The Smedsrud & Jenkins model is also a model of frazil ice formation beneath an ice shelf, and also treats the ocean as a two-layer system with an ISW plume above ambient water. It is well-mixed and the plume is defined by its depth, and depth-averaged quantities velocity, temperature and salinity. The new addition to this model is the use of different sized crystals. The crystals are modelled as circular disks which are characterized by their radius and thickness, and they range from 0.01 mm to 4 mm. The frazil ice formation model used is that of Jenkins & Bombosch (1995).

2.1.4 Holland & Feltham (2005)

The Holland & Feltham model is of frazil ice formation beneath an ice shelf, but it models the frazil ice crystals more explicitly than previous ice shelf models (JB & SJ). Similarly to SO, it splits frazil crystals into N size classes and assigns a radius and respective volume to each one. One of the new elements in this model is the use of depth dependence, which affects the freezing temperature and hence the crystal formation dynamics. Similarly to JB, the model also uses the balance between buoyancy of frazil ice crystals and the turbulence of the water surrounding the crystals to calculate the rate of crystals settling on to the surface under the ice shelf, except it also takes into account whether the water flow beneath the ice shelf is turbulent or laminar, and includes a parameterization for each case. The parameterizations are then merged to give a new equation for frazil ice precipitation which depends on the Reynolds number to decide whether the flow is turbulent or laminar.

The model we will describe in the next section is based on this model, but since we are now dealing with leads and polynyas, we will adapt the model to the upper layers of the open ocean. This will force us to reconsider processes which until now have been ignored, such as the heat fluxes at the surface and the effect of salinity on the growing ice, and revisit the definitions of other processes, such as the frazil precipitation.

We will now derive the governing equations of the model, and then the physical processes involved and their equivalent mathematical formulations.

2.2 The Frazil Ice Model and Sea Ice Growth Model used in this thesis

Our model is one dimensional, occupies the ocean surface mixed layer and is made up of several elements (figure 2.1). We have the frazil ice equations, which include the ice crystal formation, the water temperature and the water salinity equations. These are defined by balance equations for mass, heat and salt, respectively. Since they are all linked, we have a system of partial differential equations with initial and boundary conditions for each one.

The boundary conditions for the ice fraction includes the ice precipitation equations at the surface, and a zero-flux at the bottom of the mixed layer. The boundary conditions for the heat equation include the release of heat at the surface of the water, which is also a heat balance equation, and the boundary condition for the salt is initially zero-flux at the surface and bottom, but once the ice grows thick enough is made up of salt being release from brine channels and being released from ice growth. The initial conditions for all three are prescribed and are based on observations or previous models.

Another element to the model is the formation of grease ice, which is the stage that proceeds frazil formation. The equations for this stage describe the area fraction of grease ice and the ice fraction growing in the grease ice layer until the concentration is high enough that we can consider it a mushy layer (so that it can be treated as congelation ice).

Once we have reached this stage, we use the mushy layer equations to grow the ice from beneath, which includes heat loss through the ice, and salt release into the water beneath by growing ice and the formation of brine channels.

We will now describe the model in full detail.

2.2.1 Frazil Ice Equations

We consider a mixture of frazil ice and seawater with density ρ_m defined by

$$\rho_m = \rho_i C + \rho_s(1 - C), \tag{2.2.1}$$

where C is the frazil ice volume concentration of the mixture, ρ_i is the density of ice and ρ_s is the density of seawater determined by

$$\rho_s = \rho_0[1 + \beta_s(S - S_0) - \beta_t(T - T_0)], \tag{2.2.2}$$

where ρ_0, S_0 and T_0 are reference density, salinity and temperature. β_s and β_t are expansion coefficients of salinity and temperature respectively.

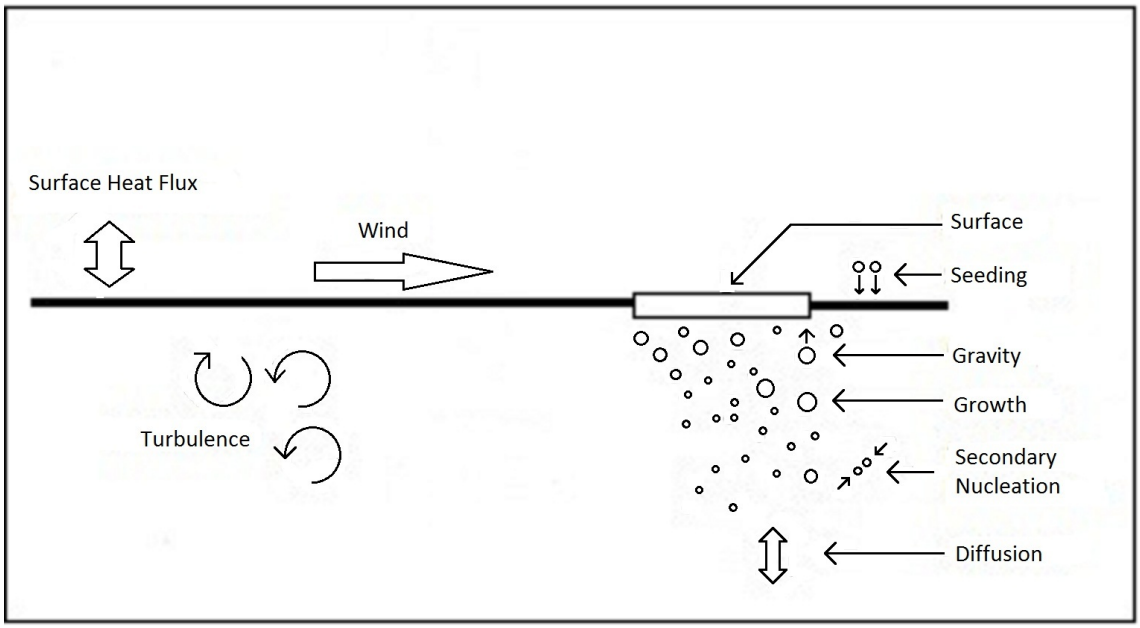

Figure 2.1: Sketch of frazil processes involved.

We define N_{ice} different size classes of crystals. By discretizing the crystal sizes, we simplify the problem of growth and melting of crystals as simply moving between size classes. The total concentration is

$$C = \sum_{i=1}^{N_{ice}} C_i, \tag{2.2.3}$$

where C_i is the volume concentration of frazil ice in size class i.

Applying the Boussinesq approximation to the seawater, which assumes that the effect of temperature and salinity on the density of the water is negligible (except for buoyancy), we set $\rho_s = \rho_0$ in equation (2.2.1), so it becomes

$$\rho_m = \rho_i C + \rho_0(1 - C). \tag{2.2.4}$$

Now, considering the conservation of mass equation of the mixture, we get

$$\frac{\partial \rho_m}{\partial t} + \nabla \cdot (\rho_m \boldsymbol{u}) = 0, \tag{2.2.5}$$

and replacing for equation (2.2.4), we get

$$\frac{\partial \rho_i C}{\partial t} + \frac{\partial \rho_0 (1-C)}{\partial t} + \nabla \cdot (\rho_i C \boldsymbol{u}) + \nabla \cdot [\rho_0 (1-C) \boldsymbol{u}] = 0. \tag{2.2.6}$$

Separating this into seawater and frazil ice parts, we get

$$\frac{\partial \rho_i C}{\partial t} + \nabla \cdot (\rho_i C \boldsymbol{u}) = 0, \tag{2.2.7}$$

and

$$\frac{\partial \rho_0 (1-C)}{\partial t} + \nabla \cdot (\rho_0 (1-C) \boldsymbol{u}) = 0. \tag{2.2.8}$$

Considering the effects of buoyancy, turbulent mixing, and growth/melting of crystals, we can rewrite these as

$$\frac{\partial \rho_i C}{\partial t} + \nabla \cdot (\rho_i C \boldsymbol{u}) + \sum_{i=1}^{N_{ice}} \rho_i w_i \frac{\partial C_i}{\partial z} = \nabla \cdot (\mu_T \nabla C) - \rho_0 w', \tag{2.2.9}$$

and

$$\frac{\partial \rho_0 (1-C)}{\partial t} + \nabla \cdot (\rho_0 (1-C) \boldsymbol{u}) + \sum_{i=1}^{N_{ice}} \rho_i w_i \frac{\partial (1-C_i)}{\partial z} = \nabla \cdot [\mu_T \nabla (1-C)] + \rho_0 w', \tag{2.2.10}$$

where z is the vertical coordinate, defined as downwards depth, w_i are the buoyancy rising velocities of the different size classes, μ_T is the turbulent eddy coefficient for both water and ice, and w' is defined as the net volume discharge of water released due to crystal melting, hence being negative in the ice equation and positive in the water equation.

We are now mainly interested in the frazil ice component, so by using the Boussinesq approximation again, we can write

$$\nabla \cdot \boldsymbol{u} = 0 \tag{2.2.11}$$

and so the i^{th} component of equation (2.2.9) becomes

$$\frac{\partial C_i}{\partial t} + \boldsymbol{u} \cdot \nabla C_i + w_i \frac{\partial C_i}{\partial z} = \nabla \cdot (\nu_T \nabla C_i) + S_i \tag{2.2.12}$$

where $\nu_T = \mu_t/\rho_i$, and S_i is the interaction term between the different crystal size classes.

Equation (2.2.12) is then our balance equation of the volume of frazil ice per unit volume of mixture.

2.2.2 Temperature Equation

We start by defining the equation of conservation of water-fraction heat per unit volume of mixture as

$$\frac{\partial}{\partial t}[(1-C)T] + \nabla \cdot [(1-C)\underline{u}T] + T\frac{\rho_I}{\rho_0}\sum_{i=1}^{N_{ice}} w_i \frac{\partial(1-C_i)}{\partial z} = \nabla \cdot (\nu_T \nabla [(1-C)T]) - \frac{Q_T}{\rho_0 c_0} \tag{2.2.13}$$

where the terms represent, in order, the rate of change of temperature in the fluid, the advection of heat by the fluid, the advection of heat by crystal rising, the turbulent mixing in the fluid and the source term of heat due to freezing and melting of ice. Applying equation (2.2.10), we arrive at the equation of conservation of heat in the water fraction per unit volume

$$(1-C)\frac{\partial T}{\partial t} + (1-C)\underline{u} \cdot \nabla T = (1-C)\nabla \cdot (\nu_T \nabla T) - 2\nu_T \nabla T \cdot \nabla C - w'T - \frac{Q_T}{\rho_0 c_0}. \tag{2.2.14}$$

The heat sink/source Q_T is made up of sensible heat, which is a heat transfer associated with a change in temperature of the water, and latent heat, which is a heat transfer associated with a change in the state of the water. We then define Q_T as

$$Q_T = \rho_0 c_0 (1-C) \sum_{k=1}^{n} \gamma_{Tk}^{c} (T - T_c)\alpha_k - \rho_0 c_0 w' T_c \tag{2.2.15}$$

where the first term on the RHS is the parameterization of sensible heat, and the second term on the RHS is that of latent heat. n is the number of ice crystals of all sizes in the unit volume, γ_{Tk}^{c} is the heat transfer coefficient and α_k is the surface area per unit volume of the kth crystal, and T_c is the temperature of all frazil crystals, which is set to the water freezing temperature.

Similarly to the ice concentration parameterization, we can assume that since $C \ll 1$, and $1-C \approx 1$, then in equation (2.2.14), we can ignore the fourth term since it is negligible compared to the third term. The equation then becomes

$$\frac{\partial T}{\partial t} + u \cdot \nabla T = \nabla \cdot (\nu_T \nabla T) + w' \left(T_f - T - \frac{L}{c_0} \right) \tag{2.2.16}$$

which is our balance equation of the water temperature.

2.2.3 Salinity Equation

We start from the equation of conservation of salt in the water, assuming that when frazil crystals form they release all the salt from that volume. Salt per unit mixture is:

$$\frac{\partial}{\partial t}[(1-C)S] + \nabla \cdot [(1-C)\underline{u}S] + S\frac{\rho_I}{\rho_0} \sum_{i=1}^{N_{ice}} w_i \frac{\partial (1-C_i)}{\partial z} = \nabla \cdot (\nu_T \nabla [(1-C)S]) \tag{2.2.17}$$

where the terms represent in order, the rate of change of salt in the fluid, the advection of salt in the fluid, the advection of salt in fluid due to crystal rising and the turbulent mixing of salt in the fluid. Once again, using equation (2.2.10) we get

$$(1-C)\frac{\partial S}{\partial t} + (1-C)\underline{u} \cdot \nabla S = (1-C)\nabla \cdot (\nu_T \nabla S) - 2\nu_T \nabla S \cdot \nabla C - w'S. \tag{2.2.18}$$

Now, since $C \ll 1$, we can assume that $1 - C \approx 1$ and we can ignore the fourth term in (2.2.18) since this term will always be negligible compared to the third term. This simplifies the equation to

$$\frac{\partial S}{\partial t} + u \cdot \nabla S = \nabla(\nu_T \nabla S) - w' S, \tag{2.2.19}$$

which is our balance equation of the water salinity.

2.2.4 Frazil Interaction Term

We now describe the term S_i from equation 2.2.12. The crystals are modelled as being circular disks with a constant ratio of radius to thickness, so we can define their size with one parameter only, radius (r). To simplify our model, we split the concentration into N_{ice} size classes. This way we can model crystal growth (G_i), melting (M_i) and secondary nucleation (N_i) as movement between different size classes (Fig. 2.2). Holland & Feltham carried out sensitivity studies on N_{ice}, the number of size classes, and found that the results of simulations were qualitatively similar for $N_{ice} = 10$ and $N_{ice} = 200$, and so we continue to use $N_{ice} = 10$. Following numerical experiments, we set our radii range from 0.01 to 2 mm (0.01, 0.02, 0.05, 0.1, 0.2, 0.3, 0.5, 0.8, 1, 2 mm).

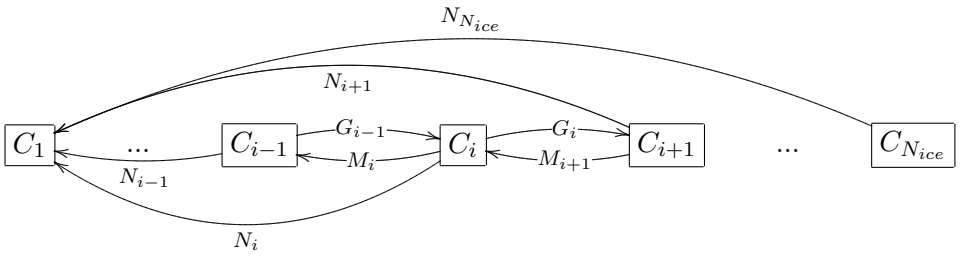

Figure 2.2: Schematic of growth, melting and secondary nucleation

As we are assuming that the crystals have a constant thickness to radius ratio (a_r), we can define the crystal volume v_i by

$$v_i = \pi r_i^2 t_i, \tag{2.2.20}$$

where $t_i = a_r r_i$ is the thickness of a crystal with radius r_i.

The interaction term of size class i is defined by the difference between the sources: melting from size class $(i+1)$ and growth from size class $(i-1)$, and the sinks: melting and growth from size class i. Since the different size-class crystals have different volumes, we must account for this when transferring crystals, and so if a crystal in size class (i) of volume v_i grows and enters class $(i+1)$, then crystal growth in term C_i must be at least $\Delta v_i = v_{i+1} - v_i$ to transfer one crystal to size class $(i+1)$. We can then define the interaction term as

$$S_i = \frac{v_i}{\Delta v_{i-1}}[(1-H)M_i + HG_{i-1}] - \frac{v_i}{\Delta v_i}[(1-H)M_{i+1} + HG_i] + N_i, \tag{2.2.21}$$

where $H = He(T_f - T)$ is to account for the different cases of $T < T_f$ (supercooled) and $T > T_f$ (not supercooled), where He, the Heaviside function, is defined as

$$He(x) = \begin{cases} 1\ , x > 0 \\ 0\ , x \leq 0 \end{cases} \tag{2.2.22}$$

We also impose that $v_0 = v_{N_{ice}+1} = G_0 = G_{N_{ice}} = M_{N_{ice}+1} = 0$

We now define the growth/melting (G_i/M_i) and secondary nucleation (N_i) terms.

2.2.5 Crystal Growth/Melting

The main assumption we make is that crystal growth occurs solely at the crystal edge, but crystal melting occurs all over, so the formulations differ. This is because experiments have shown that growth rate at the edges is 1-2 orders of magnitude larger than growth rate in the thickness, and yet melting rate is the same at the edge and faces (Daly 1994b).

We also know that the formation of frazil ice affects the salinity of the ambient water, which in turn affects the freezing temperature close to the crystal since salt diffuses slower than heat. We will however assume that the frazil formation is controlled solely by the heat flux, and so is related linearly to $T - T_f$, where T_f is calculated using the bulk salinity

of the water. The heat flux from a growing crystal of radius r_i is given by

$$q_g^i = \rho_0 c_0 Nu K_T \frac{T_f - T}{r_i} 2\pi r_i t_i \tag{2.2.23}$$

where c_0 is the specific heat capacity, Nu is the Nusselt number, K_T is the molecular thermal diffusivity, T_f and T are the freezing and water temperatures, and $2\pi r_i t_i$ is the surface area of the disk edge.

The total heat flux from all crystals in the ith size class is $q_g^i n_i$, where n_i is the number of crystals in that size class per unit volume. Converting this heat into an ice volume production gives

$$G_i = \frac{q_g^i n_i}{L\rho_0} \tag{2.2.24}$$

and applying (2.2.23) and $C_i = \pi r_i^2 t_i n_i$ gives

$$G_i = \frac{c_0 Nu K_T}{L}(T_f - T)\frac{2}{r_i^2} C_i. \tag{2.2.25}$$

Similarly for crystal melting, the heat flux from a melting crystal is given by

$$q_m^i = \rho_0 c_0 Nu K_T \frac{T_f - T}{r_i}(2\pi r_i t_i + \pi r_i^2), \tag{2.2.26}$$

and converting this into an ice melt rate gives

$$M_i = \frac{c_0 Nu K_T}{L}(T_f - T)\frac{2}{r_i}(\frac{1}{r_i} + \frac{1}{t_i}) C_i. \tag{2.2.27}$$

2.2.6 Secondary Nucleation

As mentioned earlier, secondary nucleation is the process through which new crystals are formed and is essential in the production of frazil ice. It typically occurs when crystals collide and a new crystal breaks off becoming the nucleus of a new crystal.

An assumption made in this formulation is that any new crystals formed through col-

lisions are inserted into the smallest size class. This simplifies the model since secondary nucleation becomes a source term for the smallest size class, and a sink term for all the rest.

The volume swept by a crystal in the ith size class in time Δt is

$$\Delta V = W_i \pi r_i^e \Delta t, \tag{2.2.28}$$

where r_i^e is the effective crystal radius, which is the radius of a sphere with the same volume of the crystal. We use r_i^e to account for the fact that we do not know the direction the crystal travels in. It is defined as

$$\frac{4}{3}\pi r_i^{e^3} = \pi r_i^2 t_i. \tag{2.2.29}$$

W_i is the crystal velocity, which is made up of turbulent and rising motions and is defined as

$$W_i^2 = \frac{4\epsilon}{15\nu_0} r_i^{e^2} + w_i^2, \tag{2.2.30}$$

where ϵ is the turbulent dissipation rate, v_0 is the molecular viscosity of sea water, and w_i is the rising velocity. Defining n_i to be the number of crystals in the ith size class, the total volume swept by all crystals in that size class per unit time is given as

$$n_i \frac{\Delta V}{\Delta t} = n_i W_i \pi r_i^{e^2}, \tag{2.2.31}$$

but $C_i = n_i \frac{4}{3}\pi r_i^{e^3}$ and so this becomes

$$n_i \frac{\Delta V}{\Delta t} = \frac{3}{4}\frac{W_i C_i}{r_i^e}. \tag{2.2.32}$$

So we then define the probability of a collision between any crystal in the ith size class and any other crystal as

$$N_i = a_{nuc}\frac{W_i C_i C_T}{r_i^e}, \tag{2.2.33}$$

where a_{nuc} is a calibration parameter which can be interpreted as the efficiency of a collision creating a new crystal, and $C_T = \sum_{i=1}^{N_{ice}} C_i$ is the total ice concentration. We will vary a_{nuc} later and use experimental work to determine a value for it.

2.2.7 Frazil Precipitation

Frazil crystals which are in suspension eventually rise to the surface and enter a viscous sublayer where they are assumed to remain and not re-enter the water domain. We call this process of removing crystals from the water column precipitation. This formulation is taken from Holland & Feltham, and even though we are now dealing with open water, we keep the same formulation.

The reason for keeping the same formulation was that we were more interested in exploring the newer elements of our model, like the inclusion of water salinity and the ice growth once a layer of ice has formed, and so we could concentrate more on those processes, we kept the same formulation.

We can define a dimensionless distance from the surface, $z^+ = u_* \hat{z}/\nu$, where u_* is the friction velocity, $\hat{z}$ is the coordinate normal to the surface and ν is the molecular viscosity. The friction velocity is defined by $u_*^2 = C_d U^2$, where C_d is the quadratic drag coefficient.

The viscous boundary layer at the air-ocean interface is present but is narrower than next to a solid. Wu (1984) found z^+ to be between 4 and 8, depending on the wind velocity. The added effect of the wind stress on the ocean is already accounted for in the model, which uses a wind-speed depended turbulent diffusivity in the mixed layer. Further study could be carried out to investigate the impact of the variable turbulent conditions. We note this in the interpretation of model results.

We consider the different layers present. Just beneath the open air we have a viscous sublayer ($z^+ < 7$) where viscous stresses dominate. We then have a buffer layer ($7 < z^+ < 40$) where both viscous and turbulent stresses are important. Further out

$(40 < z^+ < 500)$ turbulent stresses dominate. We define these three layers respectively as the viscous sublayer, the buffer layer and the mixed layer (Figure 2.3).

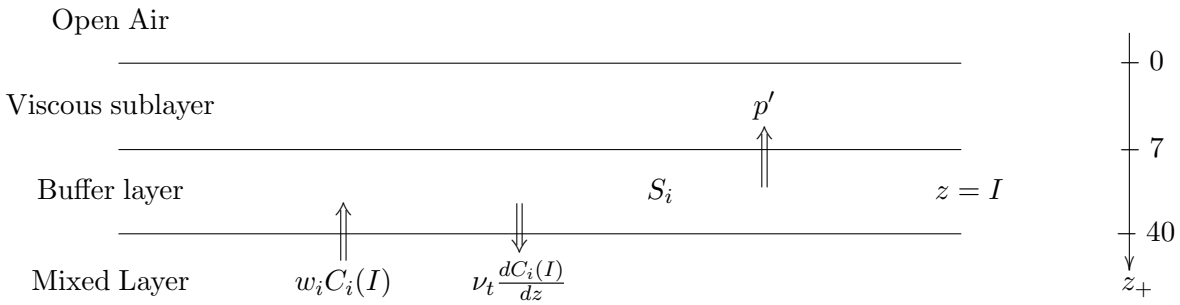

Figure 2.3: Schematic of balance of terms in the 'thin layer'

Using this schematic allows us to describe the different processes as sinks and sources in the different layers. We define buoyancy rising into the buffer layer from the mixed layer, turbulence out of the buffer layer into the mixed layer, interaction of frazil ice within the buffer layer, and precipitation out of the buffer layer into the viscous sublayer.

The crystal volume/mass balance in the buffer layer is applied as a surface boundary condition at $z = 0$ to the frazil equations in the mixed layer, and so the boundary condition at the surface becomes

$$\frac{\partial C_i(0)}{\partial t} = w_i C_i(0) - \nu_t \frac{\partial C_i(0)}{\partial z} + S_i + p'_i. \tag{2.2.34}$$

p'_i is the precipitation term which we now define. We distinguish between laminar and turbulent flows, since precipitation will be significantly different for both cases. Using the parameterization of McCave & Swift (1976), we define the turbulent precipitation as

$$p'_{iT} = -w_i C_i(0) \left(1 - \frac{U^2 + U_T^2}{U_{Ci}^2}\right) He \left(1 - \frac{U^2 + U_T^2}{U_{Ci}^2}\right) \tag{2.2.35}$$

where U is the depth-mean velocity in the mixed layer and U_T is the root-mean-square tidal velocity. He is the Heaviside function defined as equation (2.2.22), and U_{Ci} is the critical deposition velocity for each crystal size class, which can be calculated from the Sheilds criterion and the quadratic law,

$$U_{Ci}^2 = \frac{0.05(\rho_0 - \rho_i)g2r_i^e}{\rho_0 C_d}. \tag{2.2.36}$$

We define the laminar precipitation as being

$$p'_{iL} = \left(-w_i C_i(0) + \nu_t \frac{\partial C_i(0)}{\partial z} - S_i\right) He \left(-w_i C_i(0) + \nu_t \frac{\partial C_i(0)}{\partial z} - S_i\right) \tag{2.2.37}$$

The step function is used here to ensure that $p'_{iL} \geq 0$.

Now, to determine whether the flow is turbulent or laminar, we use the Richardson number, which can be defined as

$$Ri = \frac{-\frac{g}{\rho_m}\frac{\partial \rho_m}{\partial z}}{(\partial u/\partial z)^2}. \tag{2.2.38}$$

One issue is that the Richardson number is normally applied to a single component fluid where the viscosity is (almost) constant. Holland & Feltham adopted a new definition of Ri, which is modified to provide a single dimensionless quantity that represents the effects of frazil-seawater mixture viscosity, shear and stability on turbulence. It is assumed that shear stress exerted in the middle of the bursting layer by a steady externally driven flow is unchanged by an increase in the fluid viscosity and so

$$\nu_0 \left(\frac{\partial u}{\partial z}\right)_{ref} = \nu(C)\frac{\partial u}{\partial z}. \tag{2.2.39}$$

The Richardson number can then be simplified to

$$Ri = -\frac{g\nu(C)^2}{\rho_m \nu_0^2}\frac{\partial \rho_m}{\partial z}\left(\frac{\partial u}{\partial z}\right)_{ref}^{-2}, \tag{2.2.40}$$

where

$$\left(\frac{\partial u}{\partial z}\right)_{ref} = \frac{C_d U^2}{35\nu_0 \kappa} \tag{2.2.41}$$

is calculated using the predicted velocity profile in the vicinity of $z_+ = 35$ by the law

of the wall with depth-mean velocity U.

The calculation of the molecular viscosity as a function of the ice concentration $\nu(C)$ is poorly understood. The only estimate we have is that for concentration $C = 0.47$, the molecular viscosity is $\nu = 0.02$ m^{2}s^{-1}, so together with the pure-water value of ν_0 when $C = 0$, our best approximation is to use the linear function

$$\nu(C) = \nu_0 + \frac{0.02}{0.47}C. \tag{2.2.42}$$

Now we have Ri to calculate when the flow is laminar or turbulent, we can define the total precipitation, using a error function to smooth the function, as follows,

$$p_i = p'_{iT} + \frac{p'_{iL} - p'_{iT}}{2}\{1 + erf[d(Ri - Ri_C)]\} \tag{2.2.43}$$

where $Ri_C = 0.25$ and $d = 8$. This means, $p'_i \approx p'_{iT}$ if $Ri < 0$, and $p'_i \approx p'_{iL}$ if $Ri > 0.5$.

2.2.8 Frazil Rise Velocities

Several studies on frazil rise velocities have been carried out (e.g. Wueben 1984, Gosink & Osterkamp 1983, Daly 1984, Svensson & Omstedt 1994, Shen & Wang 1995), with the main objective to find a relation between rise velocity w_r and diameter d (Morse & Richard 2009).

Wueben (1984), using data from Gosink & Osterkamp's (1983) field work, proposed the following:

$$w_r = 0.3751 d^{0.64}. \tag{2.2.44}$$

But Wueben also made measurements and found them to be approximately 2.25 times lower than those found by Gosink & Osterkamp, so he proposed

$$w_r = 0.19 d^{2/3}. \tag{2.2.45}$$

Based on several sources of published experimental data related to the drag coefficients

of disks, Gosink and Osterkamp (1983) proposed a recursive set of equations to calculate the rise velocity, which depend on crystal drag (C_d) and the Reynolds number (Re),

$$log_{10}(C_d) = 1.386 - 0.892 log_{10}(Re) + 0.111[log_{10}(Re)]^2, \tag{2.2.46}$$

$$Re = \frac{w_r d}{\nu}, \tag{2.2.47}$$

and

$$w_r^2 = \frac{2(\rho_w - \rho_i) g a d}{\rho_w C_d}. \tag{2.2.48}$$

Daly (1984) assumed that the rise velocity changed with diameter range, and proposed the following:

$$w_r = \begin{cases} 0.02(g' \nu^{-1} d^2) & if\ d < 0.0006\ m \\ 0.0726(g'^{0.715} \nu^{-0.428} d^{1.14}) & if\ 0.0006\ m < d < 0.0028\ m \\ 0.5(g' r)^{1/2} & if\ d \geq 0.0028\ m \end{cases} \tag{2.2.49}$$

where g' and K_v are defined as

$$g' = 2\left(\frac{\rho_w - \rho_i}{\rho_w}\right)\left(\frac{g K_v}{\pi}\right) \tag{2.2.50}$$

and

$$\frac{K_v d^3}{8} = V_i \tag{2.2.51}$$

with V_i being the disk volume.

Svensson & Omstedt (1994) used a simplification of Daly's equations, and proposed that

$$w_r = 32.8 d^{1/2}. \tag{2.2.52}$$

Shen & Wang (1995) used the following:

$$w_r = -4\frac{k_2}{k_1}\frac{\nu}{d} + \sqrt{\left(4\frac{k_2}{k_1}\frac{\nu}{d}\right)^2 + \frac{4}{3k_1}\left(\frac{\rho_w - \rho_i}{\rho_w}\right)gd} \tag{2.2.53}$$

where $k_1 = 1.22$ and $k_2 = 4.27$.

HF, JB, SJ use the recursive algorithm of Gosink & Osterkamp (Eqs. (2.2.46)-(2.2.48)) to calculate the rising velocities and SO uses an approximation of Daly's (Eqs. (2.2.49)).

Morse & Richard (2009) studied a range of formulations and found a good approximation to be

$$w_r = \begin{cases} 2.025d^{1.621} & \text{, if } d \leq 1.27 \text{ mm} \\ -0.103d^2 + 4.069d - 2.024 & \text{, if } d > 1.27 \text{ mm} \end{cases} \tag{2.2.54}$$

where d is the diameter given in mm, and w_r is given in mm/s.

A study was carried out using all the above formulations to compare them and decide which one to use in this study. The final formulation in equation (2.2.54) was chosen as it gives the best fit to observations for the ranges discussed in this work.

This formulation has been corrected, after we had used it in our study (Morse & Richard 2010). The correct values should have been approximately twice as large, and so our results would be affected by the new formulation. Since the rise velocities would have been larger, the frazil crystals would have risen to the surface faster, which would have lead to a layer of ice forming faster at the surface.This would have lead to lower frazil ice formation rates.

2.2.9 Surface Heat Balance

The energy flux at the surface of the ocean can be defined as

$$E_{net} = \chi + F_{LW} - \epsilon\sigma T_0^4 + (1 - i_0)(1 - \alpha)F_{SW} + F_{sens} + F_{lat} \tag{2.2.55}$$

where each term represents a different type of heat flux.

χ is the oceanic diffusive flux, and is given by

$$\chi = -\nu_t \frac{\partial T}{\partial z}; \tag{2.2.56}$$

F_{LW} is the incoming longwave radiation which can be measured, and we will later take a value from observations; $-\epsilon\sigma T_0^4$ is the outgoing longwave radiation, given by the Stefan-Boltzmann law, which defines the power radiated from a black body in terms of its temperature. T is taken to be the temperature at the surface and ϵ is the emissivity, which is the ratio of the radiation emitted by a surface to the radiation emitted by a blackbody at the same temperature; $(1 - i_0)(1 - \alpha)F_{SW}$ is the net shortwave radiation. i_0 is the fraction of radiation that is not absorbed near the surface, and α is the albedo, which is the measure of the reflectivity of a surface; F_{sens} is the sensible heat emitted, which is given by Ebert & Curry (1993) as

$$F_{sens} = \rho_a c_a C_T v_a (T_a - T_0) \tag{2.2.57}$$

where T_a is the air temperature at a reference height (taken here to be 5 m), T_0 is the temperature of the water at the surface and v_a is the wind speed at the reference height; F_{lat} is the latent heat, and is also taken from Ebert & Curry (1993) as

$$F_{lat} = \rho_a \mathcal{L}^* C_t v_a (q_a - q_0) \tag{2.2.58}$$

where q_a is the humidity at a reference height (e.g. 5 m) and q_0 is the humidity at the surface. The value for q_a is taken from measurements, but q_0 is calculated using

$$q_0 = \frac{0.622 p_v}{p_{atm} - 0.378 p_v} \tag{2.2.59}$$

where the vapour pressure is

$$p_v = 2.53 \times 10^8 e^{(-5420/T_0)}. \tag{2.2.60}$$

If there is no phase change at the surface then $E_{net} = 0$ and so

$$\nu_t \frac{\partial T}{\partial z} = F_{LW} - \epsilon\sigma T^4 + (1 - i_0)(1 - \alpha)F_{SW} + F_{sens} + F_{lat}. \tag{2.2.61}$$

2.3 Grease Ice Growth

When enough frazil ice forms and rises to the surface, it builds up at the sea ice edge due to the effects of wind and water currents and becomes grease ice, a mixture of frazil and sea water which resembles an "oil slick", hence the name. The stronger the force driving the frazil ice to the edge, the more piled-up the ice becomes. We define the collection depth of a lead or polynya as the maximum depth the grease ice would accumulate at the edge.

Figure 2.4: Grease ice layer build up near pack ice with collection depth h_g. (Smedsrud (2011))

Figure 2.4 shows the process of grease ice build up near pack ice in a lead. L_{lead} is the length of the lead, L is the length of the grease ice layer, h_g is the collection depth of the grease layer, U_a is the wind speed, U_w is the ocean current and F_{tot} is the total heat flux at the surface. By balancing the packing force of the ice and the stress from the wind above and the water below, Smedsrud (2011) derived the collection depth to be

$$h_g(x) = \sqrt{\frac{\rho_a C_a}{K_r}} U_a \sqrt{x}, \tag{2.3.1}$$

where ρ_a is air density, C_a is the open-ocean drag coefficient, and $K_r \approx 100$ N m^{-3} is the resistance force constant. We can also deduce the total grease-ice volume as

$$V_g = \int_0^L h_g dx = \frac{2}{3}\sqrt{\frac{\rho_a C_a}{K_r}} U_a L^{\frac{3}{2}}, \tag{2.3.2}$$

which can be rearranged to give

$$L = \left[\frac{3}{2}\frac{V_g}{U_a}\sqrt{\frac{K_r}{\rho_a C_a}}\right]^{\frac{2}{3}} \tag{2.3.3}$$

We define a_{cover} as the area of domain which is not covered in grease ice, and calculate this as

$$a_{cover} = 1 - \frac{L}{L_{lead}}. \tag{2.3.4}$$

We define the point at which the lead closes as

$$a_{cover} = 0.95. \tag{2.3.5}$$

We set the threshold at 95% for mathematical convenience, since it would never reach 100% because the closer the cover gets to 100% the slower the ice growth is because of the insulation effect of the ice cover.

2.4 Mushy Layer Equations

Once we have a full cover of ice at the surface of the mixed layer, using the mushy layer equations of Feltham et al (2006) , we can calculate the rate at which the ice grows from beneath. To do this, we consider the domains of the ice and the water separately, and calculate the heat fluxes occurring at the ice-ocean interface.

At the surface of the ice, the boundary condition remains the same as that of water (eq (2.2.61)), except that we are now dealing with ice so the diffusivity changes accordingly. In the ice domain, we use mushy layer theory, with the governing equation being

$$c_{\text{eff}} \frac{\partial T}{\partial t} = \frac{\partial}{\partial z}(k_{\text{eff}} \frac{\partial T}{\partial z}), \tag{2.4.1}$$

where c_{eff} and k_{eff} are the effective volumetric specific heat capacity and thermal conductivity of sea ice. These are calculated from

$$c_{\text{eff}} = c_i - \frac{T_L(S_{bulk}) - T_L(0)}{\theta^2} L, \tag{2.4.2}$$

and

$$k_{\text{eff}} = k_{\text{bi}} - (k_{\text{bi}} - k_{\text{b}}) \frac{T_L(S_{\text{bulk}}) - T_L(0)}{\theta}, \tag{2.4.3}$$

where $T_L(S_{\text{bulk}})$ is the freezing liquidus temperature for the bulk salinity S_{bulk}, $T_L(0)$ is the freezing temperature of pure water, $\theta = T - T_L(0)$, L is the volumetric heat of fusion of pure ice, c_i is the volumetric heat capacity of pure ice, and k_{bi} and k_{b} are the conductivities of bubbly ice and brine, and are given by

$$k_{\text{bi}} = \frac{2k_i + k_a - 2V_a(k_i - k_a)}{2k_i + k_a + V_a(k_i - k_a)} k_i, \tag{2.4.4}$$

and

$$k_b = 0.4184(1.25 + 0.030K^{-1}\theta + 0.00014K^{-2}\theta^2), \tag{2.4.5}$$

(Schwerdtfeger, 1963) where $k_i = 1.16(1.91 - 8.66 \times 10^{-3}K^{-1}\theta + 2.97 \times 10^{-5}K^{-2}\theta^2)$ is the conductivity of pure ice, $k_a = 0.03$ W(m K^{-1}) is the conductivity of air, and $V_a = 0.025$ is the fractional volume of air in sea ice.

At the ice-ocean interface, the ice and water are at the freezing temperature of the ocean water.

Using the solutions from both the governing equations of the ice temperature and the water temperature, we can calculate the heat balance at the ice-ocean interface, and from this we can calculate the ice growth using a modified version of a Stefan condition, to include salinity. These are given by Notz & Worster (2008) and are defined as

$$\rho_i \mathcal{L} \phi \frac{dh}{dt} = k_i \frac{\partial T_i}{\partial z} - F_{ocean}(T_w), \tag{2.4.6}$$

where the first term on the RHS is the heat flux from the ice to the water, and $F_{ocean}(T_w)$ is the heat flux from the water into the ice, which is defined as

$$F_{ocean}(T_w) = \nu_t \frac{\partial T_w}{\partial z}, \tag{2.4.7}$$

$$\phi S \frac{dh}{dt} = D \frac{\partial S}{\partial z} + F_{brine}, \tag{2.4.8}$$

where F_{brine} is the salt flux at the ice-ocean interface, and

$$T_w = T_0 - \Gamma S_w, \tag{2.4.9}$$

which is the equation of the liquidus curve. h is the depth of the ice, k_i is the conductivity of ice, and ϕ is the ice solid fraction defined by

$$\phi = 1 - \frac{S_{\text{bulk}}}{S_w}. \tag{2.4.10}$$

Equations (2.4.6)–(2.4.9) are solved at each time step to give $\frac{dh}{dt}$, and the temperature and salinity at the interface.

2.5 Desalination of the Sea Ice

When sea ice is forming, salt is rejected from the ice crystals into the surrounding ambient water forming brine. This raises the salinity in the near-surface of the crystals. Sometimes this brine gets trapped in between crystals, and since it has high salinity, it can remain liquid even if the temperature decreases further. These are called brine pockets.

When the sea ice thickness reaches a critical value, the brine in the pockets is transported downwards by gravity (Wettlaufer et al. 1997). This happens through the formation of brine channels which are channels in the sea ice and carry the high salinity brine into

the lower salinity ocean. Together with the salt which is instantaneously rejected during sea ice formation, these are two ways in which forming sea ice rejects salt.

Wells et al (2011) noticed that brine channels form to maximize the rate of removal of stored potential energy. Using this they created a model of sea ice growth and found that the brine flux could be parameterized as

$$F_{brine} = \begin{cases} \gamma \dfrac{\rho_0 g \beta (C_E - C_0)^2 \Pi_0}{\mu} \left(\dfrac{R_m - R_c}{R_m} \right) & , R_m > R_c \\ 0 & , R_m < R_c, \end{cases} \tag{2.5.1}$$

where we define the porous medium Rayleigh number R_m as

$$R_m = \frac{\rho_0 g \beta \Delta C \Pi_0 l_T}{\mu \kappa} \tag{2.5.2}$$

where β is the haline expansion coefficient, $\Delta C = C_E - C_0$ where C_E is the eutectic temperature and C_0 is the ambient water salinity, l_T is length of sea ice, in our case the depth h, μ is the dynamic viscosity, κ is the thermal diffusivity and Π_0 is the permeability given by

$$\Pi_0 = 3 \times 10^{-8} (1 - \phi)^3 \tag{2.5.3}$$

where ϕ is the solid fraction of the sea ice defined in equation (2.4.10) (Golden et al 2007).

a_r	Crystal aspect ratio	0.02	-
β_S	Salinity expansion coefficient	7.86×10^{-4}	psu^{-1}
β_T	Temperaature expansion coefficient	3.87×10^{-5}	$^{\circ}\text{C}^{-1}$
c_a	Specific heat capacity of dry air	1005	$\text{J kg}^{-1}{}^{\circ}\text{C}^{-1}$
c_0	Specific heat capacity	3974	$\text{J kg}^{-1}{}^{\circ}\text{C}^{-1}$
C_d	Quadratic drag	1.5×10^{-3}	-
C_t	Stability dependent bulk transfer coefficient	1.235×10^{-3}	-
d	Arbitrary Number	8	-
ϵ	Turbulent dissipation rate	7.4×10^{-6}	W kg^{-1}
ϵ_0	Longwave emissivity	0.99	-
F_{LW}	Longwave radiation	168.3	W m^{-2}
g	Gravity	9.81	m s^{-2}
I	Layer depth	60	m
κ	Von Karmann constant	0.41	-
K_T	Molecular thermal diffusivity	1.4×10^{-7}	$\text{m}^2\ \text{s}^{-1}$
$\mathcal{L}$	Latent heat of ice fusion	3.35×10^5	J kg^{-1}
$\mathcal{L}^*$	Latent heat of vaporization	2.501×10^{-6}	J kg^{-1}
N_{ice}	Number of size classes	10	-
Nu	Nusselt number	1	-
p_{atm}	Atmospheric Pressure	101.325	kPa
ρ_a	Density of dry air	1.275	kg m^{-3}
ρ_0	Density of water	1028	kg m^{-3}
ρ_I	Density of ice	917	kg m^{-3}
q_a	Air humidity	4×10^{-5}	-
Ri_C	Critical Richardson Number	0.25	-
σ	Stefan-Boltzmann constant	5.67×10^{-8}	$\text{W m}^{-2}\text{K}^{-4}$
S	Ocean salinity	34.5	psu
S_0	Reference Salinity	34.5	psu
T_0	Reference Temperature	-2.0	$^{\circ}$C
T_a	Air temperature	248.7	K
U	Plume speed parallel to surface	0.055	m s^{-1}
U_T	Root-mean-squared tidal velocity	0.06	m s^{-1}
v_0	Molecular viscosity of water	1.95×10^{-6}	m^2s^{-1}
ν	Wind speed	5	m s^{-1}
ν_t	Turbulent eddy coefficient	1×10^{-2}	m^2s^{-1}

Table 2: List of model parameters and constants

3 Well Mixed Case

As a test of the frazil component of our model of new sea ice growth introduced in Chapter 2, we first look at a well-mixed case, where we assume that the domain is perfectly mixed, and hence we ignore the terms of advection and diffusion. This follows directly on from a study that was carried out in Holland & Feltham. Equations (2.2.12) and (2.2.16) simply become

$$\frac{\partial C_i}{\partial t} = S_i \tag{3.0.4}$$

and

$$\frac{\partial T}{\partial t} = w'(T_f - T - \mathcal{L}/c_0). \tag{3.0.5}$$

We consider a case when $N_{ice} = 10$ size classes are used, and the radii of the size classes are $r = \{0.01, 0.05, 0.15, 0.3, 0.4, 0.5, 0.6, 0.8, 1, 2\}$ mm, which includes the majority of frazil crystals sizes in experiments and observations.

Since for now we are only investigating how the crystals grow, we use a uniform supercooling of 1×10^{-4} ℃, and so the initial condition is

$$T_{in} = T_f - 1 \times 10^{-4}. \tag{3.0.6}$$

For the initial concentrations, we start with an amount of 4×10^{-8} divided equally between the 10 size classes to facilitate comparison between size classes during the run. The initial condition for the ice concentration is then

$$C_{i_{in}} = 4 \times 10^{-9}. \tag{3.0.7}$$

So equations (3.0.4), (3.0.5), (3.0.6), and (3.0.7) form a closed system of ordinary differential equations, which were solved numerically.

3.1 Results

To validate the solution, we check that the amount of heat being released from ice formation is the same as the heat equivalent to the increase in water temperature. Integrating the temperature equation over the period until $t = t_a$, we get

$$\int_{t_0}^{t_a} \frac{\partial T}{\partial t} dt = \int_{t_0}^{t_a} w'(T_f - T - \mathcal{L}/c_0) dt \tag{3.1.1}$$

which expands to

$$\rho_0 c_0 (T(t_a) - T(t_0)) = \rho_i \mathcal{L} \sum_{1}^{N_{ice}} (C_i(t_a) - C_i(t_0)) + \rho_i c_0 \int_{t_0}^{t_a} \sum_{1}^{N_{ice}} C_i (T_f - T). \tag{3.1.2}$$

The term on the left hand side is the amount of heat needed to raise the temperature of the water from $T(t_0)$ to $T(t_a)$, the first term on the right hand side is the amount of latent heat released form the formation of ice crystals, and the second term on the right hand side is the amount of sensible heat needed to lower the temperature of the water to freezing temperature before the crystals form. After calculating all three terms numerically, and checking that they agree with the above equation, we can assume that our solution is correct.

Fig. 3.1 shows the water temperature over the first 2 days of model time. The temperature increases as expected as the ice crystals are being formed to quench the supercooling and after 2 days we enter a quasi-steady state, when ice stops being created. This is simply a quasi-steady state since secondary nucleation still occurs for a lot longer.

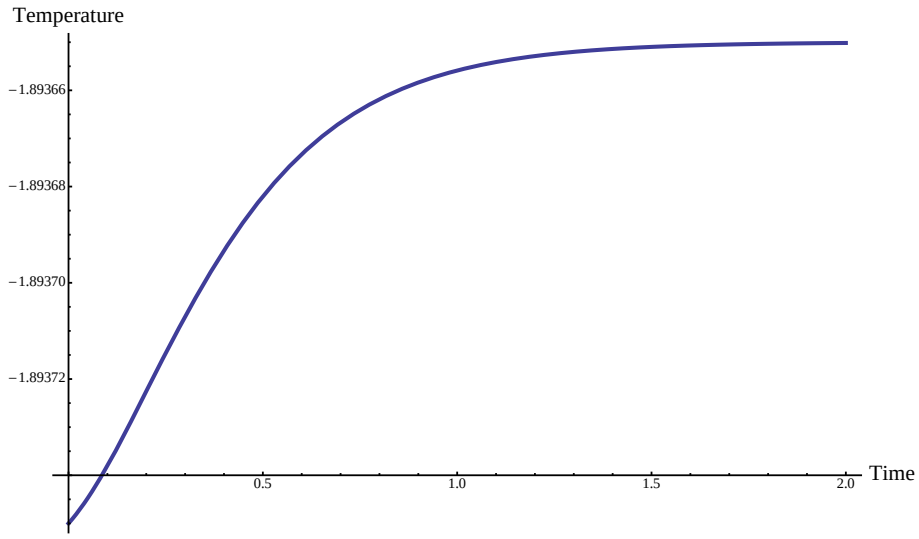

Figure 3.1: Temperature of water in first 2 days.

We look next at the concentration of the different size classes over the same period in Fig. 3.2 and find that, as we expect, the concentrations increase for the first 2 days until it halts. Since secondary nucleation occurs for a lot longer and acts as a source for size class 1, and a sink for the rest, the long term steady state is for all ice to end up in size class 1.

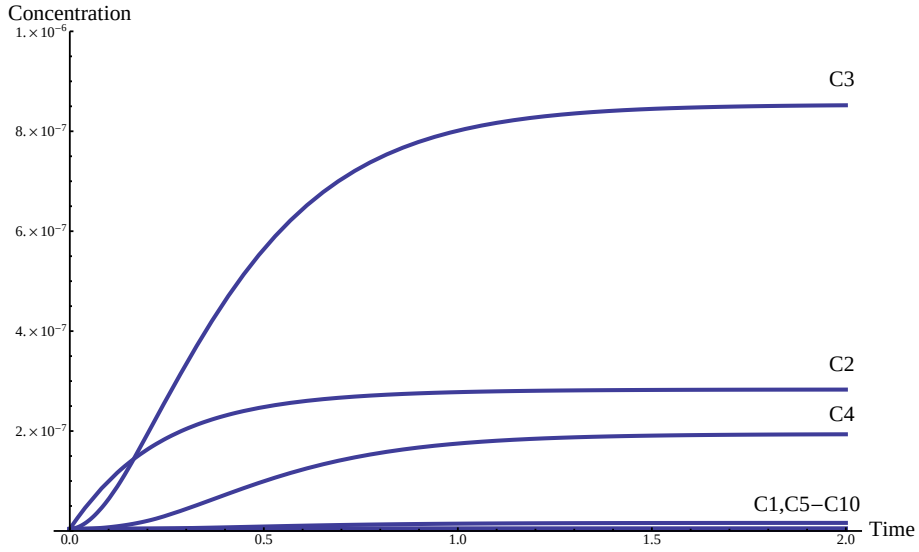

Figure 3.2: Concentration of different size classes in first 2 days.

An interesting point to note is the concentrations of the different ice concentration size classes. Smaller size classes are a lot closer in size so it is easier for them to grow to the

next size class, and larger size class crystals are more likely to suffer secondary nucleation since the volume swept is a lot larger. Consequently, the predominant size classes are in fact the intermediate ones (C_2,C_3 and C_4).

We now describe the first of two case studies analysed in this thesis, Tsang & Hanley (1985). Even though the model used in the calculations in the following case study is more advanced than the well-mixed case just described, the experiments are carried out in a well-mixed box and so the results are more relevant to this section.

3.2 Tsang & Hanley (1985)

Tsang & Hanley (1985) studied the initial stages of the formation of frazil ice in various different sets of laboratory experiments. As the experiments were conducted in a controlled environment, measurements of the salinity, temperature and ice concentration were possible. We can use the results from this work to test our model and, as we will show, also to constrain the parameter a_{nuc} from the secondary nucleation definition.

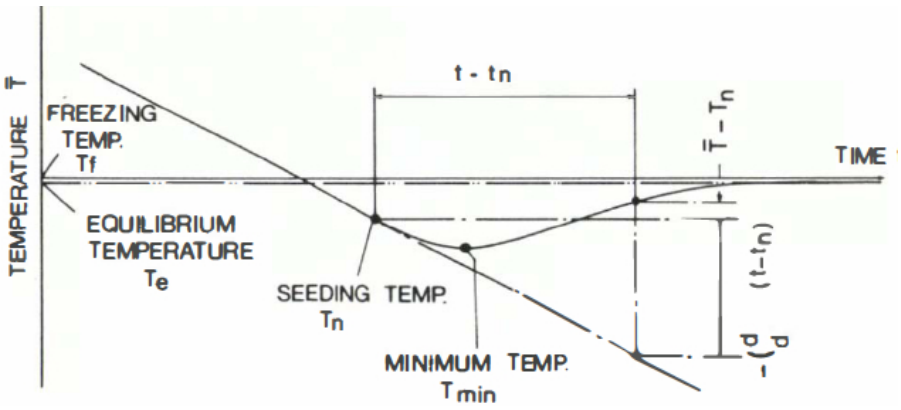

Figure 3.3: Typical time series of temperature in the initial stages of frazil ice formation.

Figure 3.3 shows the typical temperature time-series in the first instances of frazil ice formation. The water temperature is initially decreasing due to the heat flux at the surface of the water. At a time t_n, the water is seeded with an ice crystal, and from then ice starts forming through ice growth and secondary nucleation. There is a delay before the temperature begins to rise again until it reaches the equilibrium temperature. The equilibrium

temperature is still slightly below the freezing temperature, since ice is still being formed.

Two of the parameters measured in each of the experiments are the minimum temperature T_{min} and the time at which that minimum occurs t_{min}.

Two of the parameters in our model that influence T_{min} and t_{min} are the amount of ice present at seeding, and the efficiency of the secondary nucleation. This was previously defined in Chapter 2 as being

$$N_i = -\frac{a_{nuc} C_i W_i \sum_i C_i}{r_i^e} \tag{3.2.1}$$

where a_{nuc} is a parameter which limits the amount of secondary nucleation occurring. We can use the results from these experiments to give it a more accurate value.

Since we have simplified the initial seeding in our model by starting the model run with ice present, we can only start from time t_n. The initial amount of ice present is unclear from the paper, so we used a range of values and compared each to the results expected.

Two different experiments from the paper were used, one from the set of experiments A, and one from the set of experiments C.

The results from a modified version of our model were then compared to the observations. Since we have the measurements of the tank in which the experiments took place, we can define our model domain to be the same depth. We can also calculate the heat loss at the surface from the cooling rate of the water by calculating the total heat loss in the water.

If $\frac{dT}{dn}$ is the cooling rate of the water, the total heat loss at the surface per unit area is

$$F_{heat} = \rho_0 c_0 d \frac{dT}{dn} \tag{3.2.2}$$

where ρ_0 is the density of water, c_0 is the specific heat capacity and d is the depth of

the tank. The units of F_{heat} are therefore Wm^{-2}.

Since we want to compare two variables (T_{min} and t_{min}), we define a cost function as follows

$$\Psi = \sqrt{(\alpha_T(T_{min} - T^e_{min}))^2 + (\alpha_t(t_{min} - t^e_{min}))^2} \tag{3.2.3}$$

which we then try to minimize for T_{min} and t_{min}, where the e superscript denotes the experimental values. So that we can compare temperature and time, we use the price parameters α_T and α_t which we must define so that the both parts of the cost function are in the same unit. Since we are dealing with temperature and time, we can convert both into heat, by multiplying the temperature by the sensible heat of the water and time by heat loss at the surface. We then define α_T and α_t as

$$\alpha_T = \rho_0 c_p d \quad [JK^{-1}m^{-2}] \tag{3.2.4}$$

and

$$\alpha_t = F_{heat} \quad [Wm^{-2}], \tag{3.2.5}$$

where ρ is the water density, c_p is the specific heat capacity, d is the depth of the tank and F_{heat} is the heat flux at the surface.

In the group A experiments, artificial water was used, by mixing "Forty Fathoms" salt dissolved in distilled water, and they were conducted in a plexiglass tank of measurements 38 cm long × 25.5 cm wide × 15 cm deep. The air temperature was about 15°C below freezing. Eight experiments were carried out, named A1-A8. We solely looked at experiment A1. The parameters of that experiment are given in Table 3

We then ran our model for varying parameters initial concentration C_{in} and secondary nucleation parameter a_{nuc}, and the results of the cost function are shown in table 6. From these results, we can assume that an adequate value for a_{nuc} is 1 with an initial amount

Parameter	Value
Salinity	47.1 psu
Seeding temperature (T_n)	-2.681℃
Minimum temperature (T_{min})	-2.695 ℃
Equilibrium temperature (T_e)	-2.651 ℃
Supercooling at seeding ($T_e - T_n$)	0.030 ℃
Cooling rate at seeding ($(dT/dt)_n$)	-5.14×10^{-4} ℃/s
Heat loss at surface (from cooling rate) (F_{heat})	315.59 Wm^{-2}
Time of minimum temperature (t_{min})	72 s
Average rate of ice production (dc/dt)	7.554×10^{-6} s^{-1}

Table 3: Parameters of experiment A1.

of ice present of 1×10^4. Since we do not know how much ice was present initially, we can not make too many assumptions based on these results, but nevertheless we can take an estimate of a_{nuc}.

C_{in}/a_{nuc}	1×10^{-3}	1×10^{-2}	1×10^{-1}	1×10^{0}
10^{-8}	∞	4.81×10^7	5.49×10^6	1.30×10^6
10^{-7}	4.81×10^7	5.45×10^6	1.28×10^6	5.45×10^5
10^{-6}	5.34×10^6	1.22×10^6	5.15×10^5	2.34×10^5
10^{-5}	1.08×10^6	4.46×10^5	1.98×10^5	7.56×10^4
10^{-4}	3.10×10^5	1.32×10^5	4.15×10^4	8.30×10^3
10^{-3}	1.23×10^5	1.38×10^5	3.48×10^4	3.48×10^4

Table 4: Cost Function Ψ - Experiment A1.

We also ran a similar study for one of the experiments in group C, namely C1. These experiments used real Atlantic sea-water, and so are more comparable to the amount of salinity in our model. The parameters of that experiment are given in Table 5. The data from this experiment is as follows:

We used the same cost function as defined earlier and the same initial conditions C_{in} and secondary nucleation parameters a_{nuc}, and table 6 shows the results.

Similarly to the previous results, the minimum Ψ occurs when C_{in} is 1×10^{-4}, but when a_{nuc} is 1×10^{-1}.

We conclude that the model adequately reproduces the experimental results with a

Parameter	Value
Salinity	31.6 psu
Seeding temperature (T_n)	-1.728°C
Minimum temperature (T_{min})	-1.764 °C
Equilibrium temperature (T_e)	-1.728 °C
Supercooling at seeding ($T_e - T_n$)	0.000 °C
Cooling rate at seeding ($(dT/dt)_n$)	-2.68×10^{-4} °C/s
Time of minimum temperature (t_{min})	298 s
Average rate of ice production (dc/dt)	4.673×10^{-6} s^{-1}

Table 5: Parameters of experiment C1.

C_{in}/a_{nuc}	1×10^{-3}	1×10^{-2}	1×10^{-1}	1×10^{0}
10^{-8}	∞	3.24×10^{7}	4.00×10^{6}	1.11×10^{6}
10^{-7}	1.02×10^{7}	3.96×10^{6}	1.09×10^{6}	4.57×10^{5}
10^{-6}	3.86×10^{6}	1.03×10^{6}	4.30×10^{5}	1.72×10^{5}
10^{-5}	9.15×10^{5}	3.70×10^{5}	1.40×10^{5}	4.15×10^{4}
10^{-4}	2.69×10^{5}	8.57×10^{4}	2.78×10^{4}	6.49×10^{4}
10^{-3}	1.85×10^{5}	9.35×10^{4}	9.35×10^{4}	9.35×10^{4}

Table 6: Cost Function Ψ - Experiment C1.

range of values of C_{in} (10^{-3} to 1) and a_{nuc} (10^{-8} to 10^{-3}), and since the values of Ψ are still relatively small for $a_{nuc} = 1 \times 10^{0}$, we assume that it is a good estimate of that parameter, and will continue to use that value throughout this study.

4 Vertical Diffusion Case

In this chapter, we will consider the frazil ice model of Chapter 2 with vertical and horizontal terms included. We start with the model description, then a reference run with parameters taken from observations.

4.1 Model Set Up

We start with the equations describing the local balance of crystal concentration, heat and salt, (2.2.12), (2.2.16) and (2.2.19), and write these out, expanding into horizontal and vertical derivatives

$$\frac{\partial C_i}{\partial t} + u\frac{\partial C_i}{\partial x} + w\frac{\partial C_i}{\partial z} + w_i\frac{\partial C_i}{\partial z} = \frac{\partial}{\partial x}\left(\nu_T\frac{\partial C_i}{\partial x}\right) + \frac{\partial}{\partial z}\left(\nu_T\frac{\partial C_i}{\partial z}\right) + S_i, \tag{4.1.1}$$

$$\frac{\partial T}{\partial t} + u\frac{\partial T}{\partial x} + w\frac{\partial T}{\partial z} = \frac{\partial}{\partial x}\left(\nu_T\frac{\partial T}{\partial x}\right) + \frac{\partial}{\partial z}\left(\nu_T\frac{\partial T}{\partial z}\right) + w'\left(T_f - T - \frac{L}{c_0}\right), \tag{4.1.2}$$

and

$$\frac{\partial S}{\partial t} + u\frac{\partial S}{\partial x} + w\frac{\partial S}{\partial z} = \frac{\partial}{\partial x}\left(\nu_T\frac{\partial S}{\partial x}\right) + \frac{\partial}{\partial z}\left(\nu_T\frac{\partial S}{\partial z}\right) + w'S. \tag{4.1.3}$$

We can now make assumptions about the relative size of these terms:

1. Since the rising velocities and vertical diffusion of the crystals are much larger than vertical advection, we can ignore the 3rd term on the RHS of the concentration equation.

2. Since the vertical diffusion of heat and salt is a lot larger than the vertical advection, we can also ignore the 3rd term on the RHS of both the temperature and salinity equations.

3. Since vertical processes dominate in leads and polynyas, we can also assume that horizontal processes have a negligible effect compared to vertical processes, and so we ignore all horizontal terms.

With these assumptions, the three equations (4.1.1)-(4.1.3) then become:

$$\frac{\partial C_i}{\partial t} = \nu_T \frac{\partial^2 C_i}{\partial z^2} - w_i \frac{\partial C_i}{\partial z} + S_i, \tag{4.1.4}$$

$$\frac{\partial T}{\partial t} = \nu_T \frac{\partial^2 T}{\partial z^2} + w' \left(T_f - T - \frac{L}{c_0} \right), \tag{4.1.5}$$

and

$$\frac{\partial S}{\partial t} = \nu_T \frac{\partial^2 S}{\partial z^2} + w' S, \tag{4.1.6}$$

which become the balance equations of our model.

We must now define the model domain, the turbulent diffusivity and the initial and boundary conditions.

With regards to domain, we wish to include the mixed layer and also ambient water beneath. We assume that the mixed layer is 10 m deep and the ambient water is 90 m beneath, giving us 100 m of domain depth. We define the initial conditions and the turbulent diffusivity with a mixed layer of 10 m, but we also allow the mixed layer to grow should that be the case.

The turbulent diffusivity in the mixed layer is affected by three processes: waves at the surface, wind-driven ocean currents and differences in water density causing convection. We assume the effects of the first two processes are even throughout the mixed layer, hence if the density profile is stable, the turbulent diffusivity is constant. To simplify the model, we assume the stable turbulent diffusivity is constant and define it as

$$\nu_{T1} = \begin{cases} 1 \times 10^{-2} \text{ m}^2/\text{s} & , x < 10 \text{ m} \\ 1 \times 10^{-4} \text{ m}^2/\text{s} & , x \geq 10 \text{ m} \end{cases} \tag{4.1.7}$$

where x is the depth from the surface. The mixed layer is by definition more mixed than the ambient water, and we take the high value of mixing of 1×10^{-2} m^2/s and the

low value of mixing of 1×10^{-4} m^2/s. We have assumed a fixed stable turbulent diffusivity here, which is independent of wind and current velocities. This assumption means we will need to take care later on in the wind speed sensitivity study and take this into account.

We also need to consider the case when the density profile in the water becomes unstable. This happens when heavier water is above lighter water, and it creates very strong mixing to stabilise the density profile. We can then define the total turbulent diffusivity, using the above definition as

$$\nu_T = \begin{cases} 1 & , \frac{\partial \rho}{\partial z} < 0 \\ \nu_{T1} & , \frac{\partial \rho}{\partial z} \geq 0 \end{cases}. \tag{4.1.8}$$

We would expect the density profile to become unstable in the upper layers of the ocean as soon as it is in contact with the cold atmosphere since the water temperature decreases there and this increases the density. If the unstable density domain reaches the bottom of the mixed layer we would expect the mixed layer to grow from the 10 m, which we have predefined.

To initiate our model, we assume that a small amount of frazil ice is present at $t = 0$, similarly to the well-mixed scenario. We also take the same initial amount of ice, but only present in the mixed layer and so we can define the ice concentration initial condition as

$$C_i(0, z) = \begin{cases} 4 \times 10^{-9} & , z < 10 \text{ m} \\ 0 & , z \geq 10 \text{ m} \end{cases}. \tag{4.1.9}$$

The initial profiles of temperature and salinity were chosen to best replicate a realistic upper layer of ocean with a 10 m mixed layer. We expect the temperature to be lower in the mixed layer and close to the freezing temperature and higher in the ambient water, and we expect the salinity to be lower in the mixed layer and higher in the ambient water, due to the previous sea ice melt and summer river runoff. We also define the profiles so that we start with a stable density profile and let it become unstable during the model

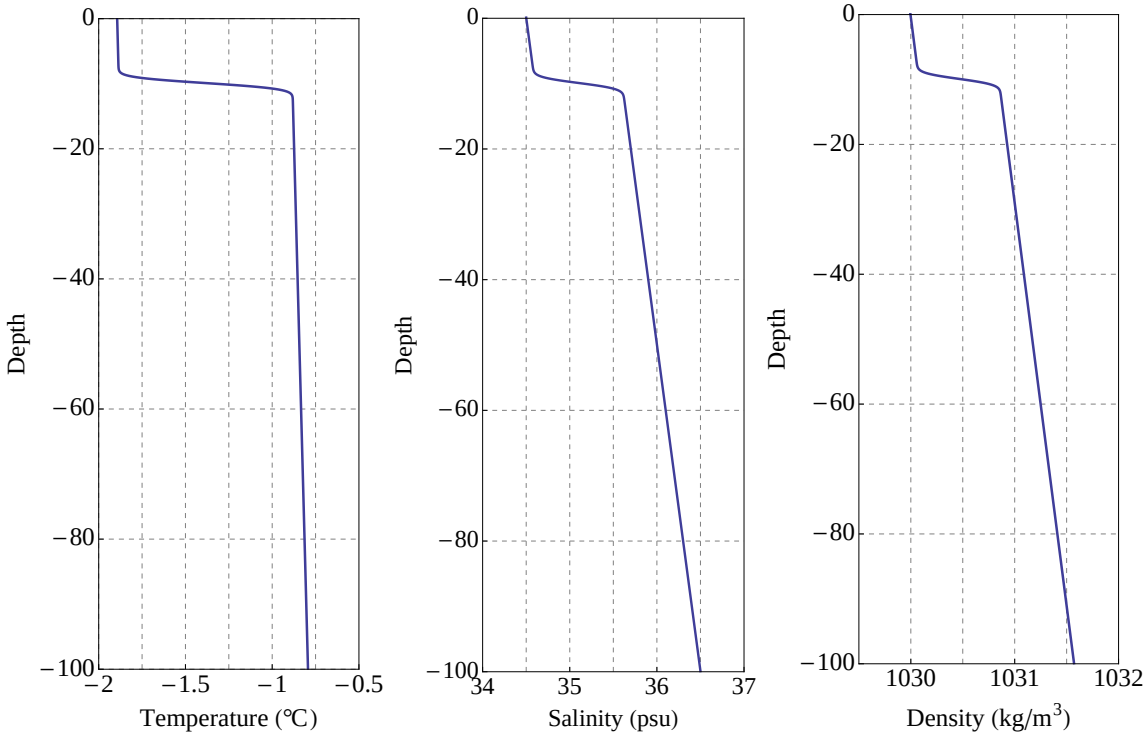

Figure 4.1: Initial profiles of temperature, salinity and density.

run. Figure 4.1 shows the initial temperature, salinity and equivalent density profiles we adopted in our model runs. The pyncocline can clearly be seen at 10 m, which separates the mixed layer from the ambient water below.

The boundary conditions for our domain have previously been defined in Chapter 2. Equation (2.2.34) is our upper ice concentration boundary condition, and equation (2.2.61) is our upper temperature boundary condition. We have prescribed the upper and lower salinity boundary conditions as being of zero flux, and the lower boundary conditions of ice concentration and temperature are also of zero flux. The boundary conditions are then

$$\frac{\partial C_i}{\partial t} = w_i C_i - \nu_t \frac{\partial C_i}{\partial z} + S_i + p_i', \qquad \nu_T \frac{\partial S}{\partial z} = 0 \qquad (z = 0), \tag{4.1.10}$$

$$\nu_T \frac{\partial T}{\partial z} = F_{LW} - \epsilon\sigma T^4 + (1 - i_0)(1 - \alpha)F_{SW} - F_{sens} - F_{lat} \qquad (z = 0), \tag{4.1.11}$$

$$\nu_T \frac{\partial S}{\partial z} = 0, \qquad \nu_T \frac{\partial C_i}{\partial z} = 0, \qquad \nu_T \frac{\partial T}{\partial z} = 0 \qquad\qquad (z = I), \tag{4.1.12}$$

where $I = 100$ m is the bottom of our domain.

To solve the model a FORTRAN computer program was written in which the whole system of equations ((4.1.4)-(4.1.6)), boundary conditions ((4.1.10) - (4.1.12)) and initial conditions as defined in figure 4.1 were numerically solved with the help of NAG routines D03 PCA and D03 PZF. The space resolution of the model was 10 cm, so over 100 m of domain we had 1000 depth points. The time resolution was 1 s, so over 2 days of run we had 172,800 time points. (See appendix for code)

We calculate the volume of frazil ice which is precipitated out of the domain into the viscous sublayer, where we assume it stays and cannot re-enter the domain. This ice eventually leads to grease ice, and finally a layer of congelation ice. We use the parameterization of Smedsurd et al (2011) to calculate how the grease ice grows in a lead, and how it affects the ice cover and hence the heat loss at the surface.

Smedsrud et al assume that grease ice is 25% solid ice and 75% water, and calculate the amount of solid ice formed directly from the heat loss at the surface and the latent heat. Since our model directly outputs the volume of precipitated ice, we use this value to calculate the grease ice volume using

$$V_g = \frac{V_p}{0.25} L_{lead} \tag{4.1.13}$$

where V_p is the volume of precipitated frazil ice, and L_{lead} is the length of the lead. The grease ice is assumed to be pushed against a large floe of stagnant pack ice by the wind, and we can calculate the total length of the grease ice layer L from equation 2.3.3

The upper temperature boundary condition (4.1.11) now becomes

$$\nu_T \frac{\partial T}{\partial z} = (1 - a_{cover})(F_{LW} - \epsilon\sigma T^4 + (1 - i_0)(1 - \alpha)F_{SW} - F_{sens} - F_{lat}), \tag{4.1.14}$$

which assumes negligible heat loss from the ocean through the grease ice. When $L = L_{lead}$, the heat flux stops and we start the next stage of our model. This happens when

$$V_p = \frac{3}{8} U_a \sqrt{\frac{L_{lead}\rho_a C_a}{K_r}}. \tag{4.1.15}$$

Although it is assumed that grease ice forms with 25% ice, since heat is still being lost from the grease ice layer, we assume that the ice fraction increases as ice is formed, and that the total volume of grease ice is kept constant. Using the temperature boundary condition we can calculate the total heat flux at the surface per unit area as

$$F_{heat} = F_{LW} - \epsilon\sigma T(0)^4 + (1 - i_0)(1 - \alpha)F_{SW} - F_{sens} - F_{lat} \tag{4.1.16}$$

and use this to calculate the rate of increase of grease ice solid fraction ϕ_g,

$$\frac{d\phi_g}{dt} = \frac{F_{heat}}{\rho_0 L}, \tag{4.1.17}$$

where ρ_0 is the density of sea water, and L is the latent heat of water.

So, once the grease ice cover is 95% ($a_{cover} = 0.95$) we stop heat loss from the water below but the grease ice solid fraction continues to increase until we reach a cut-off point of 70% ($\phi_g = 0.7$). The time it takes to reach this point can be calculated from the ice volume precipitation rate and the total volume of grease ice. At this point, we precipitate any frazil ice that was still below the grease ice layer in the ocean on to the ice and stop frazil ice production in the water. This follows from the fact that when an ice layer forms at the surface, the turbulent mixing beneath decreases and whatever ice that is still present in the water will quickly rise. The amount of ice left in the water was found to be small compared to the amount of ice which had precipitated up until this point. We now solely concentrate on the downwards growth of congelation ice from the layer that has formed at

the surface.

Since we have defined congelation ice growth to start when the grease ice has reached 70% solid ice fraction, we calculate the initial bulk salinity S_{bulk} of the sea ice from

$$\phi = 1 - \frac{Sbulk}{S} \tag{4.1.18}$$

to be $S_{bulk} = 0.3S$, where S is the ocean salinity.

Once we have entered the congelation growth stage, we model the sea ice using the mushy layer equations, from section 2.4, so that the temperature equation is given by

$$c_{\text{eff}} \frac{\partial T}{\partial t} = \frac{\partial}{\partial z}\left(k_{\text{eff}} \frac{\partial T}{\partial z}\right). \tag{4.1.19}$$

Ice growth at the ice-ocean interface is determined from

$$\rho_i \mathcal{L} \phi \frac{dh}{dt} = k_i \frac{\partial T_i}{\partial z} - F_{ocean}, \tag{4.1.20}$$

$$\phi S \frac{dh}{dt} = \nu_T \frac{\partial S}{\partial z} + F_{brine}, \tag{4.1.21}$$

and

$$T_w = T_0 - \Gamma S_w, \tag{4.1.22}$$

where $\phi = 1 - S_{bulk}/S$ is the solid fraction at the ice-ocean interface.

In the water below the ice layer, even though we have stopped frazil ice formation, we are still interested in the temperature and the salinity of the water. We keep the same governing equations for temperature and salinity, but we now change the boundary conditions accordingly. The ice-ocean interface temperature is at the freezing point. Salt can now enter the water in two different ways: salt is released from ice growth, which we can calculate from the volume of ice formed, and natural convection can cause brine to be

released from the ice through brine channels. We can define the boundary condition then as

$$\nu_T \frac{\partial S}{\partial z} = \phi \frac{dh}{dt} S + F_{brine}, \qquad (z = 0) \tag{4.1.23}$$

where F_{brine} is defined as in section 2.5.

4.2 Reference Run

We will now show the results from a reference run of the model described so far. We use the initial ocean temperature and salinity profiles as given in fig 4.1, and choose constant atmospheric parameters $F_{LW} = 168$ Wm^{-2}, $F_{SW} = 0$ Wm^{-2}, $U_w = 5$ ms^{-1}, $T_a = 249$ K and $q_a = 5 \times 10^{-4}$. We consider ice growth within a lead of width $L_{lead} = 150$ m.

As previously mentioned, the model can be split into three stages, defined by the formation of frazil ice, grease ice and congelation ice, respectively. We define the time at which the ice cover reaches 95% ($a_{cover} = 0.95$) as T_1, and the point at which the grease ice solid fraction ϕ_g reaches 70% as T_2.

For the first stage, we look at the frazil ice concentration, and the temperature and salinity of the water. Figure 4.2 shows the ice concentration in the mixed layer during the first 2 hours. The ice cover forms at about $T_1 = 2.3$ h, which defines the end of the first stage. One may see from the ice concentration plots that the top 4–5 m are well mixed. This happens because the water becomes cooler near the surface which increases the density and leads to an unstable density profile, causing vigorous mixing.

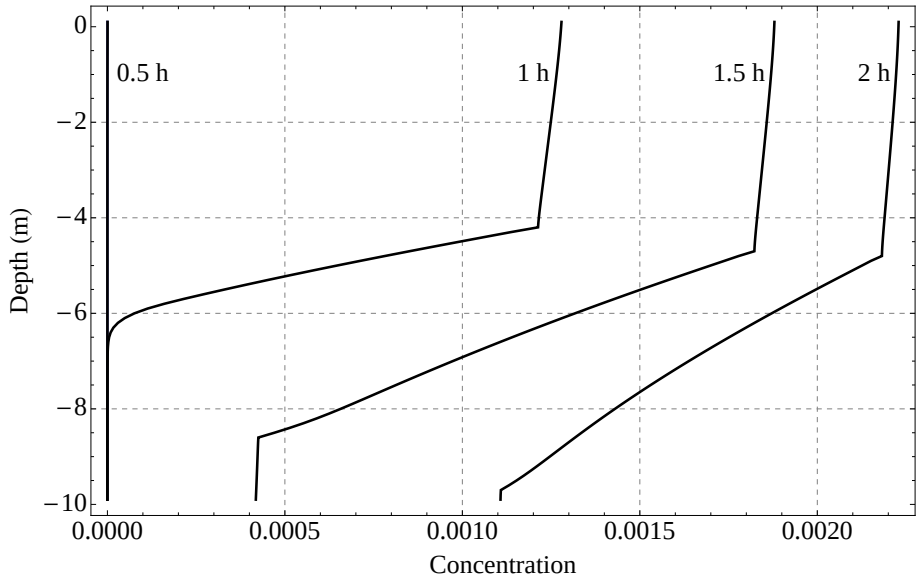

Figure 4.2: Frazil ice concentration in top 10 m at regular intervals during the first 2 hours.

Figure 4.3 shows the upper 10 m water temperature, which also becomes more mixed with time. Within one hour, the temperature has decreased and the profile is approaching that of the freezing temperature with depth. The profile is likely to remain close to that profile since any heat being lost at the surface is being quenched by new frazil ice formation.

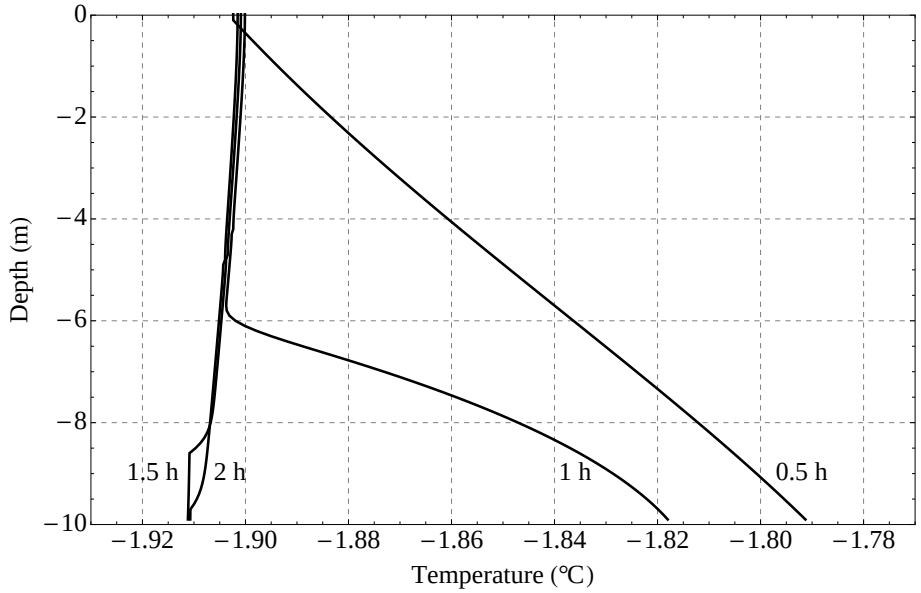

Figure 4.3: Water temperature in top 10 m at regular intervals during the first 2 hours.

Figure 4.4 shows the water salinity in the top 10 m. As expected, the profile becomes

well mixed as ice is forming. The salinity at the bottom of the mixed layer is decreasing, but this is due to the mixing, and the total salinity in the layer is increasing due to salt bring rejected from new ice being formed.

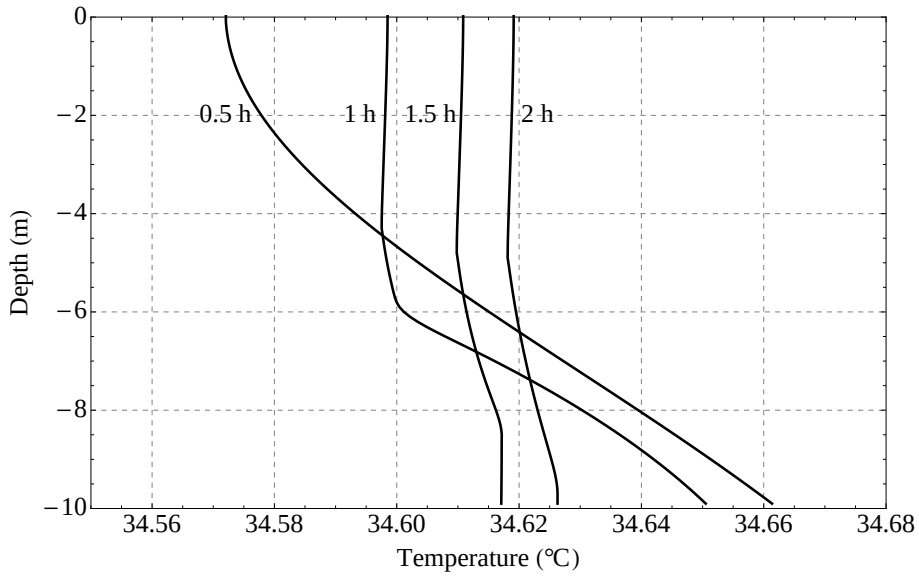

Figure 4.4: Water salinity in top 10 m at regular intervals during the first 2 hours.

As frazil ice is forming, we calculate the volume of ice which is precipitating out of the mixed layer. Figure 4.5 shows the total precipitation. Using equation (4.1.15), we can calculate that the ice cover a_{cover} reaches 95% when $V_p = 4.35 \times 10^{-2}$ m^3 . In Figure 4.6 we plot the grease ice cover a_{cover} until it reaches 0.95 at T_1.

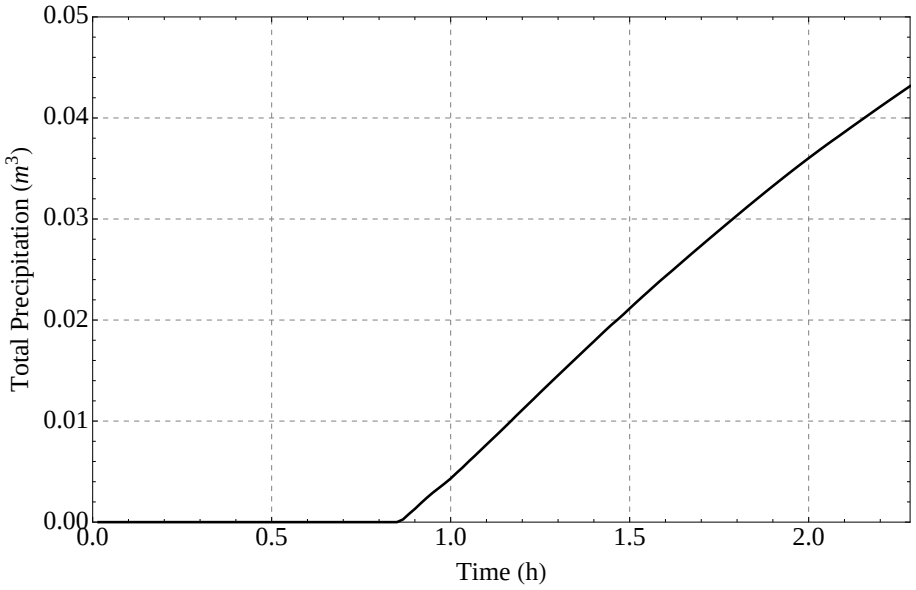

Figure 4.5: Total precipitation until T_1. The precipitation rate is approximately constant at 8×10^{-6} m/s per unit cross-sectional area.

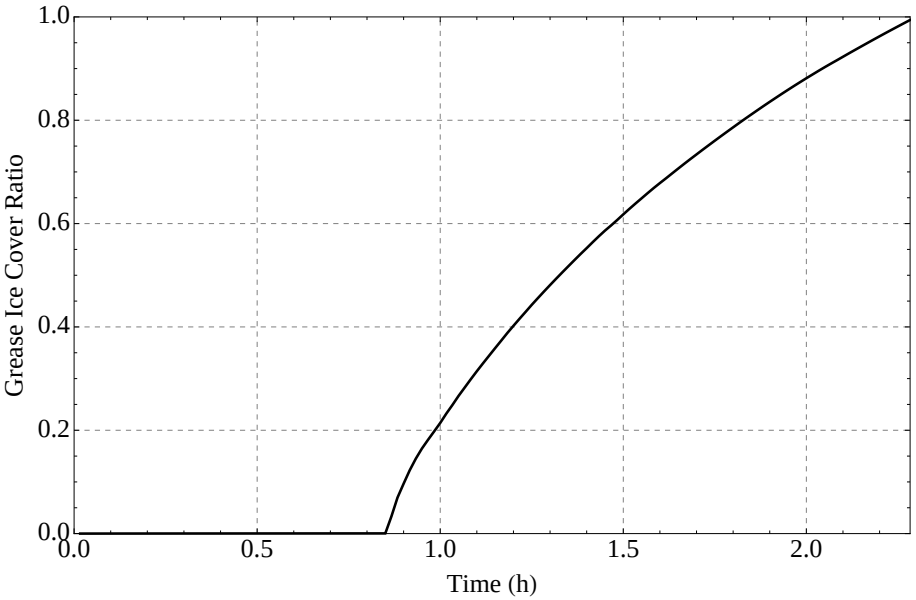

Figure 4.6: Grease ice cover until T_1.

Since we have assumed that grease ice forms at 25% solid fraction, only once we reach T_1 is when we switch off frazil ice production and let the grease ice solid fraction grow until it reaches 70%. Using (4.1.17), we calculate that this happens at $T_2 = 21.7$ h. In figure 4.7 we can see the grease ice solid fraction throughout the second and third stages with T_1 and T_2 indicated. We can see the second stage when grease ice is forming due to heat loss at

the surface, and after T_2 the solid fraction keeps growing due to the decreasing bulk salinity.

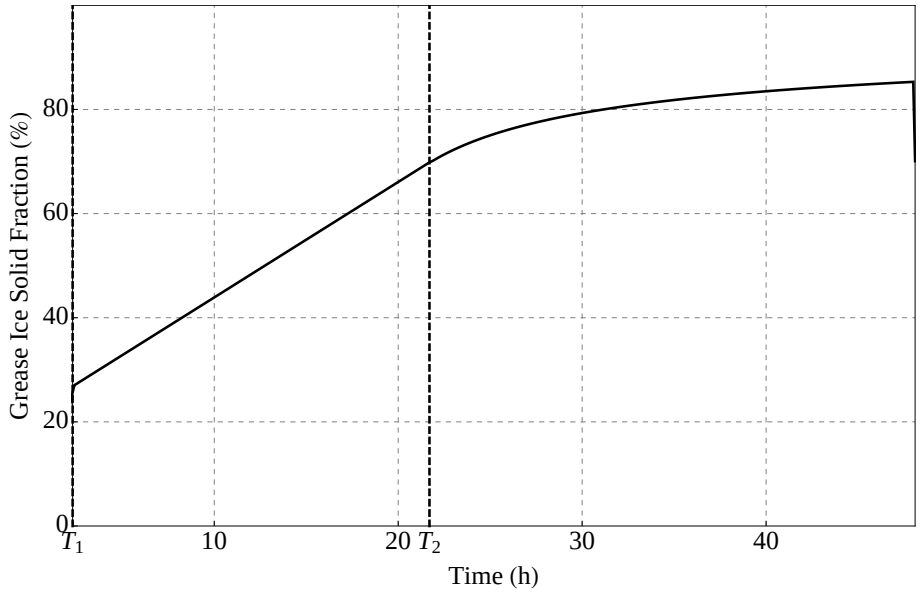

Figure 4.7: Grease ice solid fraction until T_1.

During the third stage, frazil ice has stopped forming and the ice layer has fully formed so we allow the ice to grow downwards according to the mushy layer equations. Figures 4.8 and 4.9 show the ice thickness and ice growth rate during the period dominated by congelation ice growth. They show that the ice growth rate slows down as the ice thickens, which is to be expected, and that the ice grows about 5 cm in the period of the next 24 hours after the model begins.

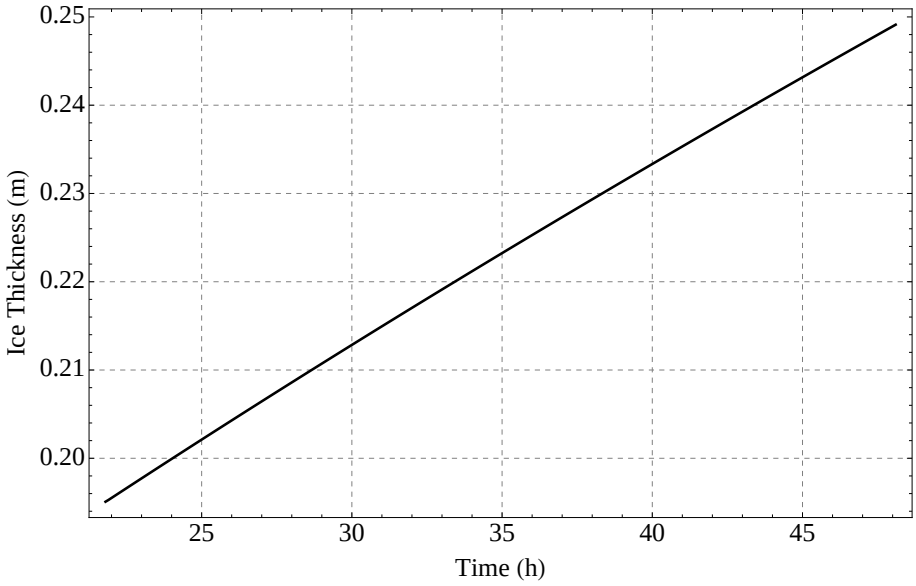

Figure 4.8: Ice thickness from T_2 to 48 h.

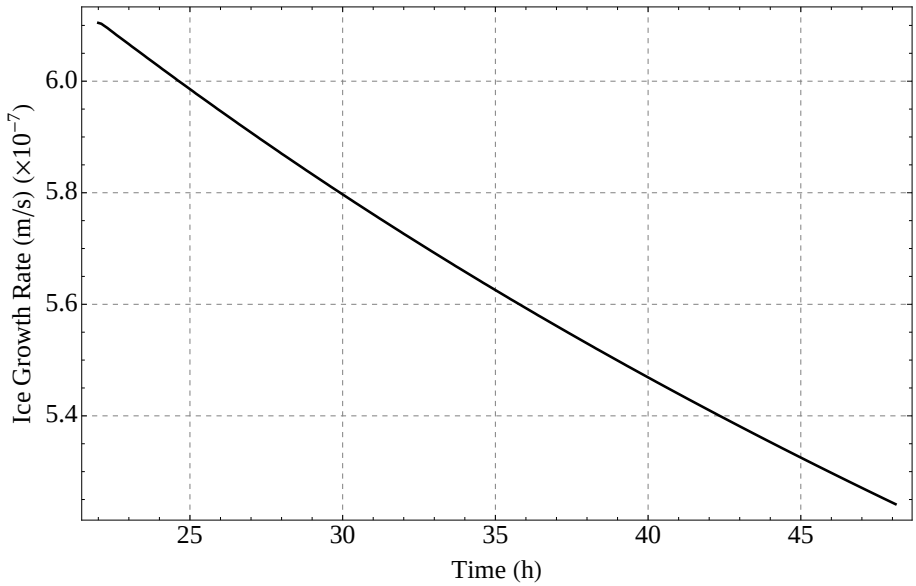

Figure 4.9: Ice growth rate from T_2 to 48 h.

During this period, the changes to the water below the ice are dominated by the downwards flux of salt from the sea ice growth. This happens in two ways, firstly by salt being rejected from the ice growing, which we call brine expulsion, and secondly by the formation of brine channels that release brine from within the sea ice. The upper boundary condition of salinity is

$$\nu_T \frac{\partial S}{\partial z} = \phi S \frac{dh}{dt} + F_{brine} \tag{4.2.1}$$

where the first term on the right side represents the brine expulsion, and the second term represents brine drainage, as defined in equation (2.5.1) . Figures 4.10 and 4.11 show the rate and total release of salt through brine expulsion. The rate is calculated from the first part of the previous equation, and the reason it remains close to constant is that although $\frac{dh}{dt}$ is decreasing, ϕ is increasing due to a lower bulk salinity, and S is also increasing due to more salt being released into the water.

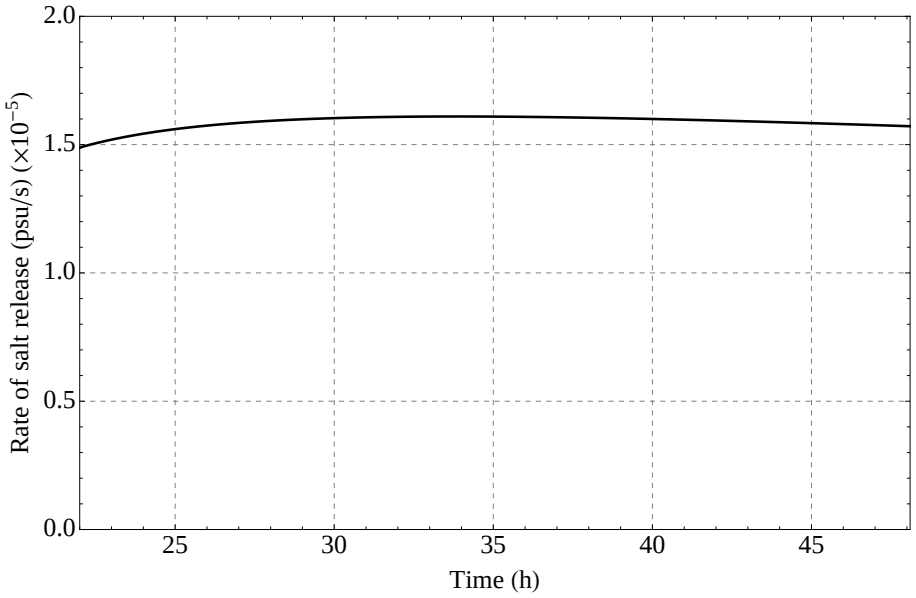

Figure 4.10: Ice growth salt release from T_2 to 48 h.

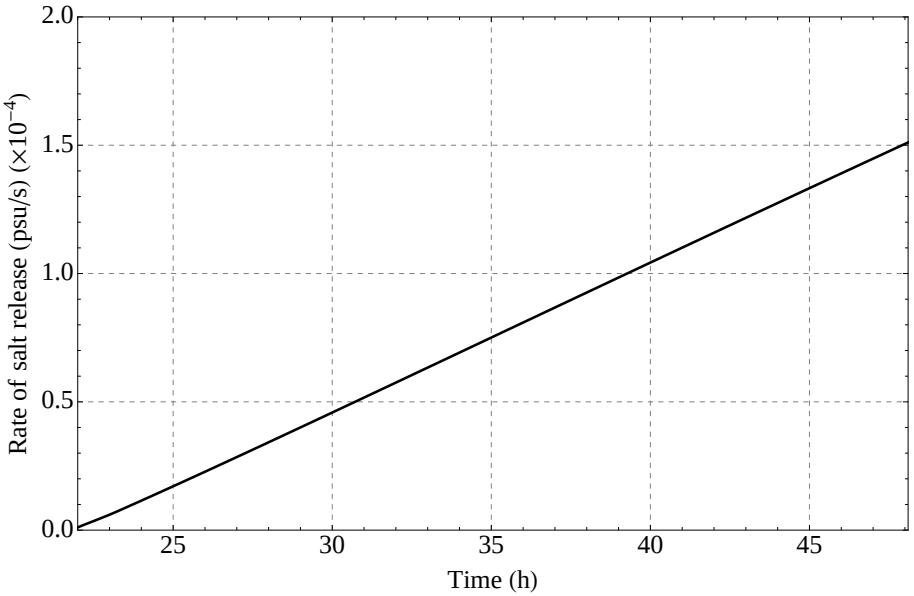

Figure 4.11: Total ice growth salt release from T_2 to 48 h.

Figures 4.12 and 4.13 show the rate and total release of salt from brine channels. The rate quickly decreases because the permeability is very sensitive to the solid fraction, which is decreasing due to the decreasing bulk salinity. It is interesting to note that during the first 6 hours, the leading process is brine channels, and then it becomes release from the ice growth. If run for enough time, the brine channels would eventually stop releasing brine, which would happen in equation (2.5.1) when $R_m < R_c$.

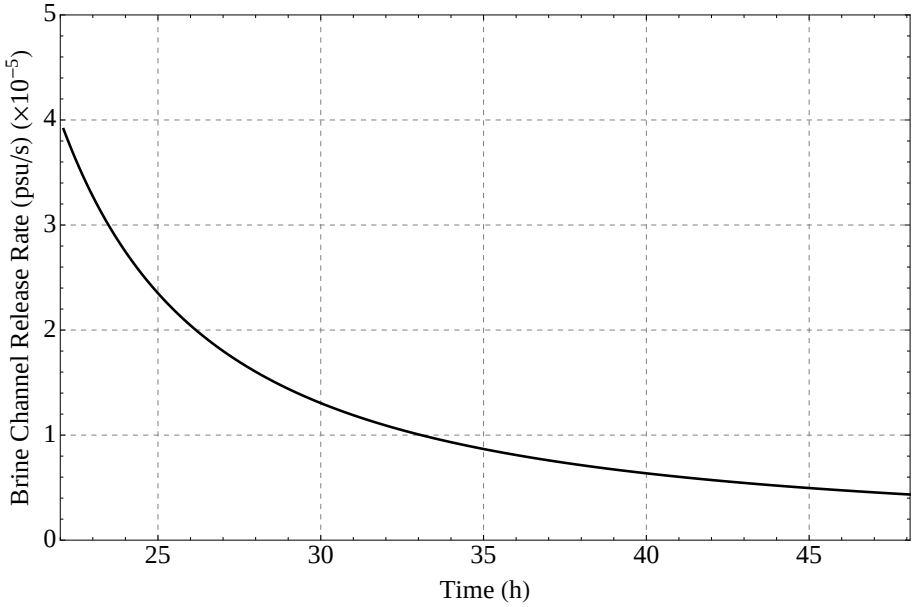

Figure 4.12: Brine channel release rate from T_2 to 48 h.

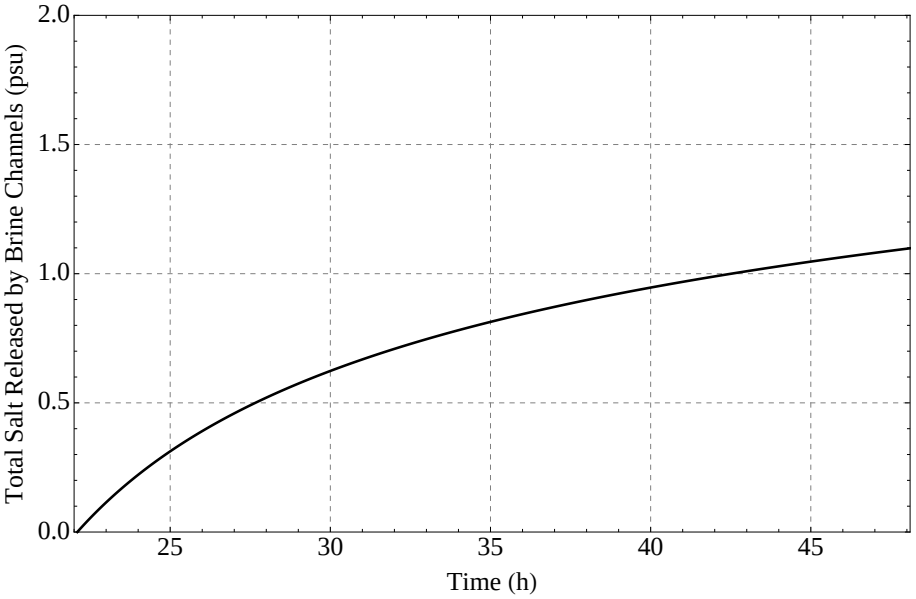

Figure 4.13: Total brine release from T_2 to 48 h.

4.3 Dmitrenko et al (2010)

Dmitrenko et al (2010) studied the formation of a polynya, namely the Laptev Sea polynya in the Arctic. Using a range of measurements including radar from Envisat and satellite imagery from TerraSAR-X, they captured a polynya event from start to finish and made

measurements of the water salinity and temperature profiles from a mooring attached to the fast-ice edge.

Since our model is 1D and does not account for ice being driven away from the surface or horizontal advection of ice by ocean currents like a polynya, we modified our model to include heat loss and frazil ice formation, but we do not allow an ice cover to form.

The Siberian continental shelf undergoes several changes in the winter due to seasonal sea-ice formation. The katabatic winds coming offshore from Siberia create areas of open water off the land-fast ice, such as the Great Siberian Polynya. One such polynya was formed in the southeastern Laptev Sea at the end of April 2008.

In summer, due to the river run-off from the Lena River and seasonal ice melting, the salinity of the surface waters in the southeastern Laptev Sea are relatively low ($\sim$5-15 psu, Dmitrenko et al (2010)). In winter there is considerably less river inflow and sea ice formation, which leads to a summer-to-winter salinity difference of $\sim$5 psu.

Between April and May 2008, 5 moorings were placed along the land-fast ice edge contouring the perimeter of the polynya. Each mooring carried equipment to detect conductivity, temperature and pressure in the surface layer and at the bottom water layers. CTD profiles were also measured periodically at the mooring locations. 26 images from Envisat and 10 from TerraSAR-X were also acquired. The scattering signatures of newly formed sea-ice, polynya open water, frazil ice and land-fast ice edge are different, and are distinguishable on the SAR images. Four of the moorings used AWS (automated weather stations) to pick up on the meteorological data with high temporal resolution. One of the mooring's AWS was attacked by polar bears and so Global Digital Analyses from the German Meteorological Service were used to fill the gap.

After observing the area from the 20th April, there were three possible polynya inducing wind events, on the 16-18 April, 22-23 April and 26-30 April. Only during the last one

was a polynya actually created, starting on the 30th April and lasting until the 1st May. High-resolution simulations with the atmospheric model COSMO (Consortium for Small-Scale Modelling) found that the total oceanic heat flux around that time was between 300 and 550 W m^{-2}. The opening of the polynya is also clearly visible in the satellite images from 30 April, when the air temperature was about -12 °C.

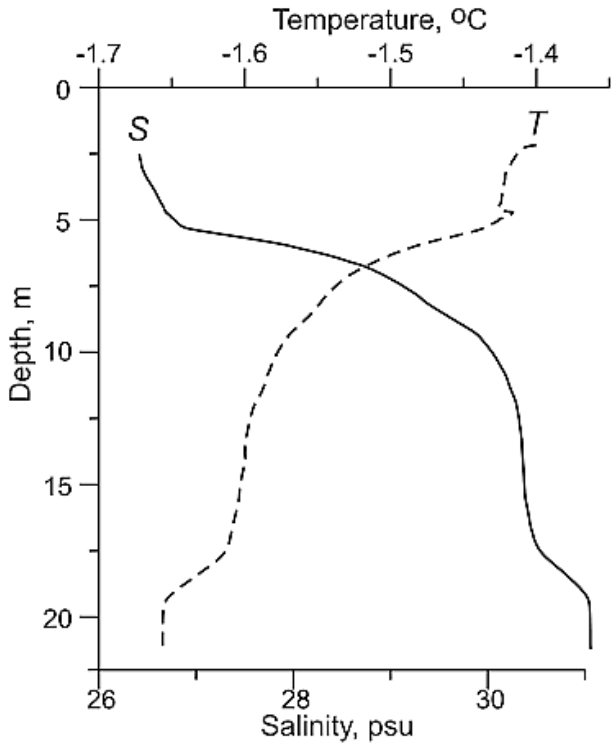

Figure 4.14: Vertical Profiles of temperature (dashed) and salinity (solid) taken on 24 April before the polynya forms.

Fig 4.14 shows the initial temperature and salinity profiles before the formation of the polynya on the 24th April. The mixed layer is shown to go down to about 6 metres, where the salinity and temperature are relatively uniform. The salinity difference from the mixed layer to the bottom water is due to the summer river runoff. The temperature at the surface is still not supercooled at this point and is ∼0.03°C above the salinity dependent freezing temperature.

Using acoustic Doppler current profilers (ADCPs) attached to the moorings, frazil ice

crystals can be detected, but no values of frazil concentration were obtained due to a missing calibration, and also crystals can only be detected if they are greater that ∼1.5 mm of diameter, which is larger than most crystals in observations, and therefore in our model.

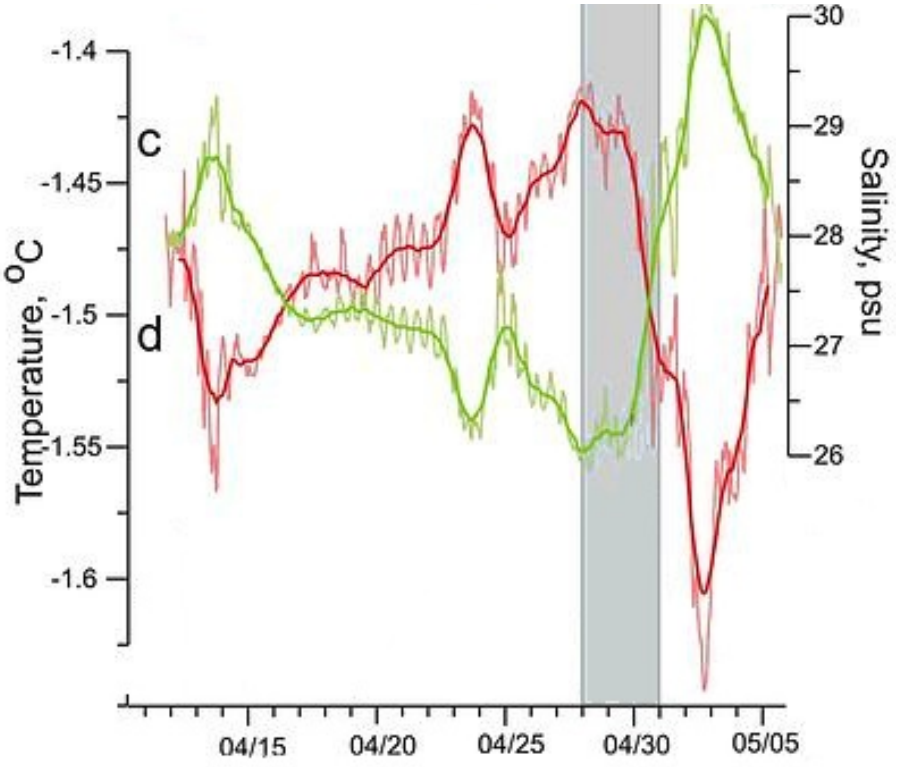

Figure 4.15: M2 mooring time series from 11 April to 5 May 2008. The red line represents the water temperature at 4.5 m, and the green line represents the salinity at 4.5 m. The period highlighted in blue is the polynya event, starting on the 28th April and ending on the 1st May.

In order to model this situation, we made changes to our model to account for a more realistic scenario in the south Laptev sea. The air temperature and heat flux data were mentioned earlier as being -12°C and 300-550 W m^{-2}. The wind speed is measured as being between 5 and 7 m s^{-1}, and the air humidity is taken from ERA reanalysis data. The mixed layer depth is set to 6 m, with high turbulent diffusivity of $\nu_T = 1 \times 10^{-2}$ there, to account for high mixing. Below the mixed layer the turbulent diffusivity is a lot lower ($\nu_T = 1 \times 10^{-5}$). The initial profiles of temperature and salinity are taken from figure 4.14.

Figure 4.15 shows the time series of temperature and salinity during about three weeks in April and May, with the three days corresponding to the polynya event highlighted. Assuming that the mixed layer is well mixed, these values taken at 4.5 m can be assumed to be the same throughout the whole mixed layer. As expected the salinity increases as frazil ice is formed and releases salt, and consequently the freezing temperature decreases. This, along with the fact the heat is being lost at the surface continually account for the decrease in temperature. The observed values show a decrease in temperature of about $\sim$0.1°C (from about -1.42°C to -1.52°C), and a rise in salinity of $\sim$2 psu (from 26 psu to 28 psu). The results from our model are similar to these values. We found a final temperature of about -1.518°C and a salinity of about 27.9 psu. In figure 4.16 you can see that the temperature and salinity time-series are close to linear unlike the observations, but that is to be expected from an idealized model, where parameters such as wind speed and heat fluxes are kept constant throughout. Although the observations can provide only a limited test of our model, the consistency in the temperature and salinity evolution lends us some confidence in the model.

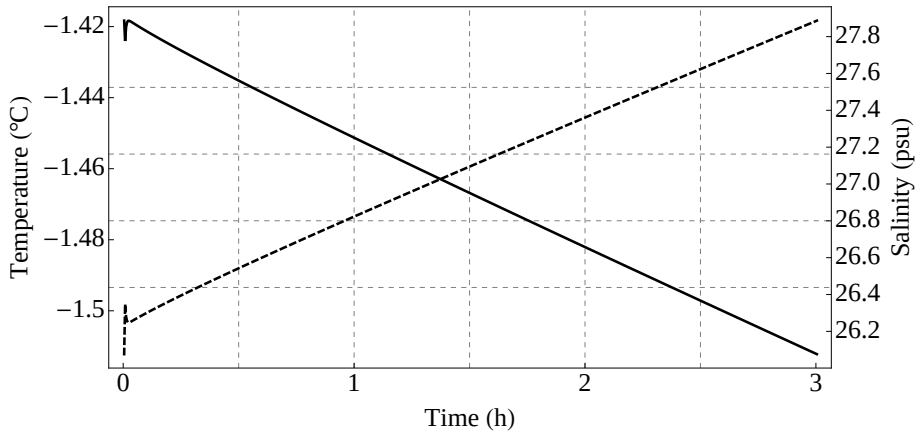

Figure 4.16: Temperature and salinity in the mixed layer during the three days of the polynya event.

5 Sensitivity Studies

In this chapter we will vary some of the more important forcings and parameters of our model, and compare the results to our reference run, which will allow us to make some conclusions on how important the varying parameter is to the model. Table 7 shows a summary of the results from six different sensitivity studies, where we vary wind speed (1 & 2), air temperature (3 & 4), initial water salinity temperature (5 & 6), lead width (7 & 8), longwave radiation (9 & 10) and air humidity (11 & 12). T1 represents the time it takes for an ice cover of precipitated frazil ice to form and T2 represents how long it takes for the grease ice to reach a solid fraction $\phi_g = 70\%$.

During the analysis of these sensitivity studies, what we realised was the time it takes for ice to first start forming, what we called the 'delay', was mainly caused by the secondary nucleation and the parameterization we had used for it. This is shown in the values of $T1'$ and $T2'$ of table 7, which are the times taken to form an ice cover and for the solid grease ice to reach 70% in the same scenarios, but by increasing the secondary nucleation parameter a_{nuc} from a value of 1×10^{-3} to 1. The times are reduced in all cases, in some cases dramatically. This happens because of the nonlinearity of the secondary nucleation formulation, that somewhat non-intuitively depends on the forcings. Since there is some uncertainty in this process, when looking at the results, we mostly interpret results after the secondary nucleation kicks in, and ice starts forming.

The results of the reference run, shown in table 7, are also affected by the delay, which is about 0.9 hours in this case. Since the time difference between T1 and T2, when grease ice solid fraction is increasing at a constant rate, remains the same in both cases, the delay of 0.9 hours can also be seen in the difference between T2 and T2'. The overall effect is that less ice will be formed since, as we will see in the sensitivity studies, the rate of ice formation is higher during the first phase when the ocean is in contact with open water, than later on when congelation ice is growing beneath the ice.

The delay in the formation of frazil means that even though the water is supercooled enough to form ice, since the secondary nucleation is not strong enough to create ice, the water becomes more supercooled than it normally would. Once ice starts forming and there are enough nucleii to form more ice, this supercooling will get quickly quenched, and ice will form at a faster rate than it normally would. Once a quasi-steady state is formed where the amount heat lost at the surface is the same amount of heat released from ice formation, the effect of the initial delay will no longer be felt as the total ice formed should be the same, except that it will happen slightly later in the delay case.

With regards to the sensitivity studies, since the delay only affects up to about 1 hour of the run, we felt that over 48 hours, the effects of the delay were small enough that it would not affect the results qualitatively much, and so used the results with the delay, so that we were comparing the reference run with results on the same basis.

	Simulation	T1 (h)	T1' (h)	T2 (h)	T2' (h)	H (cm)
0	Reference	1.9	1.0	21.7	20.8	24.58
1	$U_w = 10$ m/s	2.6	1.7	26.8	25.9	40.69
2	$U_w = 2.5$ m/s	1.0	0.5	15.6	15.1	17.31
3	$T_{air} = -15$ °C	1.6	1.0	27.0	26.4	22.19
4	$T_{air} = -35$ °C	2.9	1.0	19.2	17.3	26.96
5	$S_w = 44.5$ psu	1.9	1.1	22.2	21.4	24.69
6	$S_w = 24.5$ psu	1.9	0.9	21.3	20.3	24.60
7	$L_{lead} = 50$ m	1.6	0.7	13.0	12.1	20.20
8	$L_{lead} = 250$ m	2.1	1.2	27.8	26.9	28.21
9	$F_{LW} = 100$ W/m^2	3.1	1.0	19.9	17.8	25.45
10	$F_{LW} = 240$ W/m^2	1.6	1.0	26.2	25.6	23.40
11	$q_a = 2.5 \times 10^{-3}$	1.6	0.9	24.1	23.4	23.25
12	$q_a = 1 \times 10^{-4}$	1.9	1.0	21.3	20.4	24.80

Table 7: Sensitivity studies from varying several parameters. T1 is the time taken to form an ice cover, and T2 is the time taken for the grease ice solid fraction to reach 70%. T1' and T2' are the equivalent times when we use a higher secondary nucleation parameter.

5.1 Varying wind speed

Wind speed affects our model in several ways. Firstly, the wind speed affects how the frazil ice builds up at the sea ice edge, and hence the collection depth. This is the maximum depth we assume the grease ice forms at. This means that if the wind speed is higher, the collection depth will be larger and this will create a thicker grease ice layer. Another way in which the wind speed affects the model is that the sensible and latent heat parameterization depend on wind speed directly, and so if the wind speed doubles, so do the sensible and latent heats. Since increasing wind speed will create a thicker collection depth and will increase the heat fluxes at the surface, we might expect a larger wind speed to create more frazil ice and take longer to fully cover with grease ice.

As mentioned in Chapter 2, the turbulent diffusivity in the mixed layer does not depend on the wind speed and is defined to be constant. In reality, the higher wind speed would cause more mixing and the lower wind speed would cause less mixing. This would affect the results by releasing heat faster, but also by keeping the frazil crystals from precipitating to the surface as easily. Overall it would potentially mean that even more ice would form in the higher wind speed case and less ice in the lower wind speed case.

Our reference run has a wind speed of $U_w = 5$ m/s, and we ran two new simulations where we doubled the wind speed to $U_w = 10$ m/s and halved the wind speed to $U_w = 2.5$ m/s.We now discuss the results and show the relevant plots.

As a higher wind speed has a larger collection depth, the run which takes the longest to form a complete ice cover is the case with the highest wind speed and conversely, the quickest is the case with the lowest wind speed which just takes over an hour to form, as shown in figure 5.1. One interesting point to note is the depth to which the ice concentration is very well-mixed, which is about 4 m in the reference run, but reaches 10 m in the higher wind speed and only 2 m in the lower wind speed. This happens because the higher the wind speed, the more turbulence there is in the water, which causes more mixing.

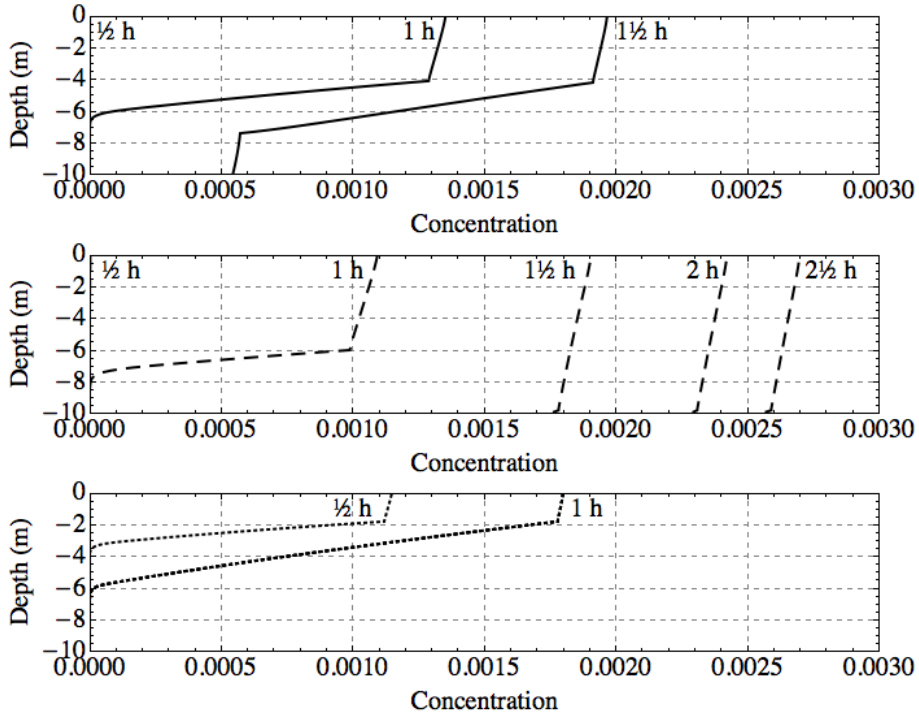

Figure 5.1: Frazil ice concentration plots until an ice cover forms. The top plot is the reference run ($U_w = 5$ m/s), the middle one is the higher wind speed ($U_w = 10$ m/s) and the bottom one is the lower wind speed ($U_w = 5$ m/s).

In figure 5.2 we see that the temperature profiles do not vary much. The temperature profile varies more in the earlier stages, as the profile after 30 minutes is different for all three, but after an hour, the profiles look more similar.

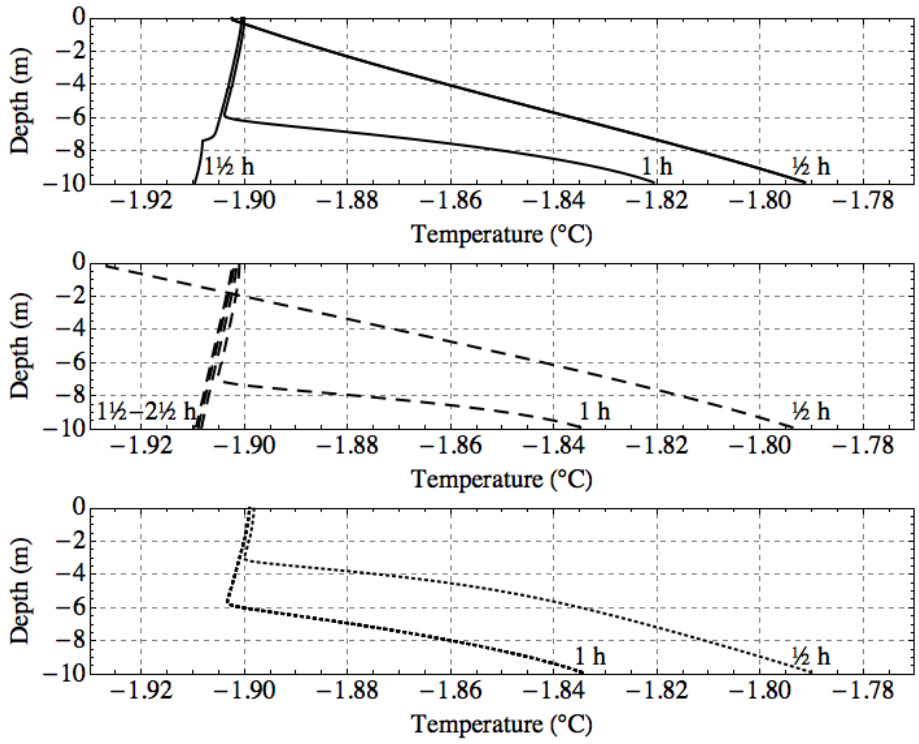

Figure 5.2: Water temperature profiles until an ice cover forms. The top plot is the reference run ($U_w = 5$ m/s), the middle one is the higher wind speed ($U_w = 10$ m/s) and the bottom one is the lower wind speed ($U_w = 5$ m/s).

Similarly to the temperature, and also because salinity and temperature are intrinsically linked, the salinity profiles do not appear to be affected very much by the different wind speeds, as shown in figure 5.3. The profiles are slightly different at the one hour mark, but not enough to account for any big changes in results.

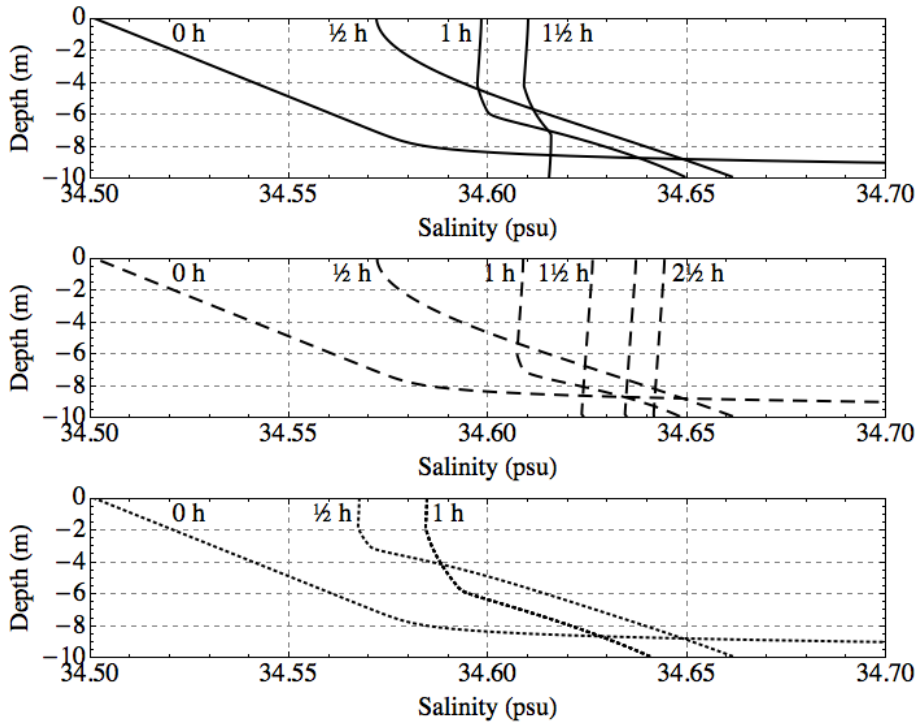

Figure 5.3: Water salinity profiles until an ice cover forms. The top plot is the reference run ($U_w = 5$ m/s), the middle one is the higher wind speed ($U_w = 10$ m/s) and the bottom one is the lower wind speed ($U_w = 5$ m/s).

Figure 5.4 shows the total precipitation of frazil ice out of the water column until an ice cover forms. Since the wind speed directly affects the collection depth, the amount of ice precipitated needed to form an ice cover is also directly proportional to wind speed, doubling for the higher wind speed and halving for the lower wind speed.

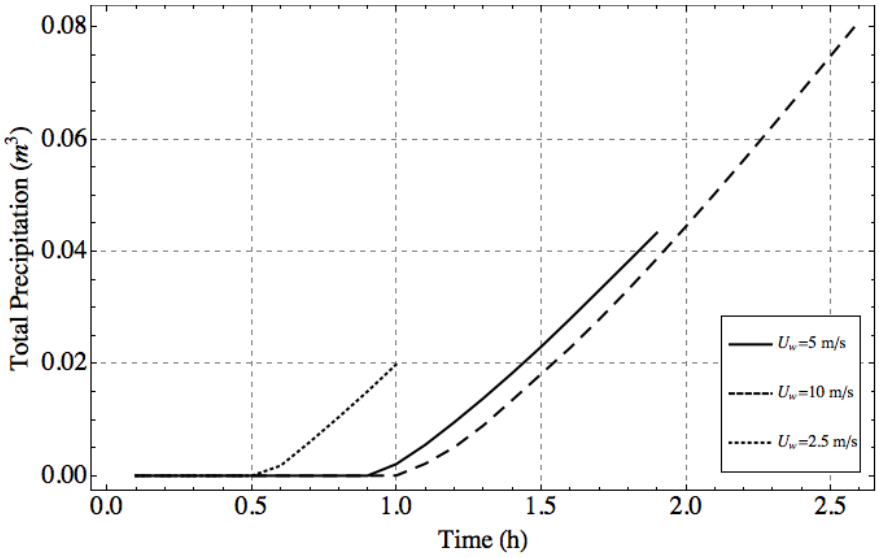

Figure 5.4: Total precipitation out of the water column until an ice cover forms.

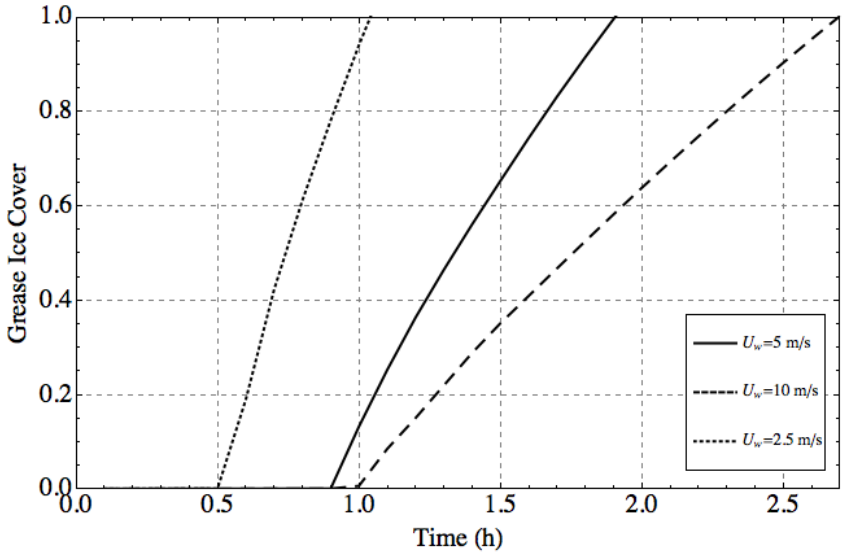

Figure 5.5: Grease ice cover until an ice cover forms.

In figure 5.5 we see the grease ice cover fraction from the beginning of the run until an full cover of grease ice forms. Since the mixing is lower in the lower wind scenario, the ice rises faster to the surface and starts forming the cover first. Conversely, the higher wind speed takes longer to start forming the ice cover. It also takes longer in this case since, as mentioned earlier, the collection depth is a lot larger.

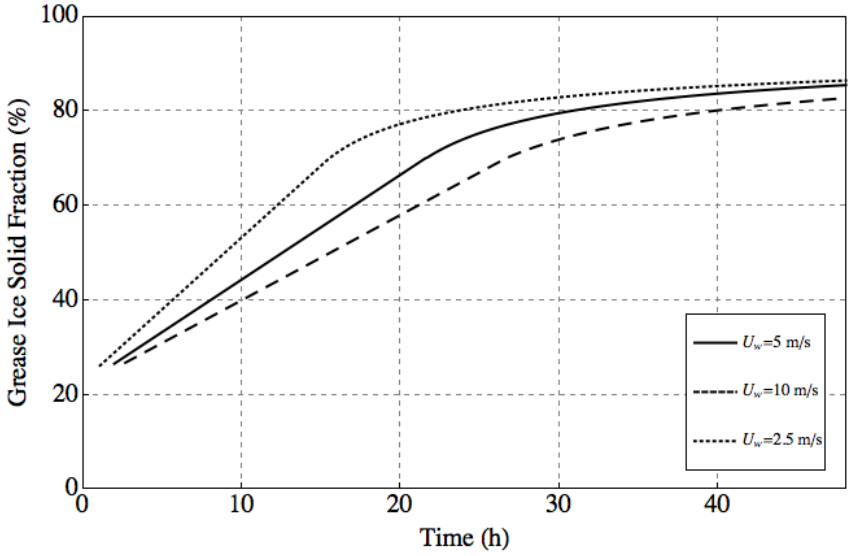

Figure 5.6: Grease ice solid fraction until 2 days of simulation.

Once the frazil ice has precipitated and formed an ice layer, we treat the mixture as grease ice and allow it to grow by letting the grease solid fraction increase, as shown in figure 5.6. Once the grease ice reaches a critical solid fraction of 70%, we assume the layer is now ice and allow growth from beneath as well as growth within the grease ice. This is why the gradient of the plots change when they reach a fraction of 70%. As the wind speed affects the rate at which heat is released from the water, the grease ice fraction growth rate is higher in the lower wind speed case, and conversely lower in the higher wind speed case. Even though the heat flux is higher with a higher wind speed, the grease ice layer is thicker, and so takes longer to reach the 70% fraction.

Once the grease ice cover reaches the required 70% for a solid layer, we let the congelation ice grow downwards, and measure the ice thickness, as shown in figure 5.7. The only mechanism for ice growth now is the heat lost through the ice from the water beneath, at a much lower rate than that through open water. Since the heat loss is higher in the higher wind speed case, the collection depth is larger in that case, and smaller in the lower wind speed. In figure 5.8 we see the ice growth rate. Although the higher wind speed cases have a larger surface heat loss, the thicker ice in these cases reduce the conductive flux at the base of the ice so that the ice growth is slower in these cases.

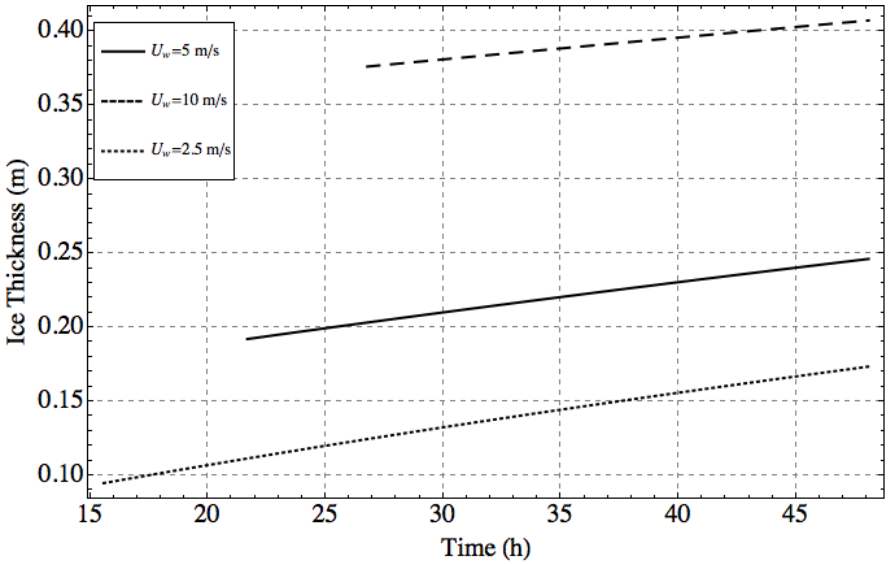

Figure 5.7: Ice thickness until two days of simulation.

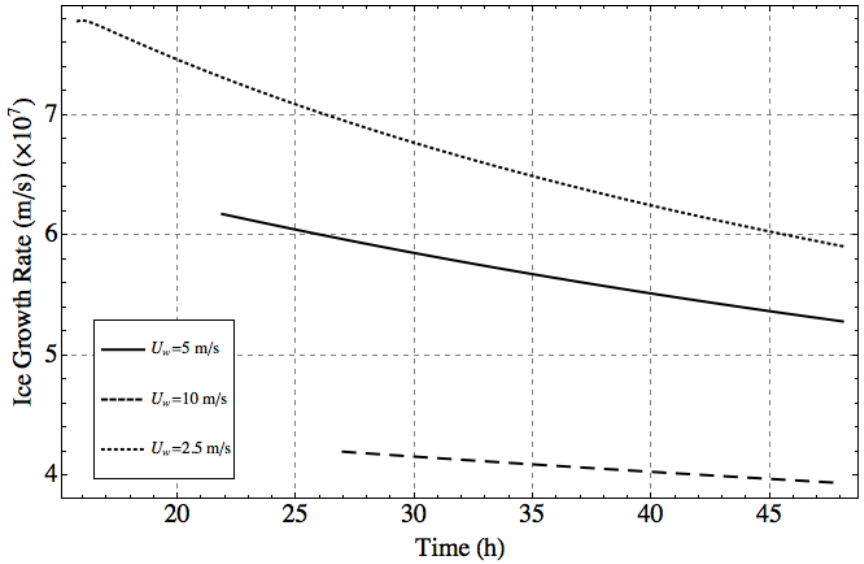

Figure 5.8: Ice growth rate until two days of simulation.

While the ice is growing, salt is released in two ways, through the formation of brine channels and from congelation ice formation rejecting the salt when it grows. Figure 5.9 shows the rate of salt release from brine channel formation. Since the ice starts growing first in the lower wind speed case, the release starts in that case first, and starts last for the higher wind speed. The brine channel salt loss rate, however, is larger in the higher wind

speed case, since the ice is thicker and there is more brine to release. Figure 5.10 shows the total salt released by brine channels. We can see from this that although the higher wind speed case starts releasing brine later, the total brine released is larger, as shown by the area under the curve.

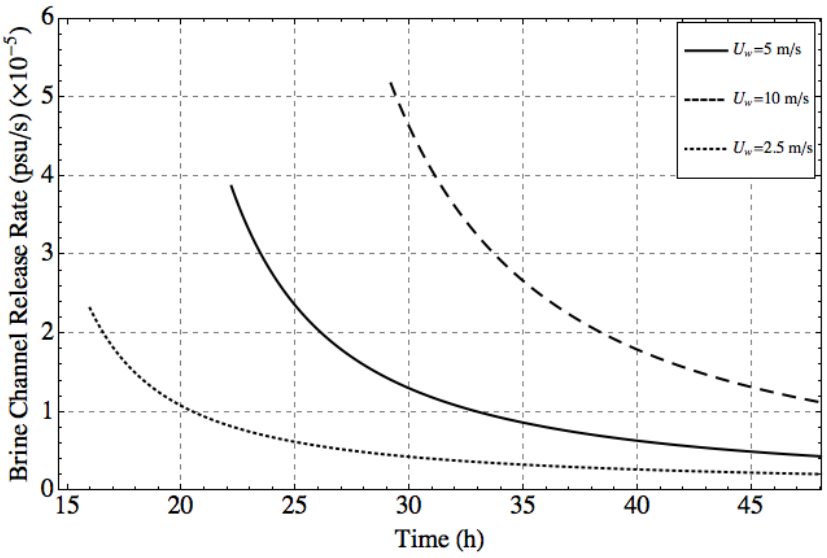

Figure 5.9: Brine channel release rate until two days of simulation.

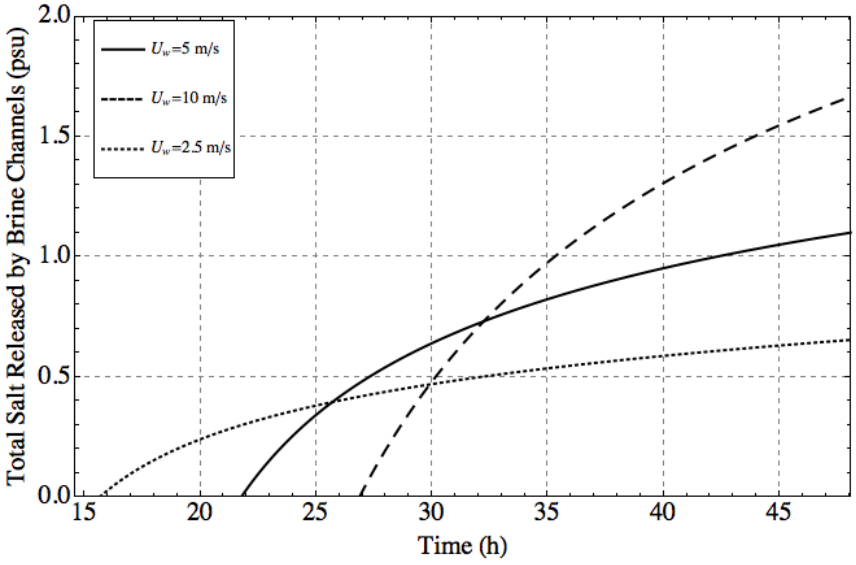

Figure 5.10: Total brine channel release until two days of simulation.

The other way in which salt is released into the water is through the congelation ice

rejecting salt into the water when growing. Figure 5.11 shows the rate of salt released in this way. Since it is directly related to the rate of ice growth, following on from figure 5.7, the lowest wind speed case has the highest rate and the highest wind speed case has the lowest. Since the lowest wind speed case also starts forming congelation ice first, the total salt released in this way is always higher, as shown in figure 5.12, and lower in the higher wind speed case.

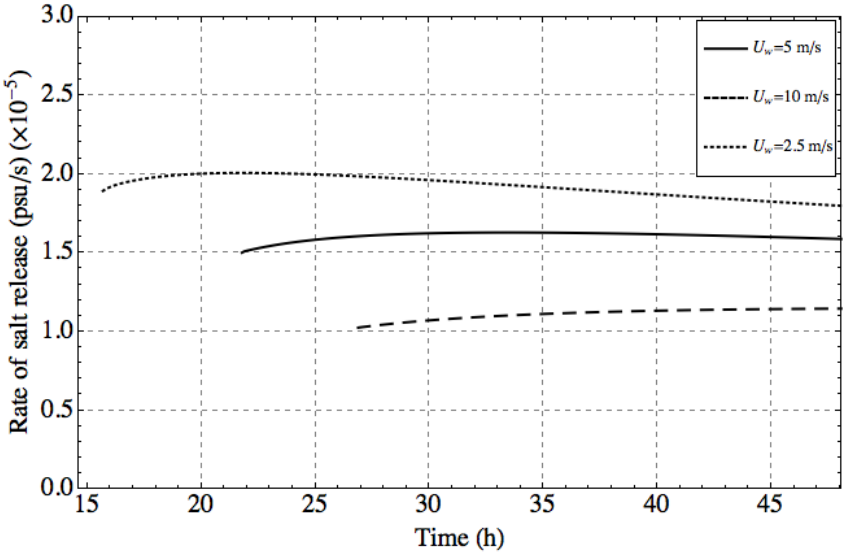

Figure 5.11: Rate of salt release from congelation ice formation until two days of simulation.

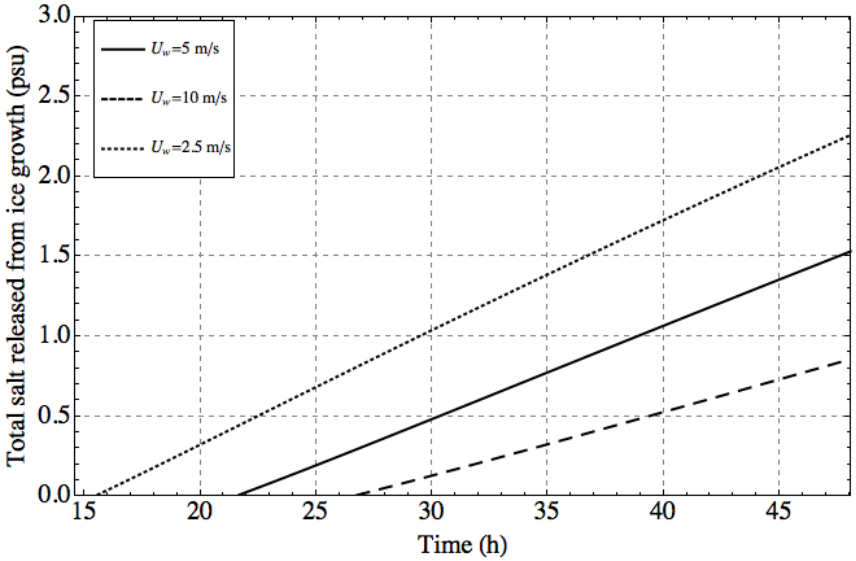

Figure 5.12: Total salt released from congelation ice formation until two days of simulation.

5.2 Varying air temperature

Air temperature affects our model because it changes the heat flux from the water to the air, hence increasing the amount of ice produced. The air temperature in the reference run was $T_{air} = -25°\text{C}$, and we ran two more simulations where we increased it to $T_{air} = -15°\text{C}$, and decreased it to $T_{air} = -35°\text{C}$ and compared the results from these with the reference run.

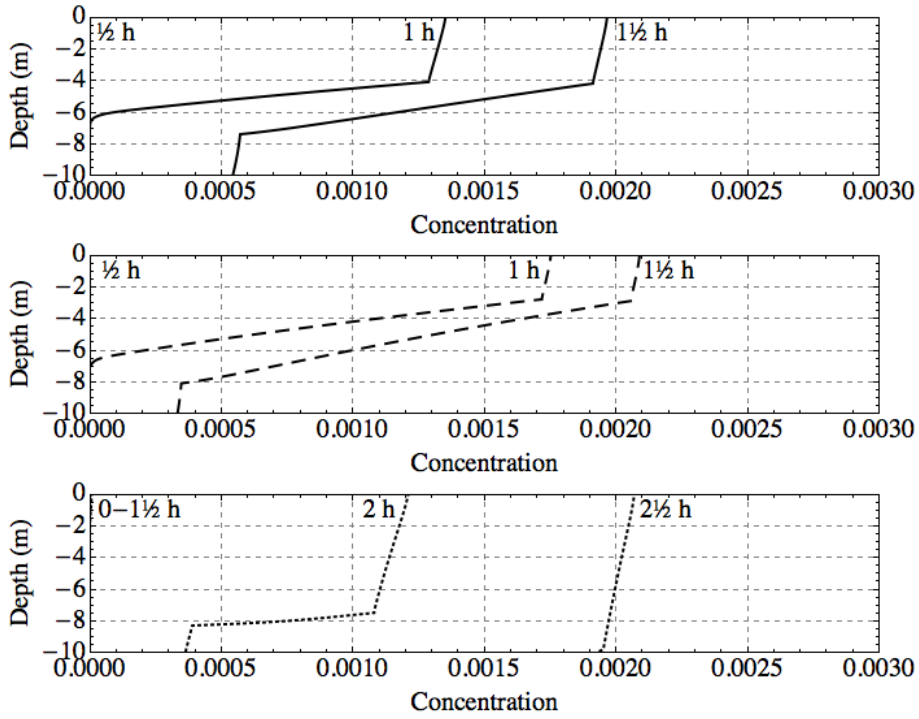

Figure 5.13: Frazil ice concentration plots until an ice cover forms. The top plot is the reference run ($T_{air} = -25°\text{C}$), the middle plot is the higher air temperature ($T_{air} = -15°\text{C}$) and the bottom plot is the lower air temperature ($T_{air} = -35°\text{C}$)

Figure 5.13 shows the concentration plots for the three simulations. We can see from the plots that the lower the temperature, the longer it takes for ice to start forming, and ice does not start forming in the bottom plot until after 1.5 hours. This delay in the ice beginning to form leads to a time T_1 which is inversely proportional to the air temperature (as seen in table 7).

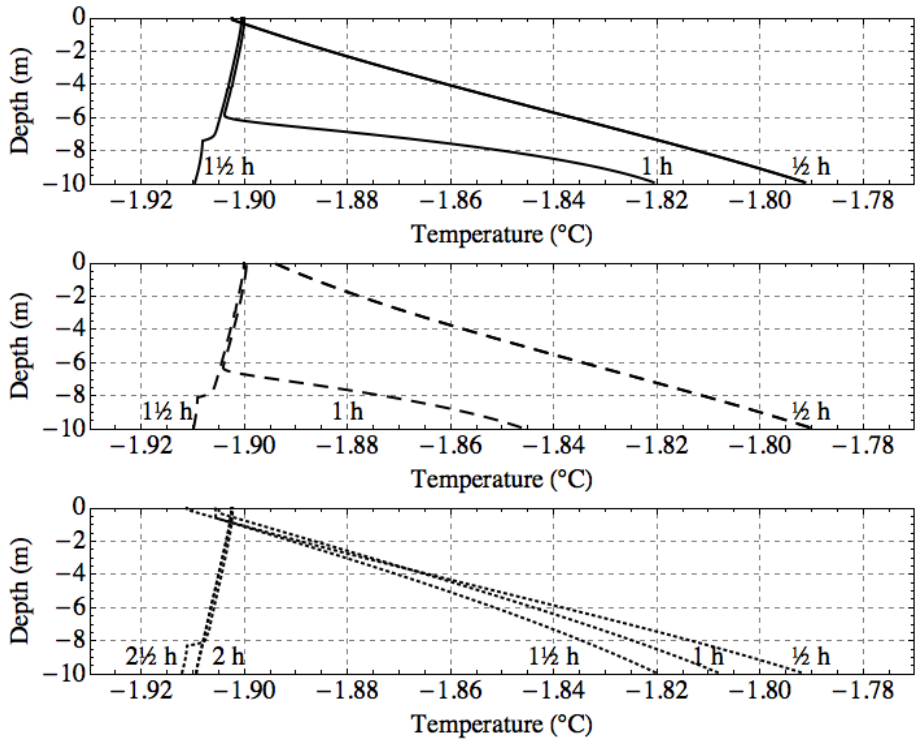

Figure 5.14: Water temperature profiles until an ice cover forms.

Figure 5.14 shows the temperature profiles for the three simulations. As expected, they do not vary much except near the surface.

The salinity profiles are shows in figure 5.15 and, similarly to the temperature, they do not vary too much except slightly near the surface after about 1.5 hours.

Figure 5.16 shows the total precipitation until we reach T_1. As mentioned earlier, the lowest air temperature takes the longest to start forming ice, but the rate of precipitation is relatively constant for all three cases.

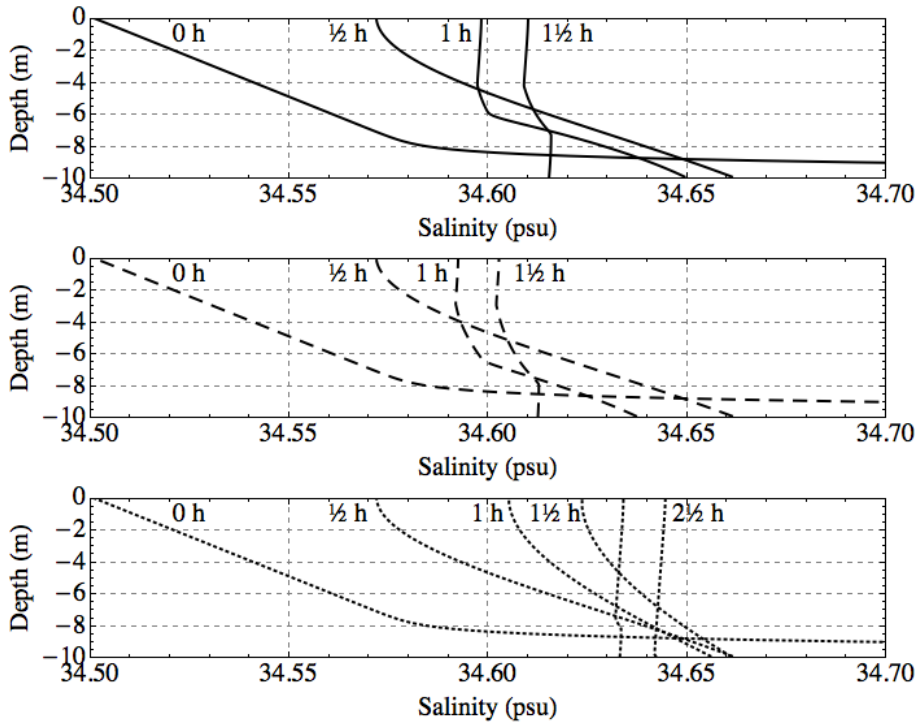

Figure 5.15: Water salinity profiles until an ice cover forms.

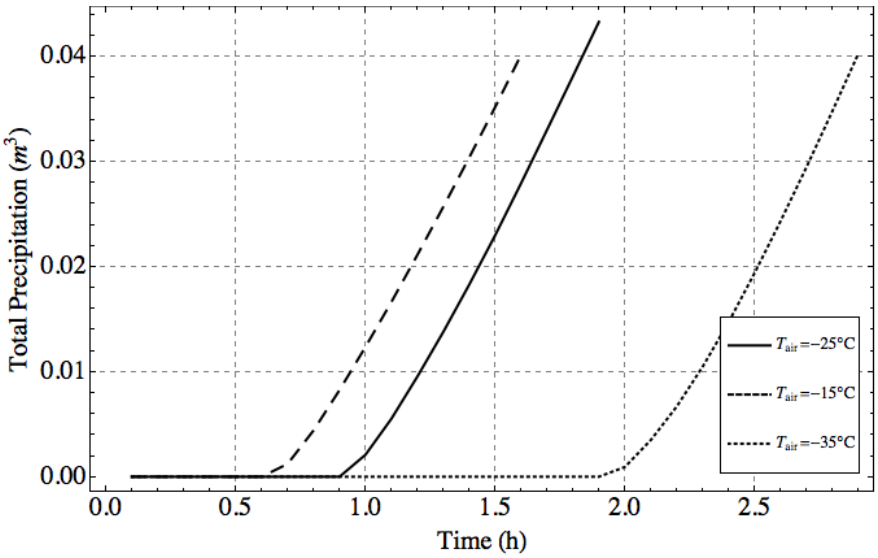

Figure 5.16: Total precipitation out of the water column until an ice cover forms.

Figure 5.17 shows the fraction of the surface covered in grease ice, which relates to the total ice precipitated, since when ice precipitates to the surface it adds to the grease ice layer there and increases the solid fraction, hence the similarity to figure 5.16.

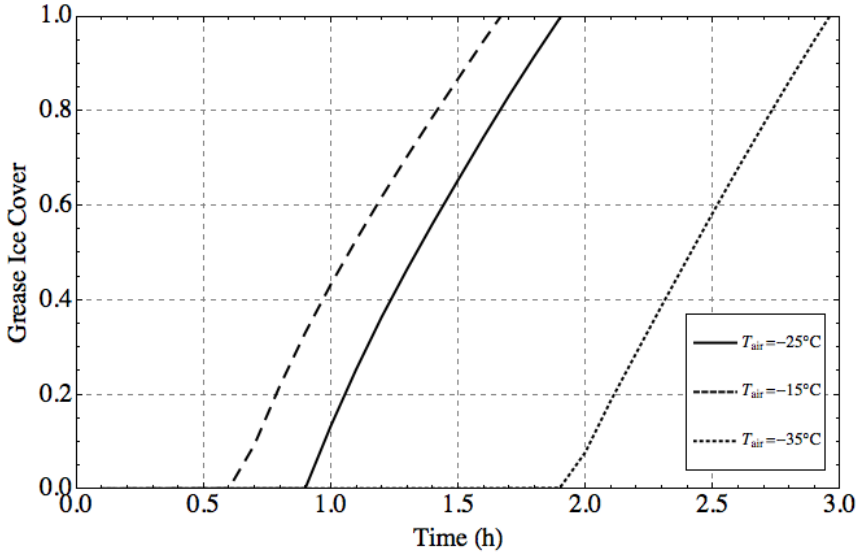

Figure 5.17: Grease ice cover until an ice cover forms

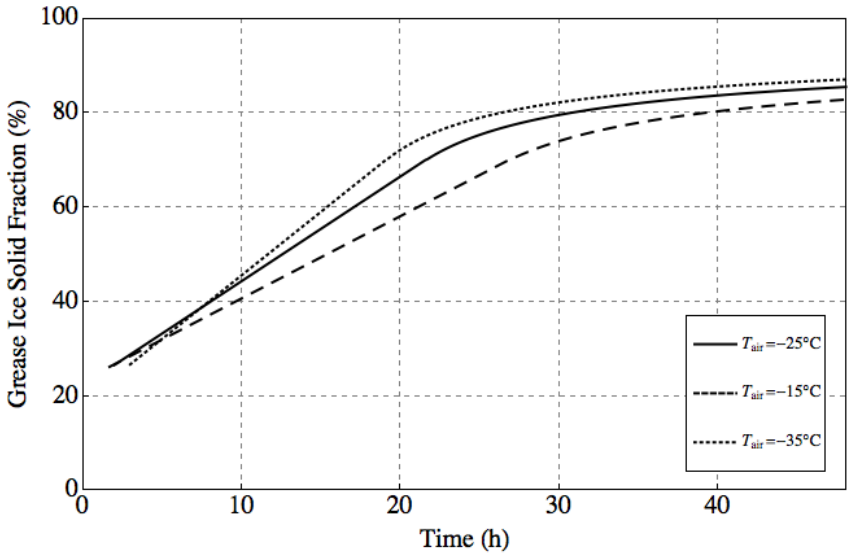

Figure 5.18: Grease ice solid fraction until 2 days of simulation.

Figure 5.18 shows the grease ice solid fraction once an ice cover has formed. Although the lowest temperature case takes the longest to form a complete ice cover, the rate of increase of the grease ice solid fraction is largest so that it reaches a solid fraction of 70% before the other cases (the point at which the ice is classified as congelation ice).

Once the grease ice solid fraction reaches 70%, we define the ice as congelation ice which grows downwards only. Since the lowest air temperature case reaches this state first, as seen in figure 5.18, and since the heat flux at the surface is higher, it has the highest growth rate and inversely for the highest air temperature, as shown in figure 5.19.

Following on from this, figure 5.20 shows the total ice thickness during the same period. Since the lowest air temperature case rate of ice growth is the highest, so is the total thickness.

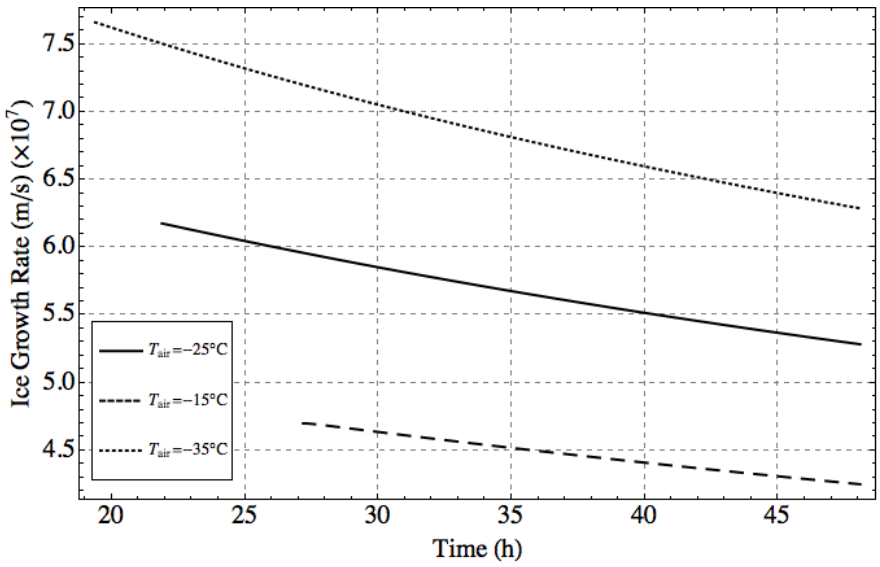

Figure 5.19: Ice growth rate until 2 days of simulation.

We now turn to the desalination of the ice. Figure 5.21 shows the rate of brine release from brine channels. Since the ice is thicker in the lowest temperature scenario, the initial rate of brine release is the highest, and also since the brine channel release starts earlier, the total brine release is always higher in that case, as shown by figure 5.22.

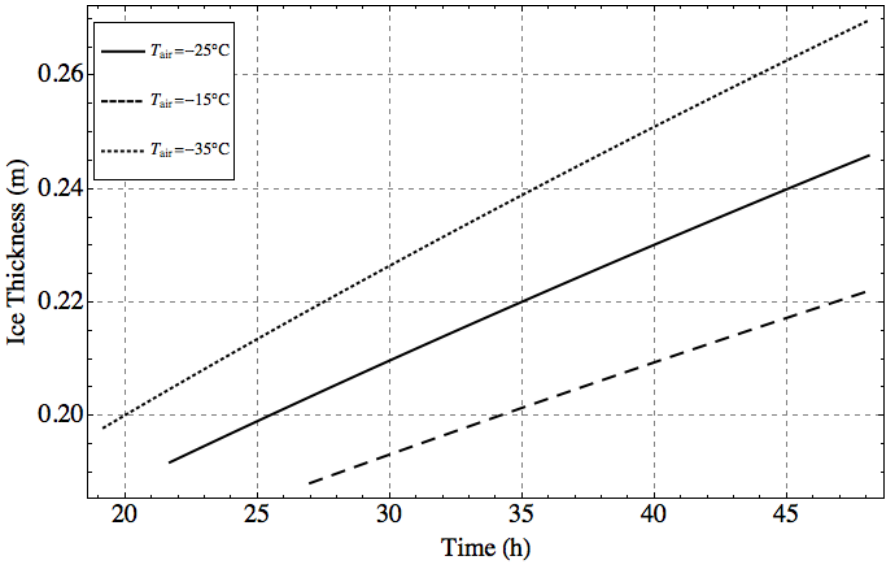

Figure 5.20: Total ice thickness until 2 days of simulation.

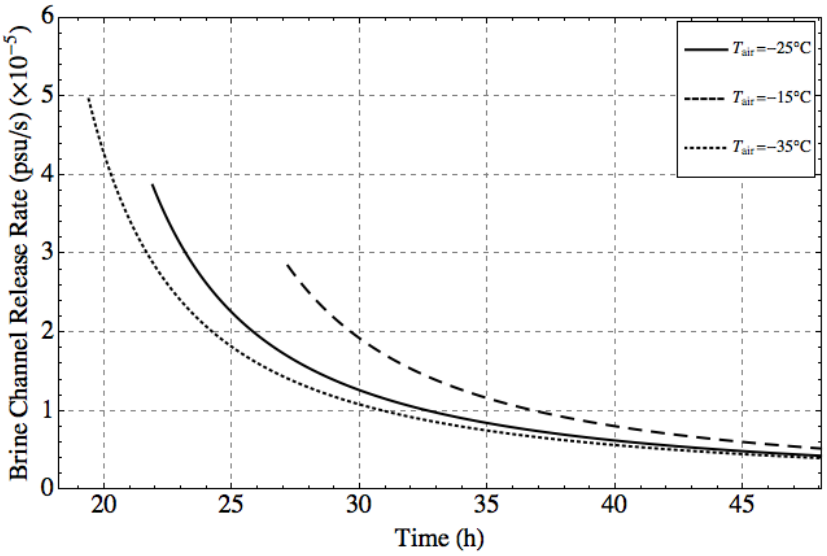

Figure 5.21: Brine channel release rate until 2 days of simulation.

Salt is also released by the ice growing and releasing salt. The rates for this salt release appear to be more linearly dependent on the air temperature, as shown by figure 5.23, and 5.24 which shows the total salt released in this way.

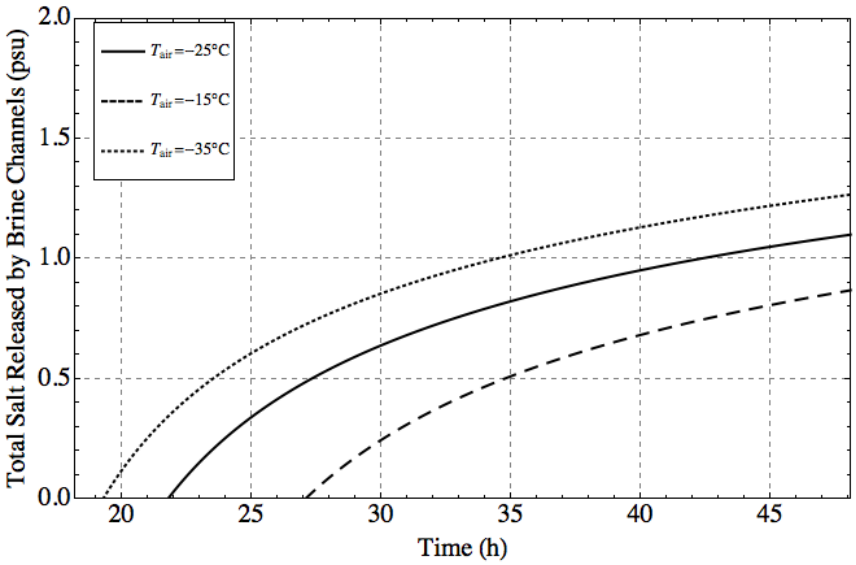

Figure 5.22: Total brine channel release until 2 days of simulation.

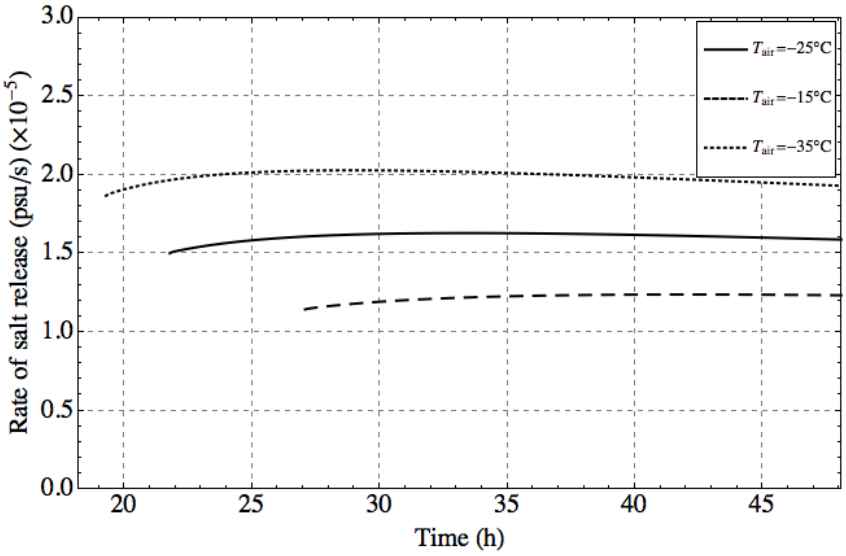

Figure 5.23: Rate of salt release from congelation ice formation until 2 days of simulation.

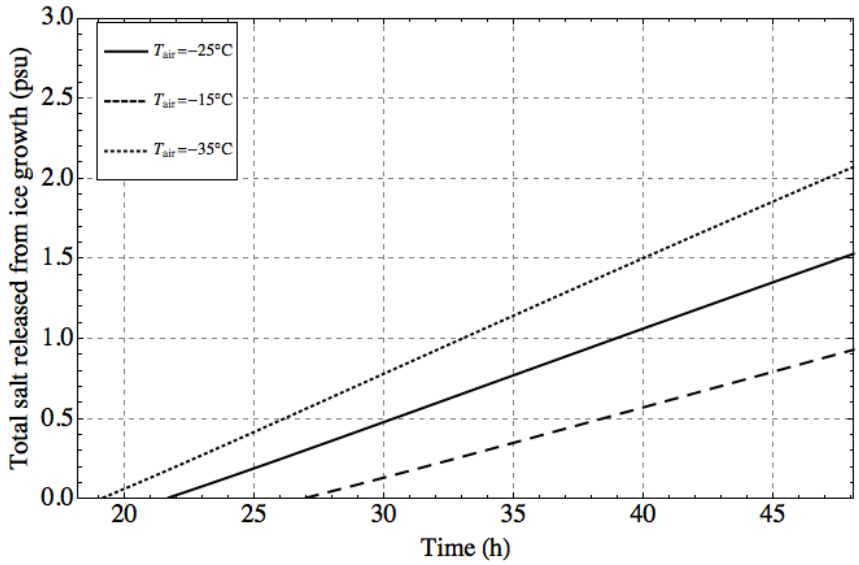

Figure 5.24: Total salt release from congelation ice formation until 2 days of simulation.

5.3 Varying initial water salinity

Since our model starts in a slightly supercooled state, varying the initial salinity also varies the initial water temperature, hence we will not be analyzing the water salinity and temperature profiles, since the three profiles will look so different from the beginning.

The initial water salinity in the reference run was $S_w = 34.5$psu, and we ran two simulations where we increased the salinity to $S_w = 44.5$psu and decreased it to $S_w = 24.5$psu, before comparing the results.

Water salinity affects the freezing temperature and so, all other variables remaining equal, we would expect it to take longer for ice to grow when the salinity is higher as we would need more heat loss. Figure 5.25 shows just that, with the total concentration highest in the lowest salinity and lowest in the highest salinity cases. Although they all take approximately the same time to reach an ice cover, the depth of the ice is different for all three cases.

Figure 5.26 shows the total precipitation out of the water column until an ice cover

forms. As shown in table 7, all three cases reach the solid cover nearly at the same time, with the highest salinity case slightly later. The precipitation rates are about the same for all three cases, showing us that salinity does not significantly affect precipitation. This is because water salinity does not affect the heat loss at the surface, which is the main process contributing to grease ice formation.

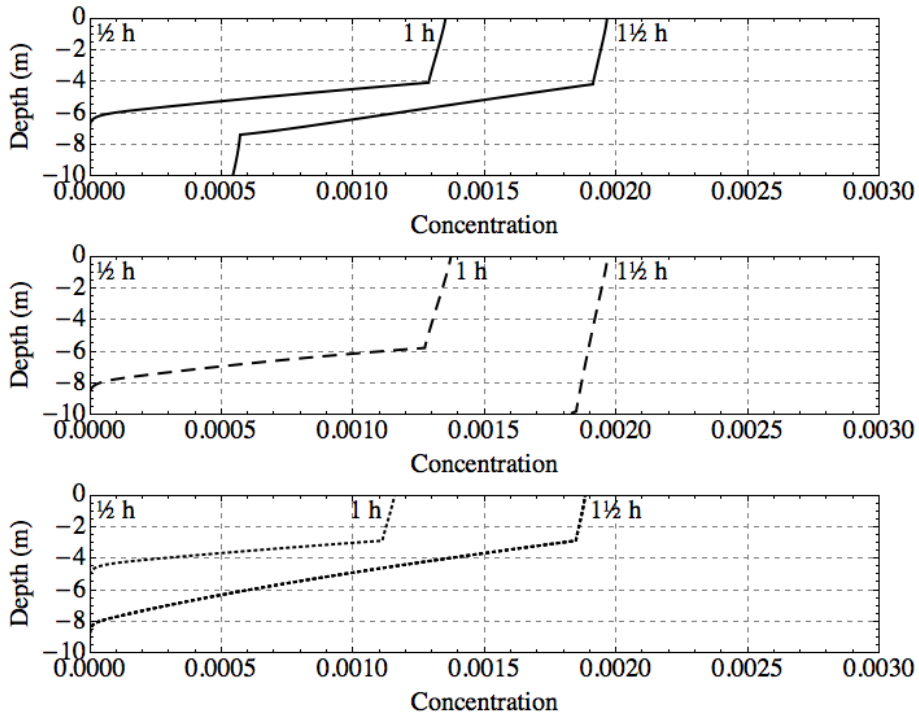

Figure 5.25: Frazil ice concentration plots until an ice cover forms. The top plot is the reference run ($S_w = 34.5$psu), the middle plot is the higher salinity case ("$S_w = 44.5$psu) and the bottom plot is the lower salinity case ($S_w = 24.5$psu).

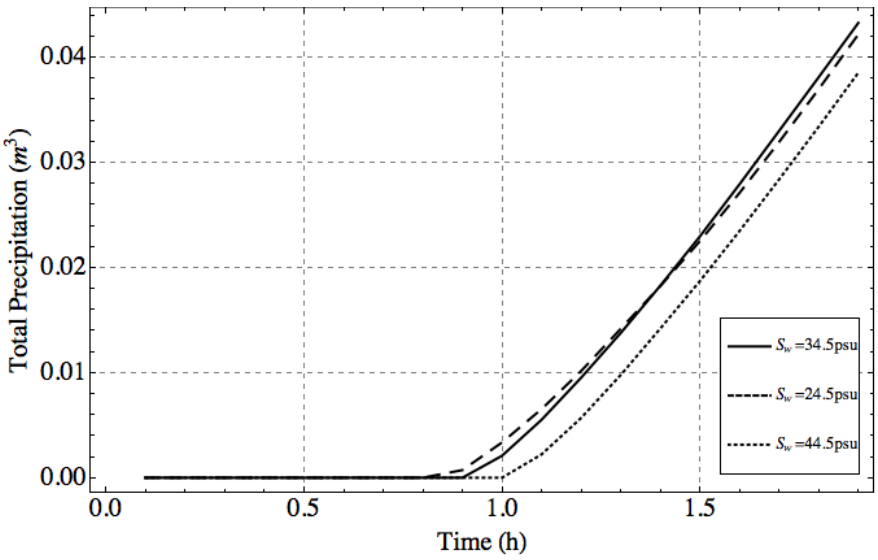

Figure 5.26: Total precipitation out of the water column until an ice cover forms.

Figure 5.27 shows the fraction of the surface covered in grease ice, which again is similar for all three cases, but is slightly later for the higher salinity.

As we can see in figure 5.28, the grease ice solid fraction is approximately the same for all three scenarios. This is again due to the fact that water salinity does not affect the heat loss at the surface.

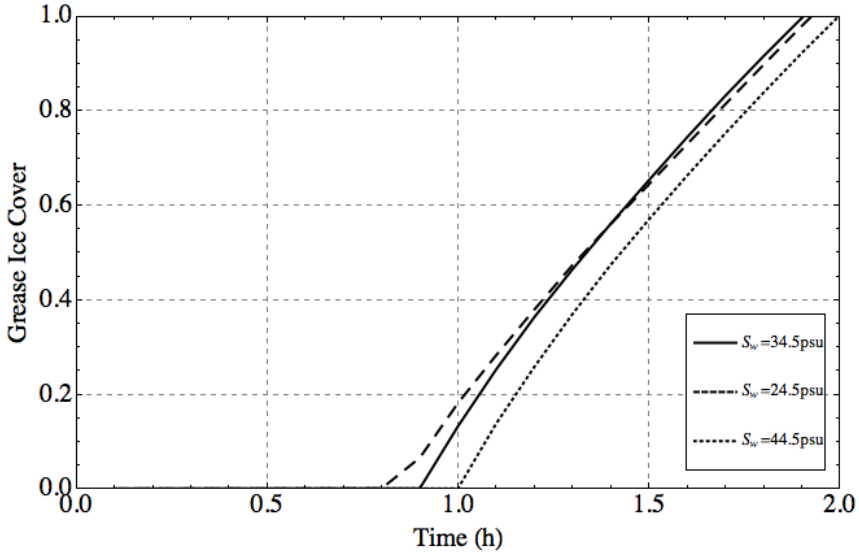

Figure 5.27: Grease ice cover until an ice cover forms.

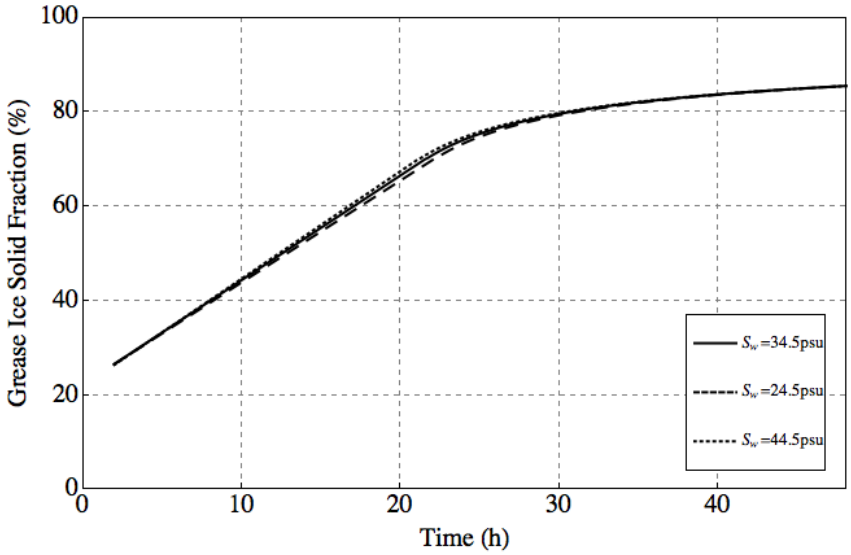

Figure 5.28: Grease ice solid fraction until two days of simulation.

Following on from figure 5.28, where we can see that all three cases reach the required 70% to be considered an ice layer at approximately the same time. We can see in figure 5.29 that although congelation ice growth starts at the same time for all three cases, the lower salinity case is thicker to start but also has a slightly slower growth rate, as we can see in figure 5.30. This is because thicker ice grows at a slower rate since the gradient of temperature is less steep in thicker ice, which leads to slower growth.

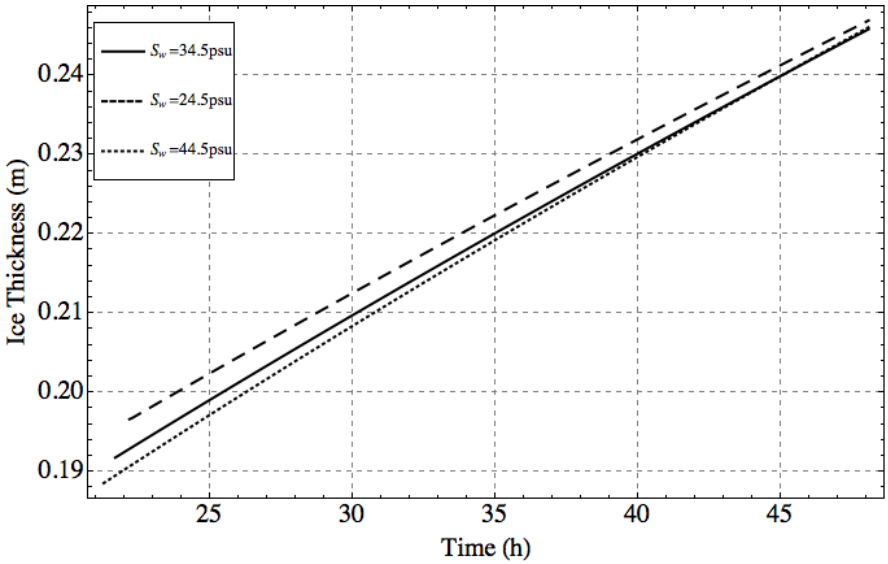

Figure 5.29: Total ice thickness until two days of simulation.

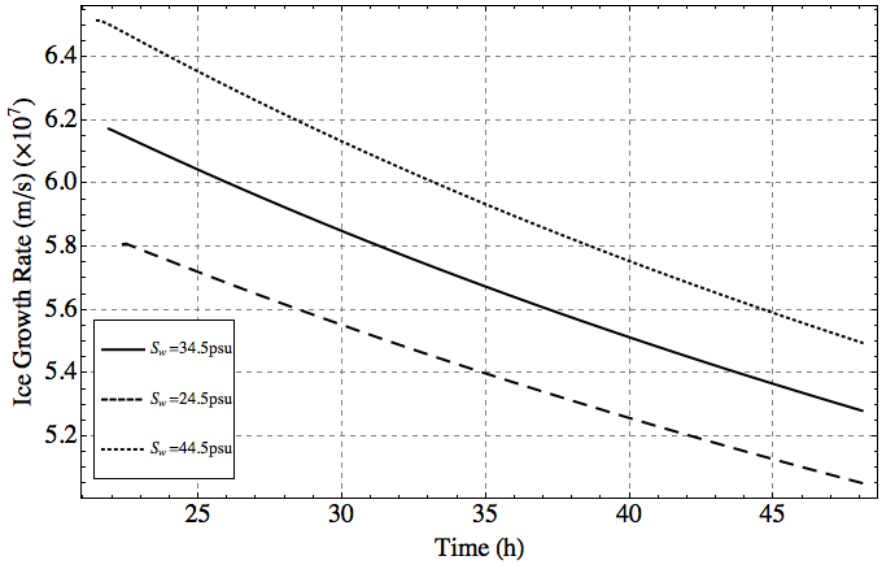

Figure 5.30: Ice growth rate until two days of simulation.

In figure 5.31 we see the rate of brine release from the brine channels. Although they start at different times, they quickly become very close, which can also be seen in figure 5.32.

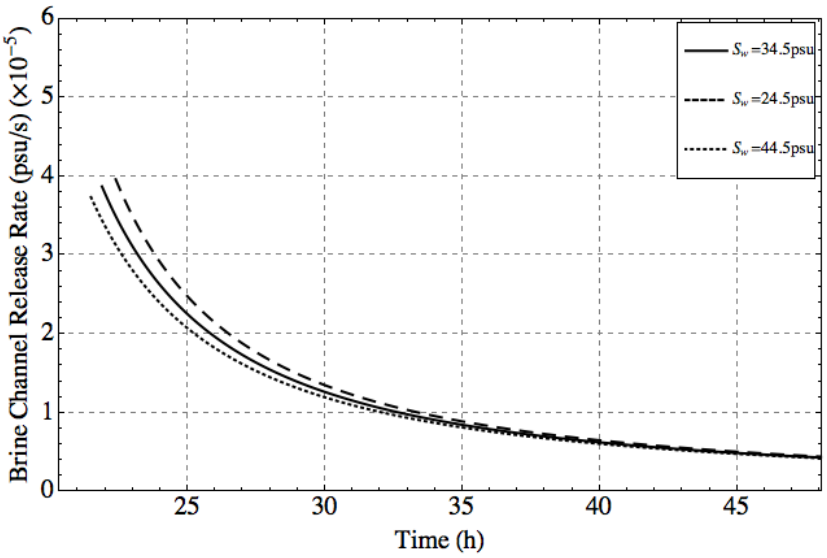

Figure 5.31: Brine channel release rate until two days of simulation.

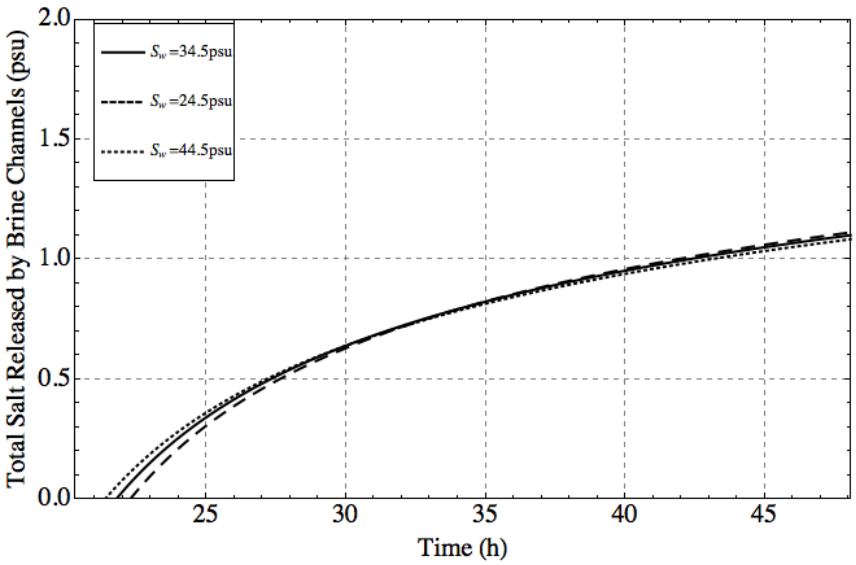

Figure 5.32: Total brine channel release until two days of simulation

Figure 5.33 shows that the differences in the salt release are bigger in the case of salt released by ice formation than by brine channel release.

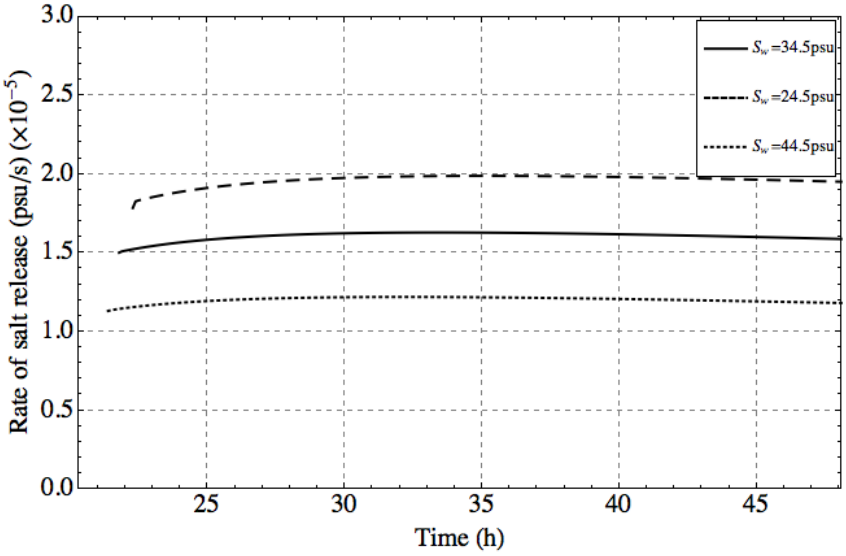

Figure 5.33: Rate of salt release form congelation ice formation until 2 days of simulation.

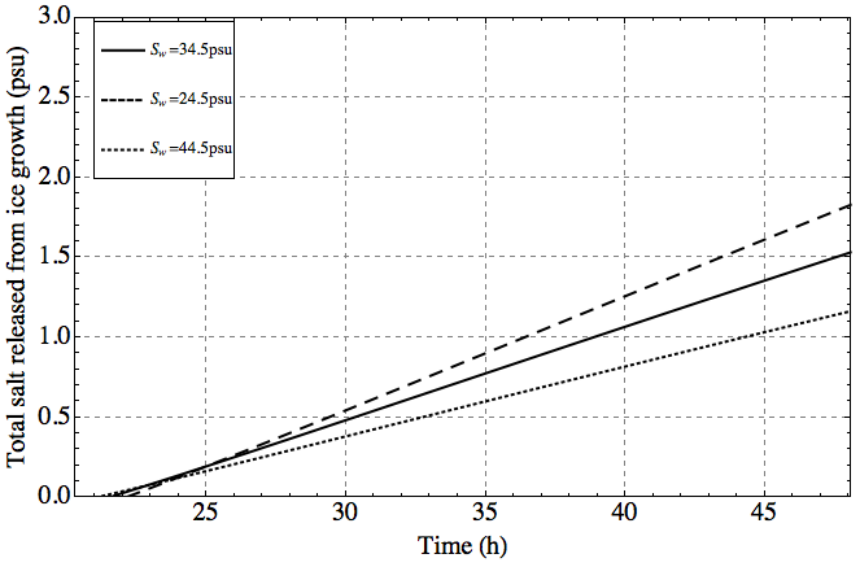

Figure 5.34: Total salt release from congelation ice formation until 2 days of simulation.

5.4 Varying lead width

We now vary the width of the lead which affects the formation of grease ice since the area to cover is altered and the parameterization of the grease ice build-up depends on the lead width. We compare the reference run, which has a lead width of $L_{lead} = 150$m, with two runs with a larger lead width of $L_{lead} = 250$m and a smaller lead width of $L_{lead} = 50$m.

Figure 5.35 shows the frazil ice concentration plots for the three cases, with the reference run first, the smaller length lead second and the larger length lead last. The growth rate of the frazil ice is approximately constant for all three cases, but the time it takes to form an ice layer changes with the lead length. From table 7 we see that the longer the lead, the longer it takes for the ice layer to form.

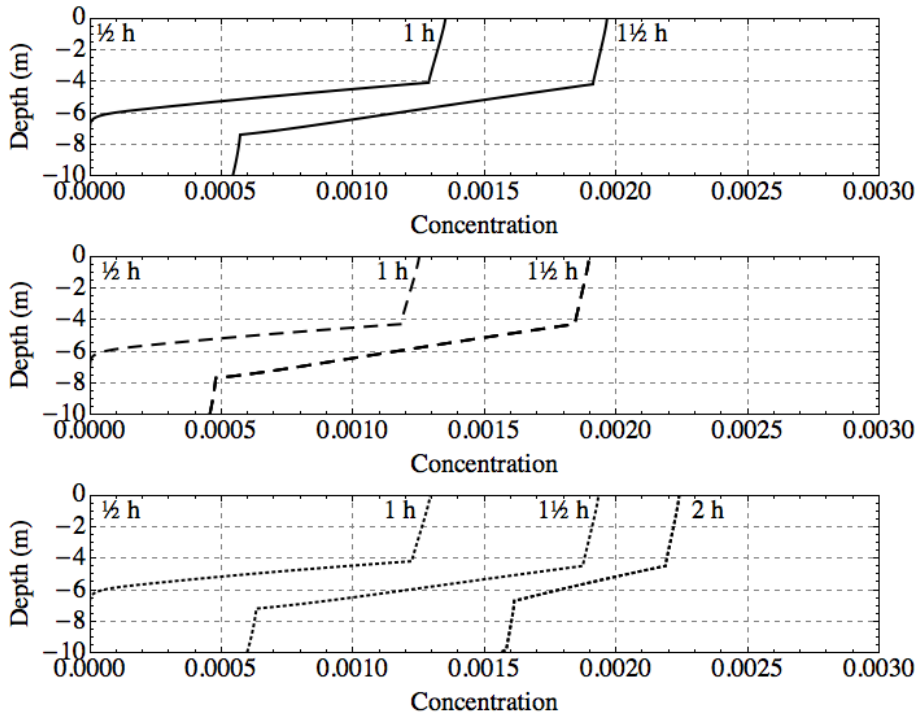

Figure 5.35: Frazil ice concentration plots until an ice cover forms. The top plot is the reference run ($L_{lead} = 150$m), the middle one is the smallest lead width ($L_{lead} = 50$m) and the bottom one is the largest lead width ($L_{lead} = 250$m).

Figures 5.36 and 5.37 show the water temperature and salinity profiles for the three cases, and similarly to the ice concentration, all have similar profiles, except that the longer lead width case takes longer for an ice cover to form.

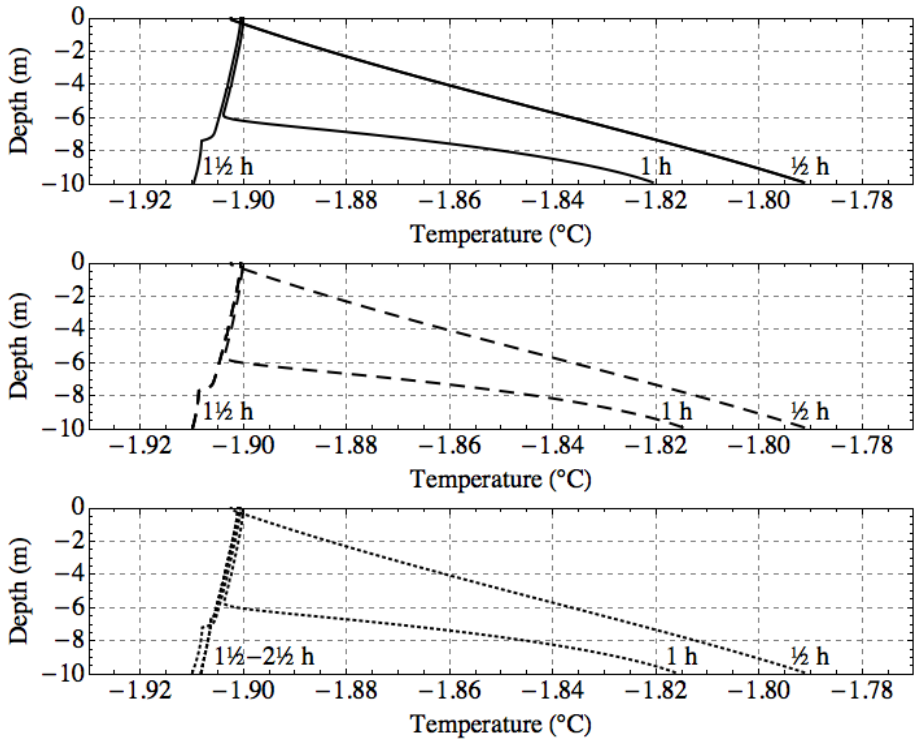

Figure 5.36: Water temperature plots until an ice cover forms. The top plot is the reference run (L_{lead} = 150m), the middle one is the smallest lead width (L_{lead} = 50m) and the bottom one is the largest lead width (L_{lead} = 250m).

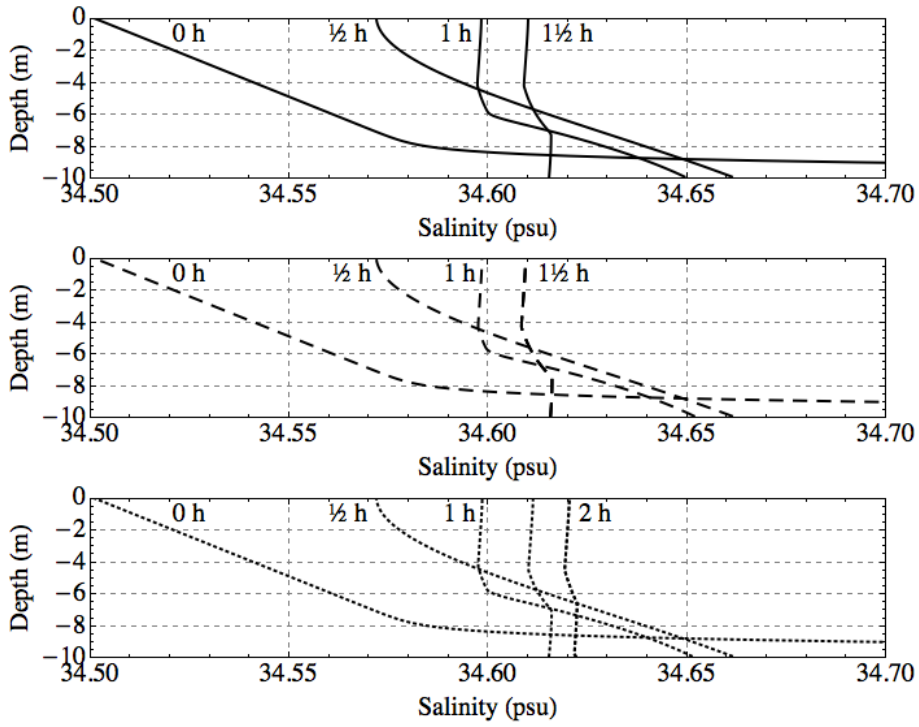

Figure 5.37: Water salinity plots until an ice cover forms. The top plot is the reference run ($L_{lead} = 150$m), the middle one is the smallest lead width ($L_{lead} = 50$m) and the bottom one is the largest lead width ($L_{lead} = 250$m).

Figure 5.38 shows the total precipitation for all three cases. Since the collection depth is dependent on the lead width, the total precipitation needed to form an ice cover varies in all three cases, and is proportionally higher for the biggest lead width and lower for the smallest lead width.

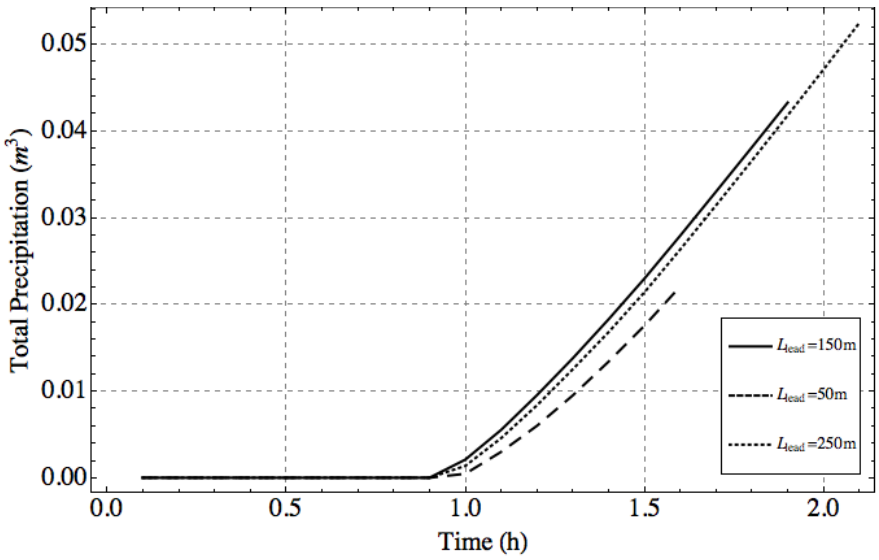

Figure 5.38: Total precipitation out of the water column until an ice cover forms.

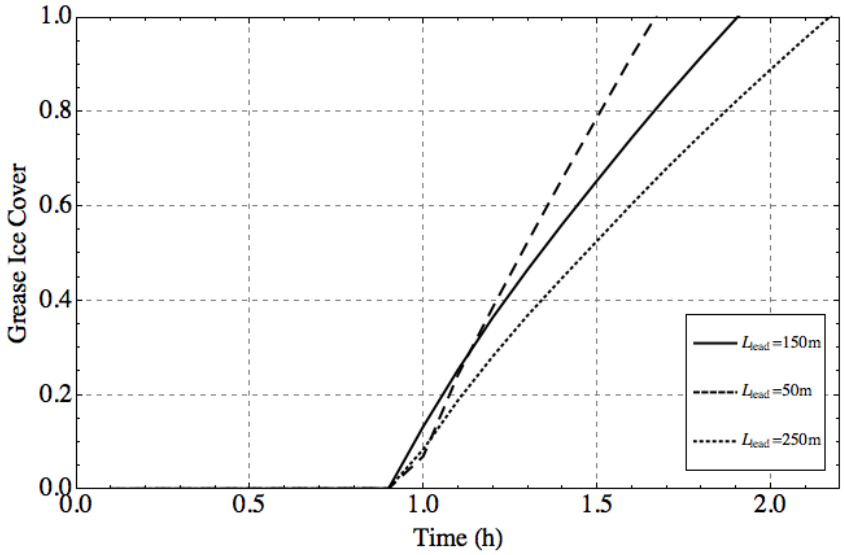

Figure 5.39: Grease ice cover until an ice cover forms.

Figure 5.40 shows the grease ice solid fraction from the time when an ice cover is reached, up to 48 hours. Since the collection depth is different for all three cases, the rate of growth of the grease ice fraction is also different for all three cases. This is due to the thicker ice solid fraction growing slower, hence the smallest lead width case solid fraction growing fastest, and the biggest lead width case solid fraction growing slowest. This can also be seen in figure 5.39, where the smallest lead width case reaches a full grease ice cover

faster.

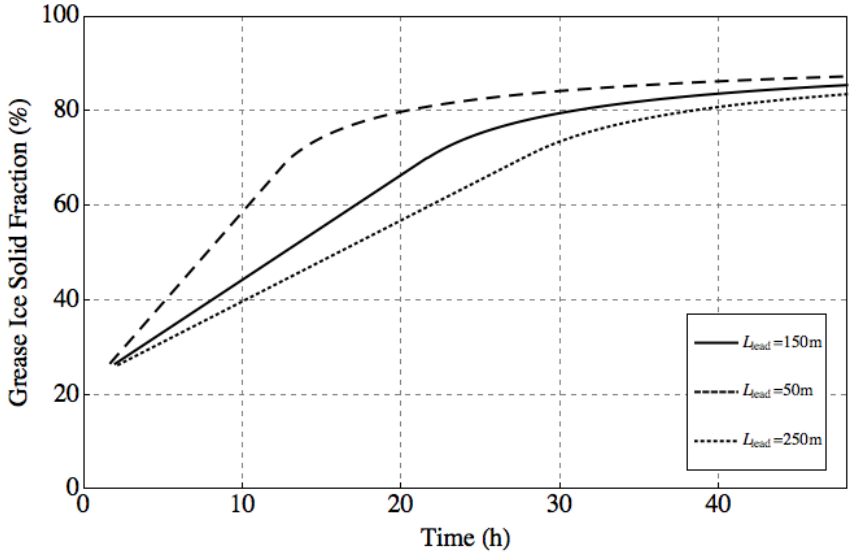

Figure 5.40: Grease ice solid fraction until two days of simulation.

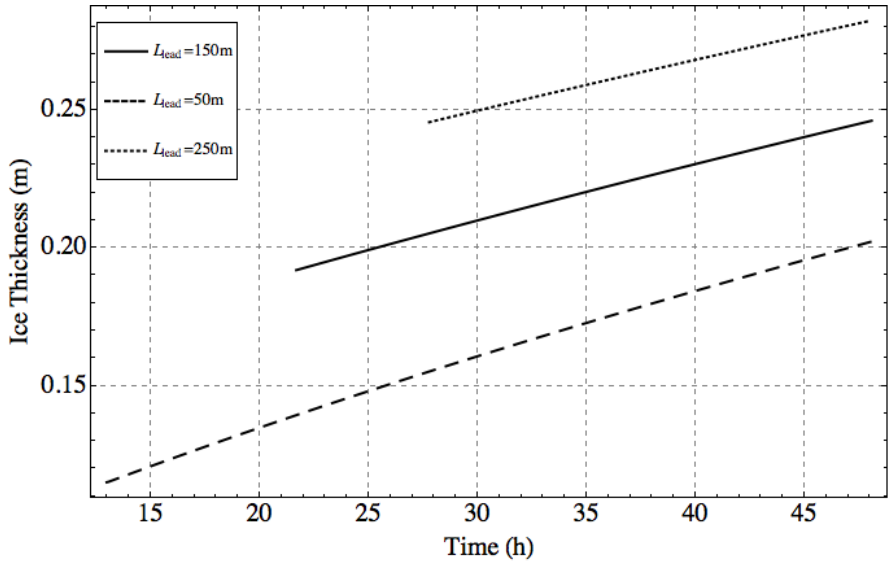

Figure 5.41: Total ice thickness until two days of simulation.

Figure 5.41 shows the thickness of the ice cover up to 48 hours of run-time. Following on from figure 5.40, the smallest lead width case reaches the required 70% grease ice solid fraction first and the largest lead width reaches it last. As mentioned earlier, the thicker the ice is the slower the growth rate is, which can be seen in figure 5.42. We can infer from figure 5.41 that ice growth rates are a lot higher during the frazil ice formation stage than

the congelation ice formation stage, since after 48 hours the ice is thicker in the largest lead width case, solely because it spends longer in the frazil ice formation stage.

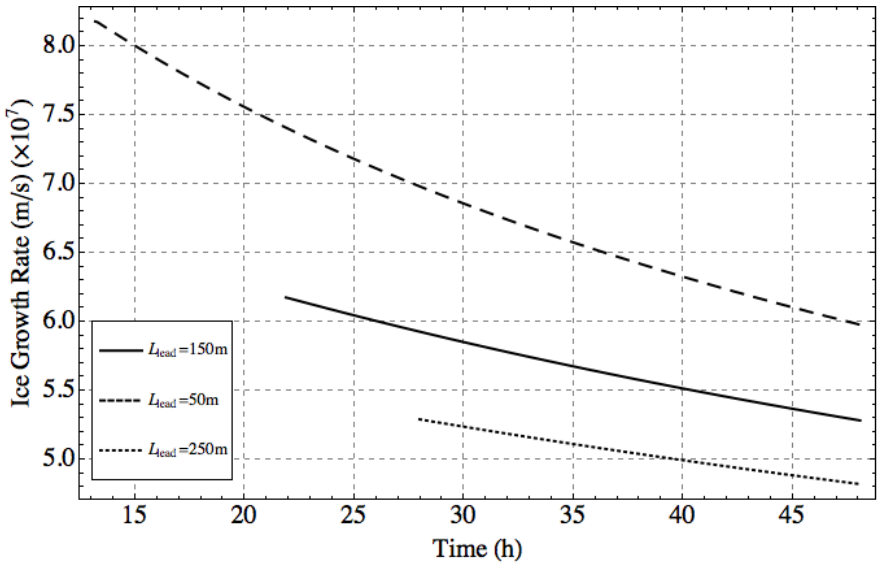

Figure 5.42: Ice growth rate until two days of simulation.

Once the ice grows to a certain thickness, brine channels form and release brine to the water below. Since the ice is thickest in the largest lead width case, we might expect the brine channels to form here first, but because of the lower salinity in the lower salinity case the threshold for brine channel formation is lower and so they form in this case first, as shown in figure 5.43. The other two cases follow on, with brine tube drainage in the largest lead width case starting last, but the later they start, the higher the rate is. This happens because the ice is thicker, which leads to larger brine channels, and hence a higher brine release rate. In figure 5.44 we see the total brine release from the ice. We can see that although the smallest lead width start first, the total salt released is quickly larger in the other two cases, since the brine release rate is larger.

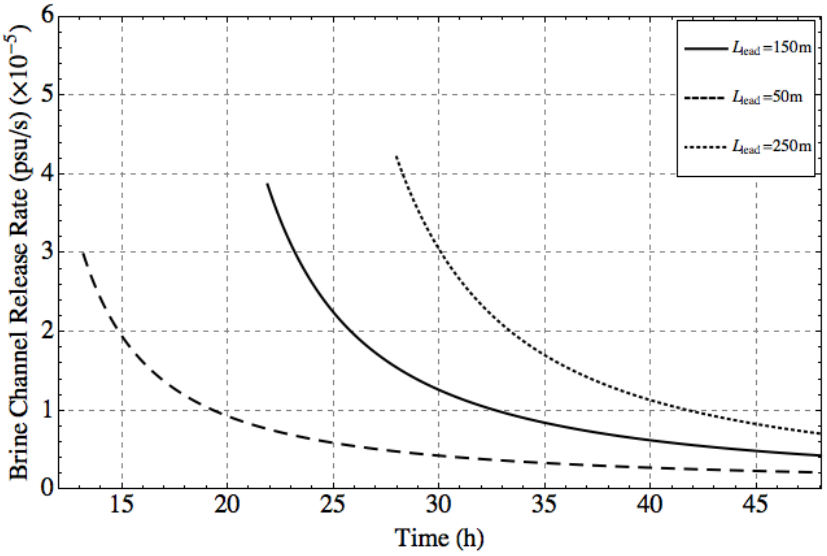

Figure 5.43: Brine channel release rate until two days of simulation.

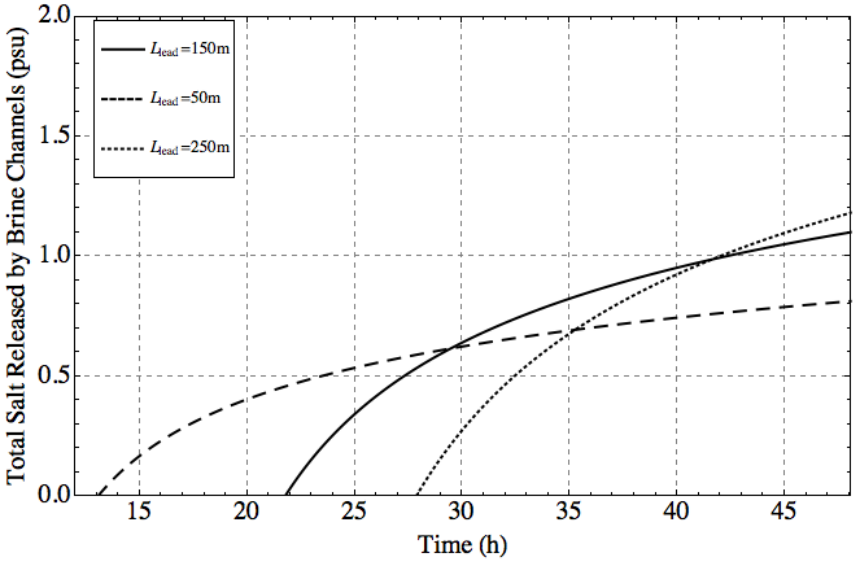

Figure 5.44: Total brine channel release until two days of simulation.

The rate of salt release at the interface solely by brine expulsion is directly proportional to the ice growth rate, and so is larger in the smallest lead width case, and smaller in the largest width case, as can be seen in figure 5.45. Since the smallest lead width case starts first and has the highest rate, the total salt release from congelation growth is largest in this case, as shown in figure 5.46.

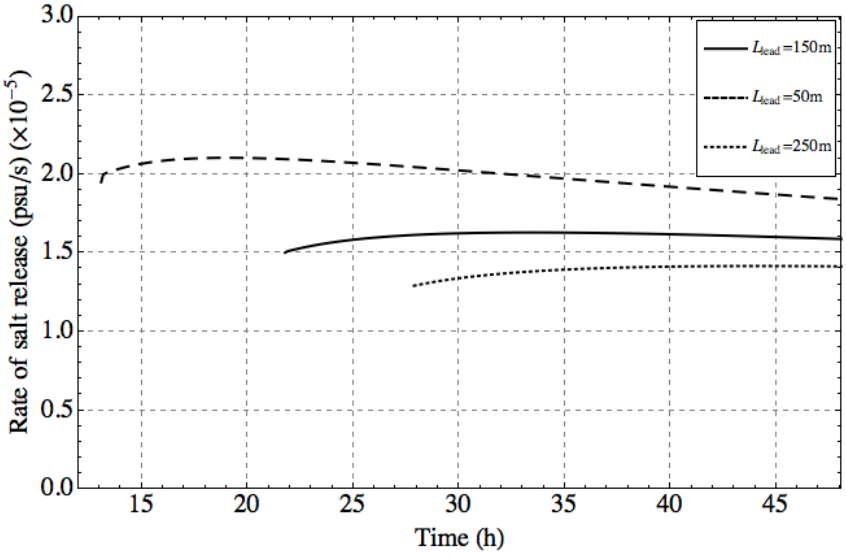

Figure 5.45: Rate of salt release from congelation ice until two days of simulation.

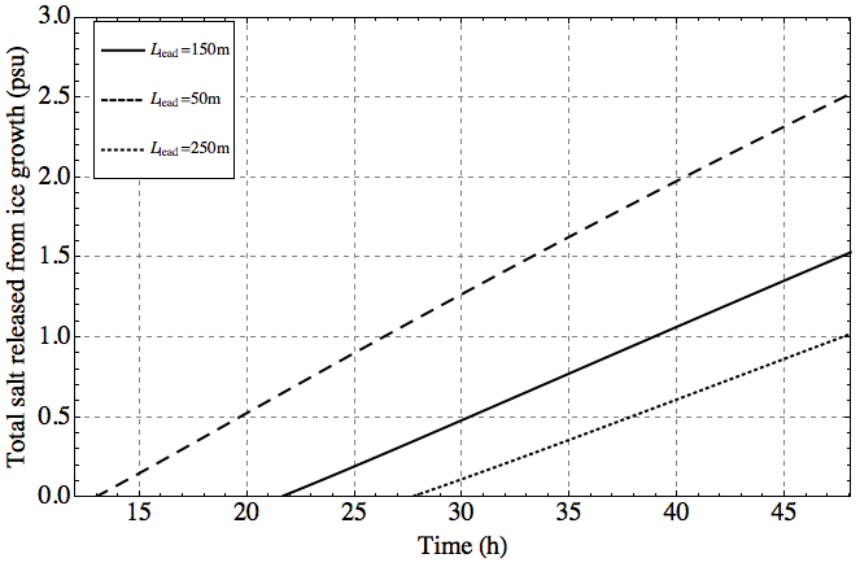

Figure 5.46: Total salt release from congelation ice formation until two days of simulation.

5.5 Varying longwave radiation

Varying longwave radiation affects the heat balance at the ocean-atmosphere interface. This affects the amount of heat loss from the ocean and hence the growth/melting rate of the ice. The results in this section should therefore be comparable to the results in the air temperature sensitivity study.

Once again, we compared the reference run, with a longwave radiation of $F_{LW} = 170$ W/m^2, with two cases with a higher longwave radiation of $F_{LW} = 240$ W/m^2), and a lower longwave radiation of $F_{LW} = 100$ W/m^2. In figure 5.47 we see the concentration profiles for the three scenarios until they form ice layers. The lowest radiation case takes longer to start forming ice, since lower radiation means that there is greater net heat loss, which in turn delays the formation of frazil ice. This is probably due to the secondary nucleation and is similar to the air temperature study. The reference case and the higher radiation case are a lot more similar, which suggests that the delay in ice formation is not directly related to the longwave radiation.

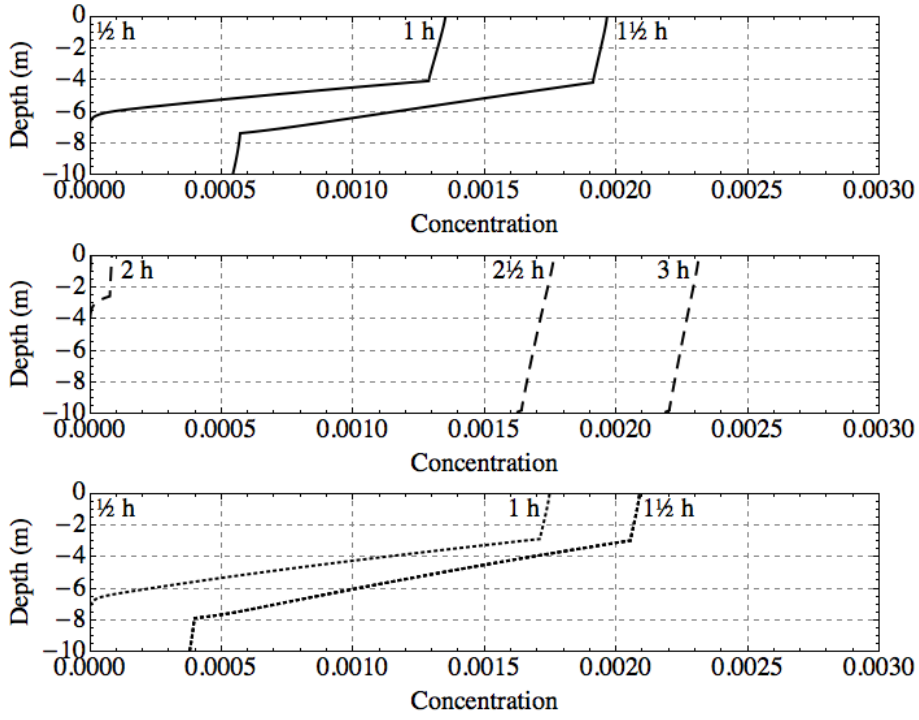

Figure 5.47: Frazil ice concentration plots until an ice cover forms. The top plot is the reference run ($F_{LW} = 170$ W/m^2), the middle plot is the lower longwave radiation ($F_{LW} = 100$ W/m^2) and the bottom plot is the higher longwave radiation ($F_{LW} = 240$ W/m^2).

Figure 5.48 shows the temperature profiles for the three scenarios. The temperature takes longer to decrease in the lower radiation plot since, although the net heat loss is greater, more ice is created in this case which keeps the temperature from decreasing. Another thing to note is the depth to which mixing occurs in all three cases. In the reference

run the mixing happens until about 4 m, in the second plot it happens throughout the whole 10 m, and in the bottom plot it happens in the top 3 m. This happens because the delay in the initial formation of ice in the lowest radiation allows the layer to become more mixed, and so when ice starts forming it mixes further down. Conversely for the higher radiation case.

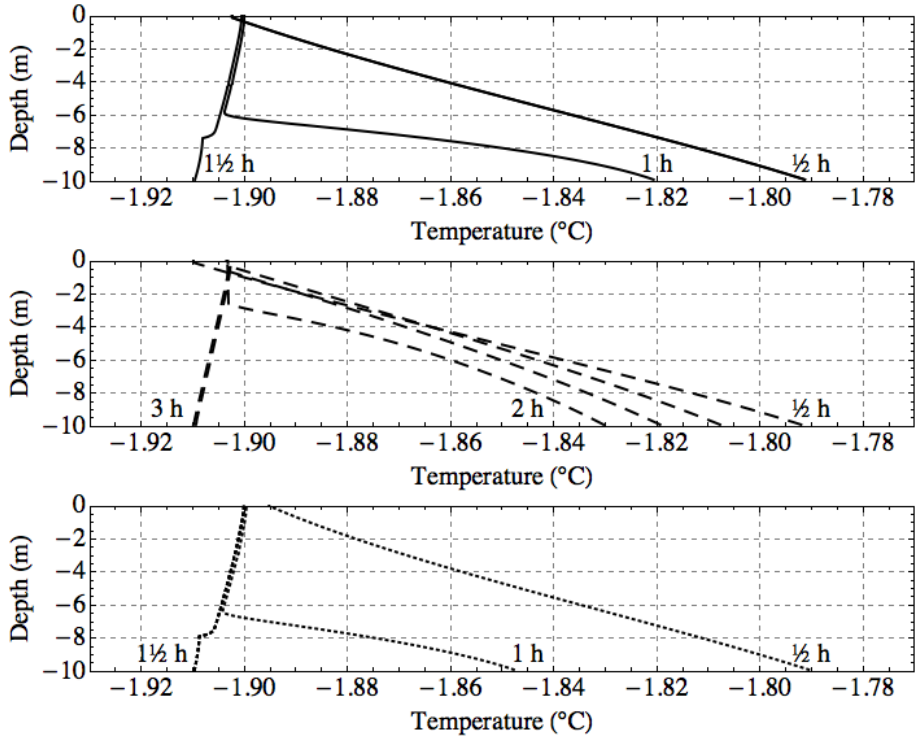

Figure 5.48: Water temperature plots until an ice cover forms. The top plot is the reference run (F_{LW} = 170 W/m^2), the middle plot is the lower longwave radiation (F_{LW} = 100 W/m^2) and the bottom plot is the higher longwave radiation (F_{LW} = 240 W/m^2).

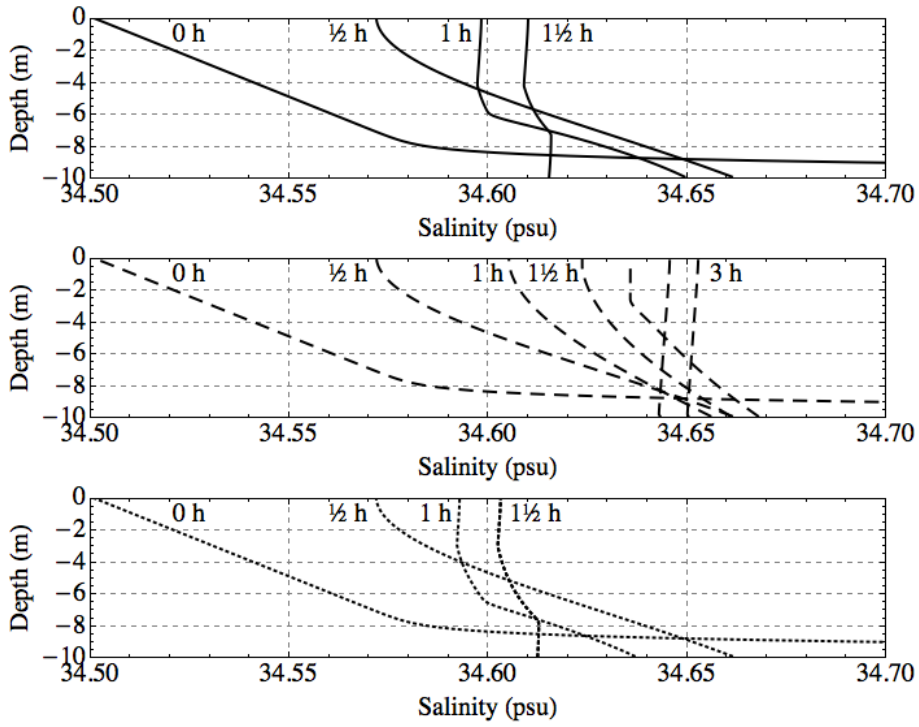

Figure 5.49: Water salinity plots until an ice cover forms. The top plot is the reference run ($F_{LW} = 170$ W/m^2), the middle plot is the lower longwave radiation ($F_{LW} = 100$ W/m^2) and the bottom plot is the higher longwave radiation ($F_{LW} = 240$ W/m^2).

The salinity profiles are similar to the temperature profiles, with the water being mixed to much deeper in the lower radiation case, as shown in plot 2 of figure 5.49. The reference plot and the bottom plot are much more similar.

The precipitation plots are shown in figure 5.50, where we can clearly see the delay in the initial formation of frazil ice, with the lower radiation case starting more than an hour later than the other two cases. The higher radiation case also starts slightly before the reference case. The rates of precipitation are about the same for all three cases.

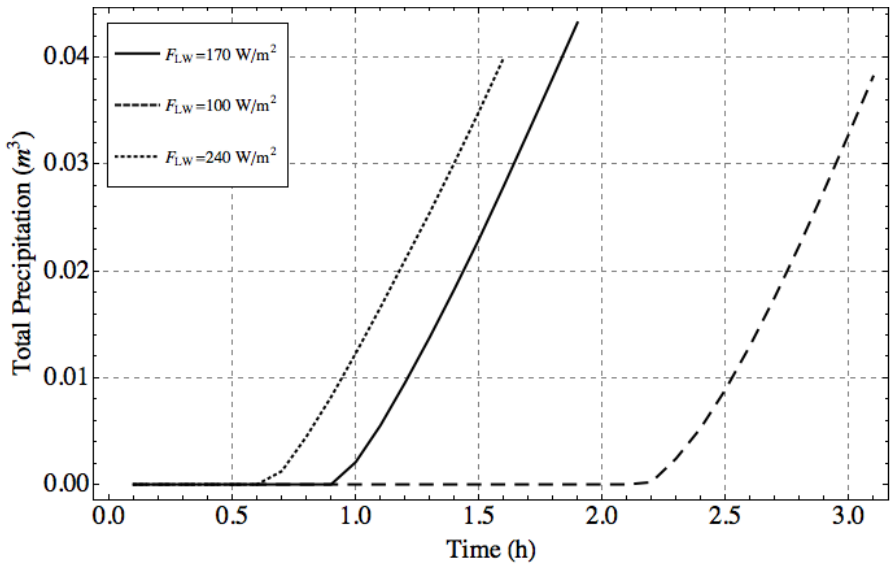

Figure 5.50: Total precipitation out of the water column until an ice cover forms.

Although the lowest radiation case forms an ice layer later than the other two cases the heat loss at the surface is higher, hence the grease ice growth rate is higher and so it reaches the 70% threshold first, as seen in figure 5.52. Conversely, the highest radiation case reaches it last. The grease ice cover plots in figure 5.51 show that the lower the radiation, the longer it takes for the grease ice cover to begin forming. This is counter intuitive and probably due to the secondary nucleation delay we have mentioned before.

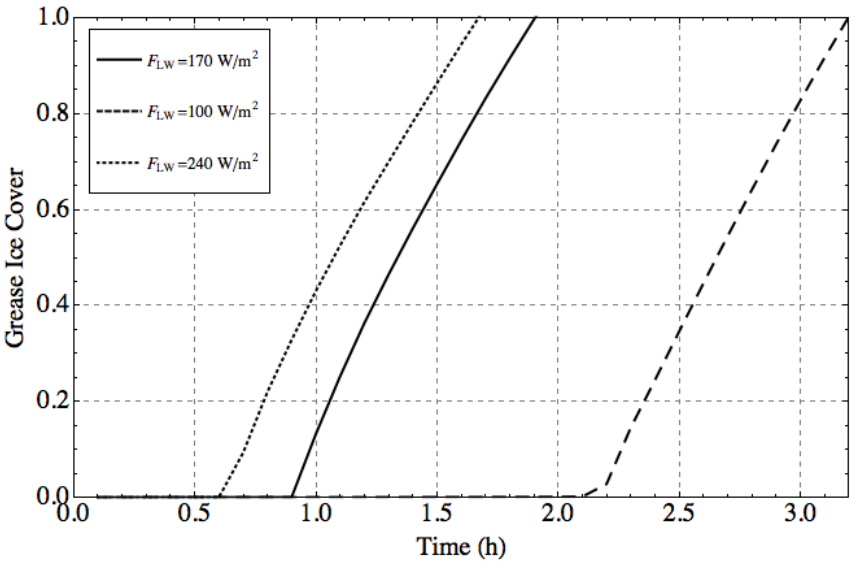

Figure 5.51: Grease ice cover until an ice cover forms.

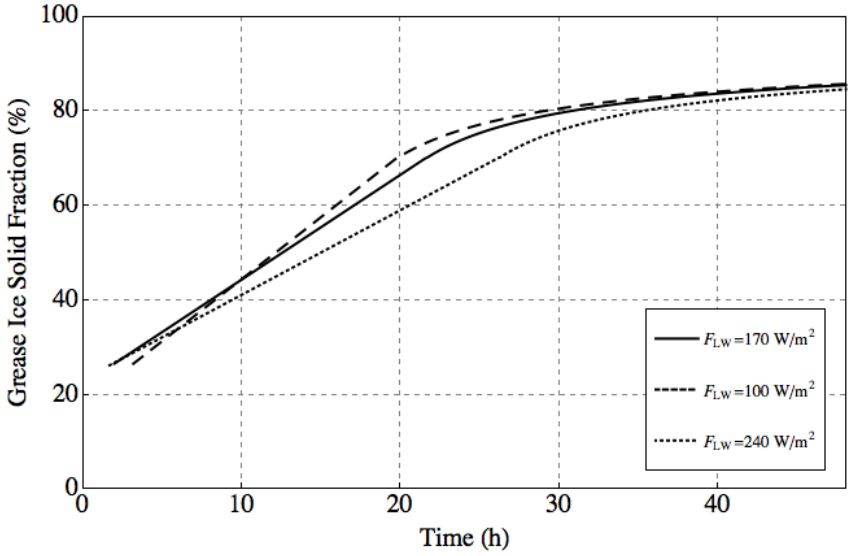

Figure 5.52: Grease ice solid fraction until two days of simulation.

Figure 5.53 shows the ice thickness plots for all three cases up to 48 hours of simulation. As seen earlier, the lowest radiation case reaches the consolidated ice cover stage first and the highest radiation case reaches it last. We would expect the growth rate for the lowest radiation case to be the highest, but since the ice is slightly thicker to start with, the growth rate is actually the lowest, as shown in figure 5.54. Conversely, the highest radiation case would normally have the lowest growth rate, but has the highest, since the ice is thinner. After two days of simulation, the ice is thickest in the lowest radiation case, as we would expect, since the heat loss at the surface is higher.

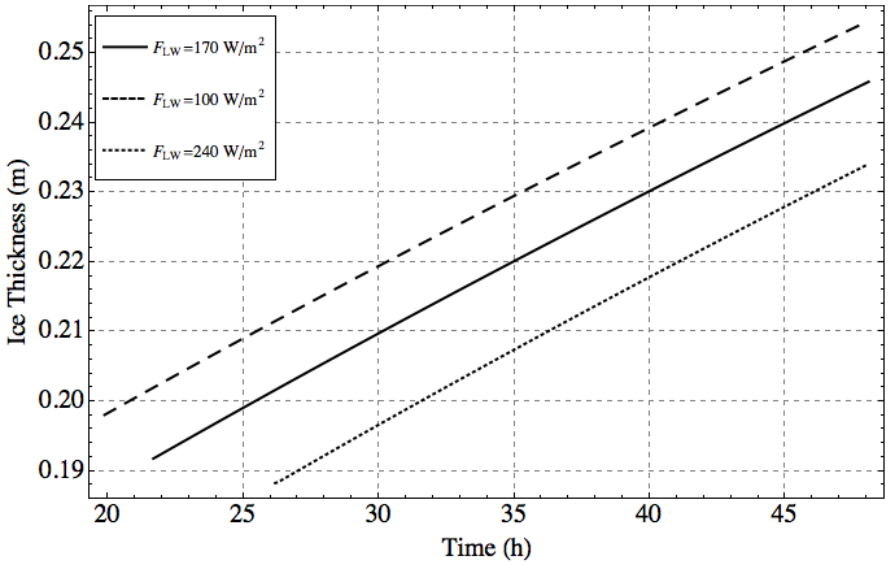

Figure 5.53: Total ice thickness until two days of simulation.

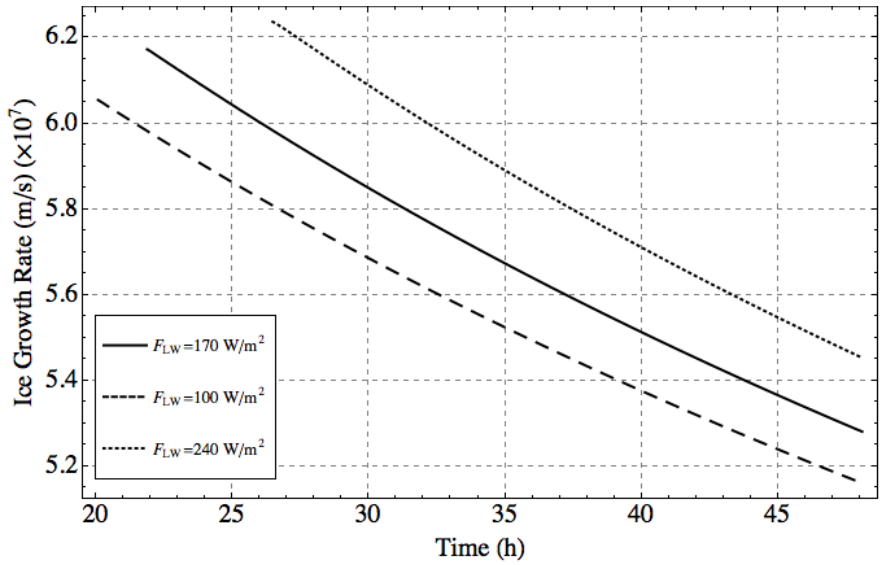

Figure 5.54: Ice growth rate until two days of simulation.

The rate of desalination of the ice through brine channels is shown in figure 5.55, where we can see that since the lowest radiation case has the thicker ice, the brine channels form earlier in this case. The highest radiation case is the last to start. We note that although they all start at different times, at the end of 48 hours, the rates are approximately equal. Similarly, in figure 5.56 we see that with time, the total brine released becomes closer for all three cases.

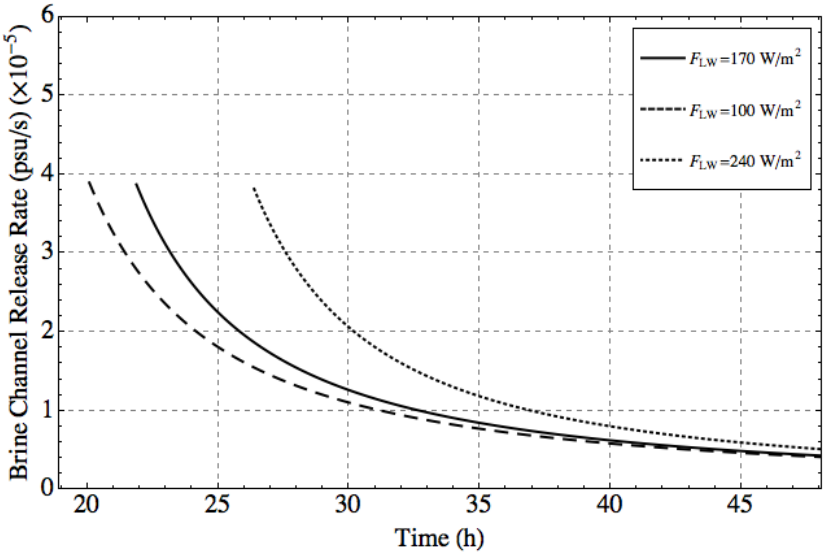

Figure 5.55: Brine channel release rate until two days of simulation.

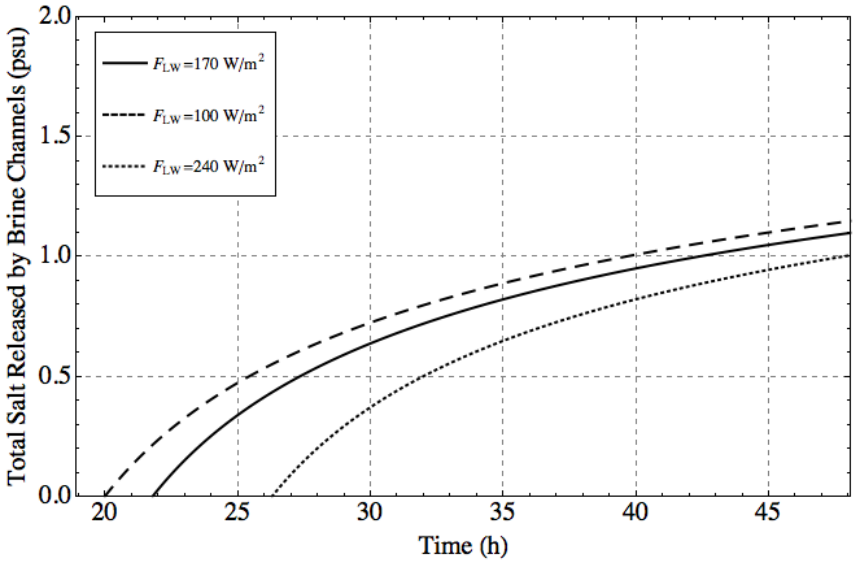

Figure 5.56: Total brine channel release until two days of simulation.

With regards to the salt released during the formation of congelation ice, we see in figure 5.57 that the rate of salt release is approximately constant for all 3 cases, with a slight downturn later on, as the ice becomes thicker and the growth rate slows. Although the rates are constant, since the lower radiation case starts first, the total salt released is always higher in this case, as seen in figure 5.58

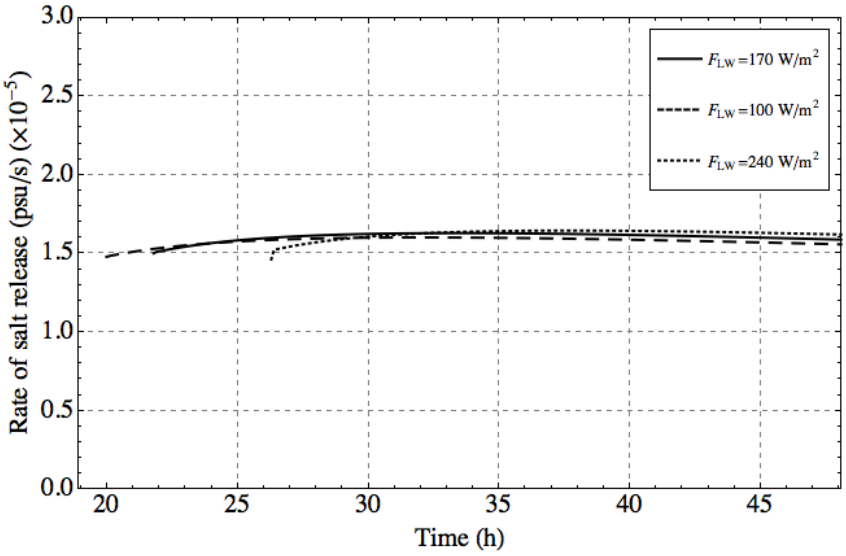

Figure 5.57: Rate of salt release from congelation ice until two days of simulation.

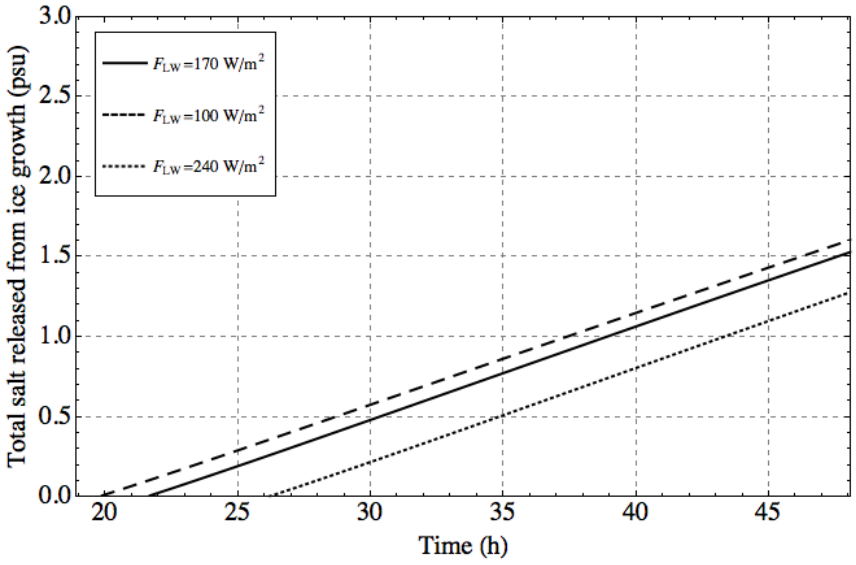

Figure 5.58: Total salt release from congelation ice formation until two days of simulation.

5.6 Varying air humidity

Varying air humidity affects the heat balance at the surface of the water. A higher humidity gives a lower latent heat loss and so decreases the rate of frazil and congelation ice growth, similarly to the air temperature and longwave radiation flux sensitivity studies. We compare the reference run, which has air humidity of $q_a = 5 \times 10^{-4}$, with two cases

with a higher air humidity of $q_a = 2.5 \times 10^{-3}$ and a lower humidity of $q_a = 1 \times 10^{-4}$.

Figure 5.59 shows the concentration plots until an ice cover forms. The concentration after an hour is highest in the higher humidity case, and lowest in the lowest in the lower humidity case. This is contrary to what we expect, since lower humidity leads to a larger heat loss. We relate this back to the delay we encountered during this study, where ice only starts forming after a period of time which seems to be directly related to the secondary nucleation parameterization. As can be seen in table 7, the higher humidity case forms an ice layer at T_1 first, implying that the delay in this case is not as large as in the reference and lower humidity cases.

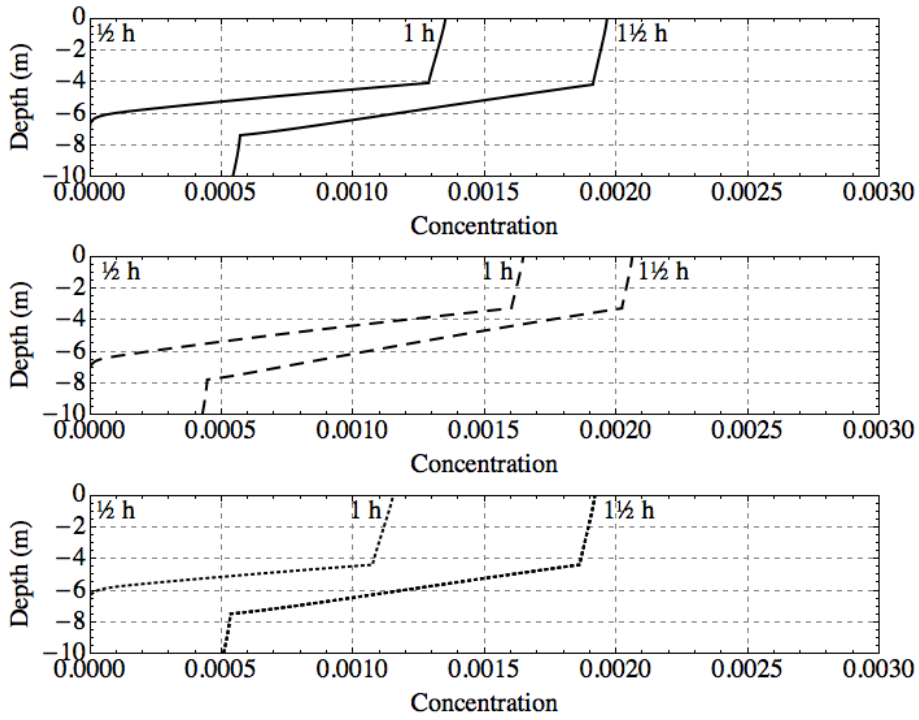

Figure 5.59: Frazil ice concentration plots until an ice cover forms. The top plot is the reference run ($q_a = 5 \times 10^4$), the middle plot is the higher humidity ($q_a = 2.5 \times 10^{-3}$) and the bottom plot is the lower humidity ($q_a = 1 \times 10^{-4}$).

The water temperature profiles are shown in figure 5.60, where after 1 hour, the temperature is lower in the higher humidity case, since less ice has formed to quench the supercooling. The salinity profiles, in figure 5.61 are all approximately the same, except

the salinity is lower in the middle plot for the same reason as mentioned above.

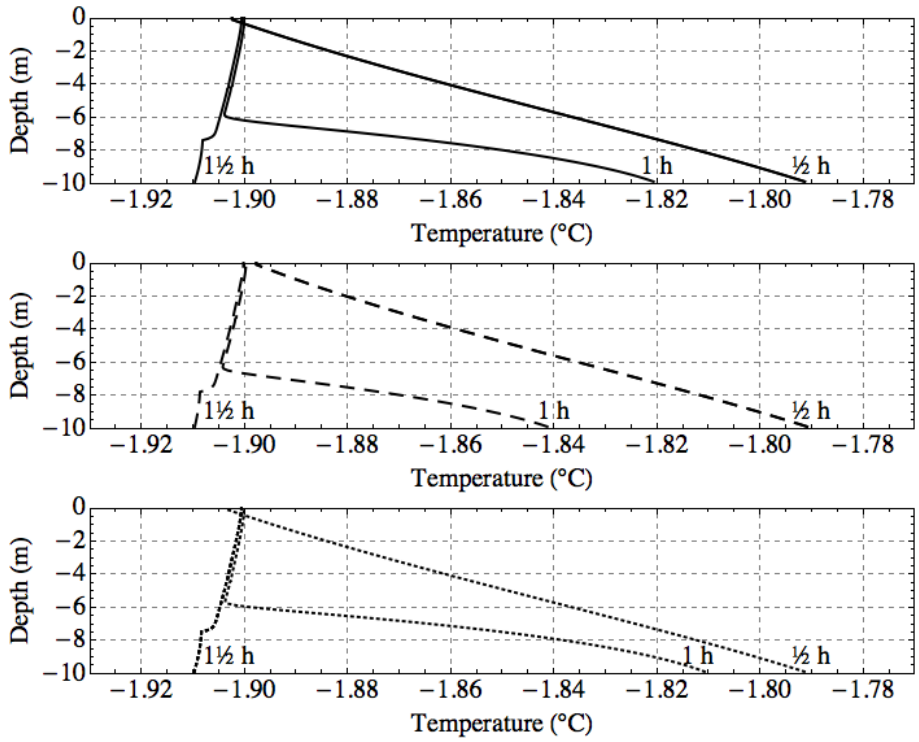

Figure 5.60: Water temperature plots until an ice cover forms. The top plot is the reference run ($q_a = 5 \times 10^4$), the middle plot is the higher humidity ($q_a = 2.5 \times 10^{-3}$) and the bottom plot is the lower humidity ($q_a = 1 \times 10^{-4}$).

The total frazil ice precipitation plot is shown in figure 5.62. The precipitation starts first in the higher humidity case, because since frazil ice starts forming earlier, it also precipitates earlier. The precipitation rates are about the same with all three cases forming an ice layer before two hours.

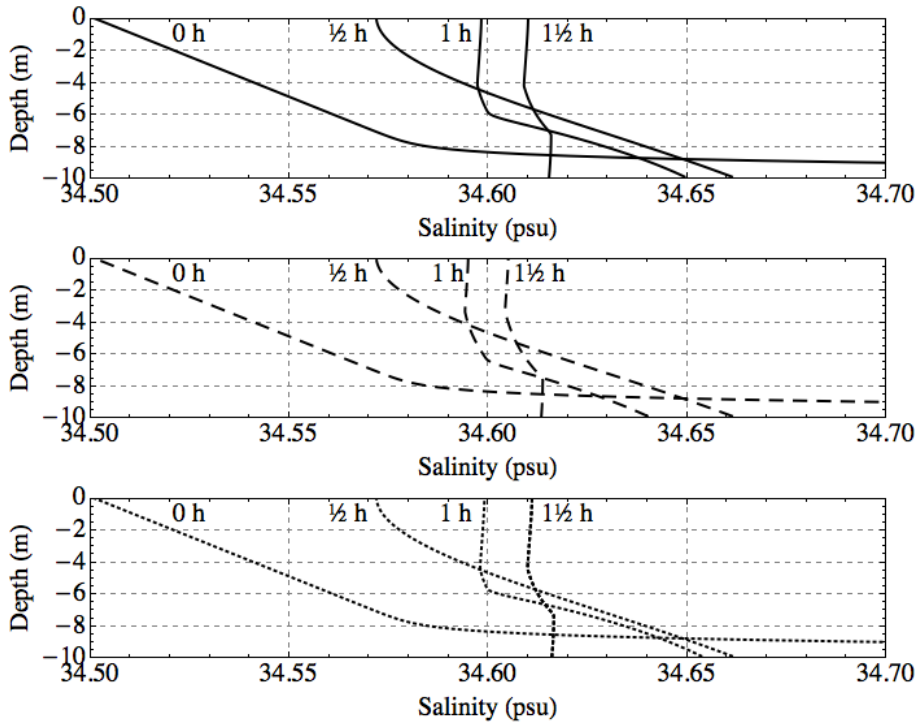

Figure 5.61: Water salinity plots until an ice cover forms. The top plot is the reference run ($q_a = 5 \times 10^4$), the middle plot is the higher humidity ($q_a = 2.5 \times 10^{-3}$) and the bottom plot is the lower humidity ($q_a = 1 \times 10^{-4}$).

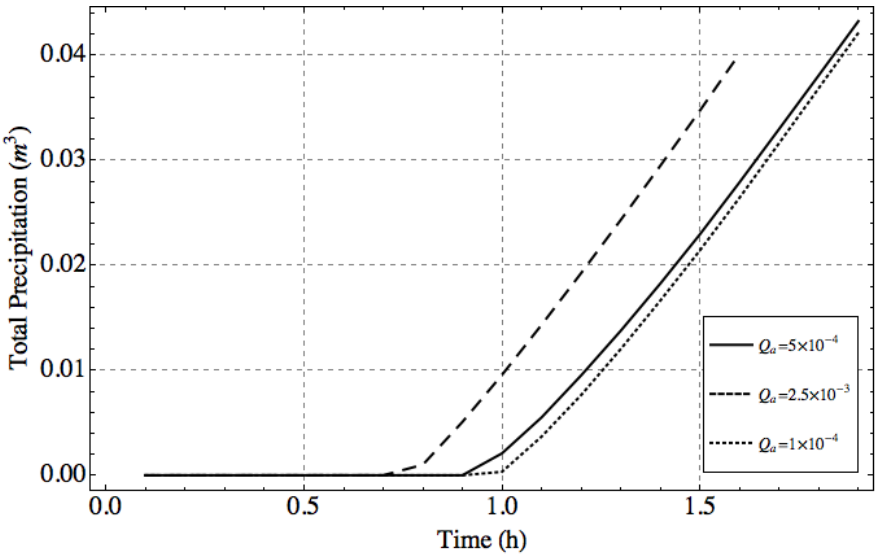

Figure 5.62: Total precipitation out of the water column until an ice cover forms.

Figure 5.63 shows the grease ice cover until the ice cover forms, and once again, following on from figure 5.62, ice is formed earlier in the higher humidity case, hence precipitating

and forming a grease ice cover first. The grease ice solid fraction is shown in figure 5.64, where we can see that the higher humidity case has a slower growth rate due to the lower heat loss at the surface. By this point, the effect of the initial delay is no longer felt since the grease ice is growing slower for the higher humidity case, and faster for the lower humidity case, as we expect.

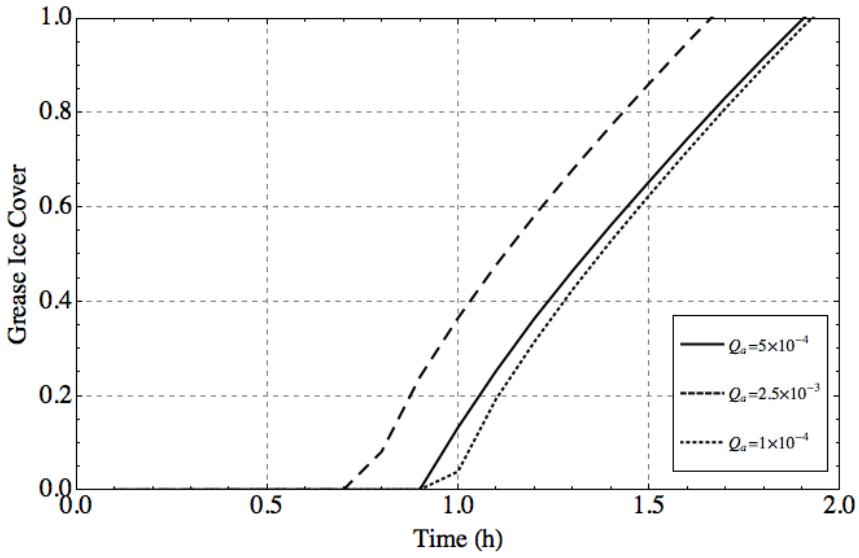

Figure 5.63: Grease ice cover until an ice cover forms.

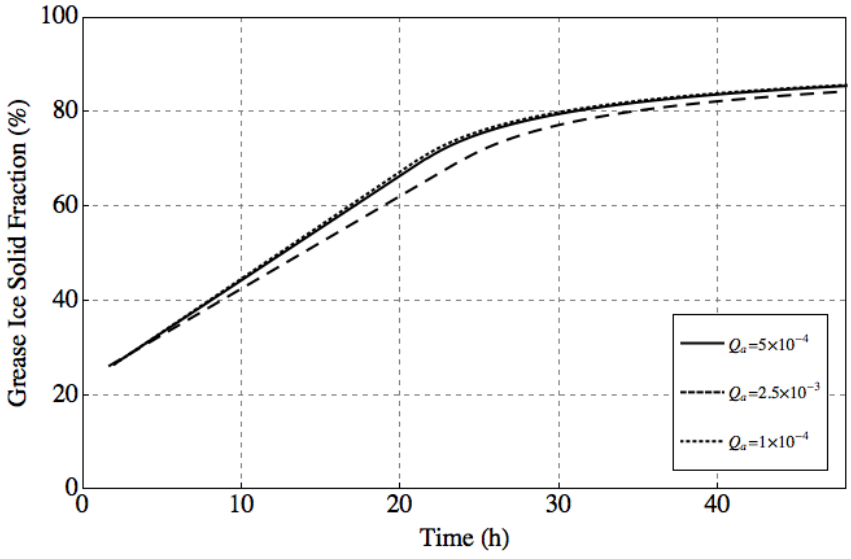

Figure 5.64: Grease ice solid fraction until two days of simulation.

The required 70% threshold in figure 5.64 to form an ice cover shows that the higher humidity case forms an ice cover last, which we can see in figure 5.65. This shows the total ice thickness until 48 hours. The growth rate is also lower as shown in figure 5.66, which means that after 48 hours, the higher humidity case ice thickness is considerably lower than the other two cases.

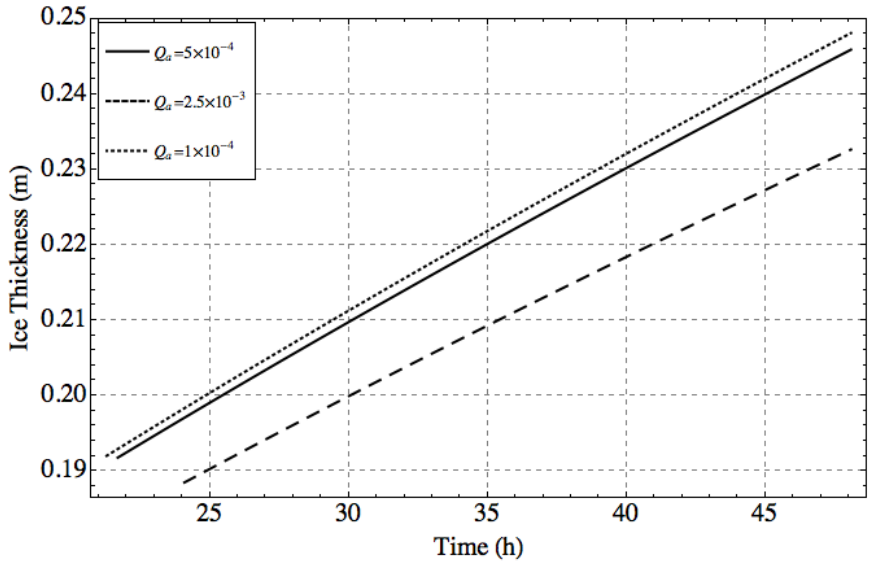

Figure 5.65: Total ice thickness until two days of simulation.

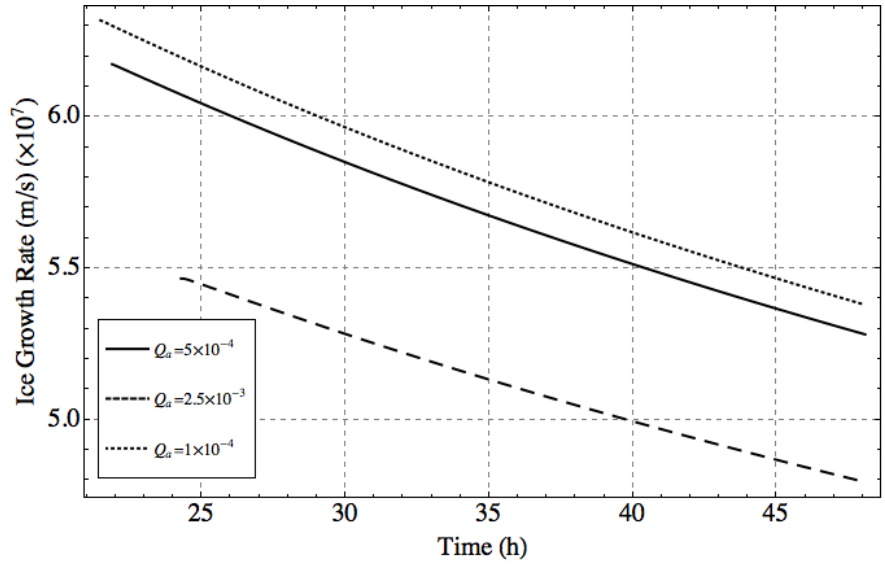

Figure 5.66: Ice growth rate until two days of simulation.

The brine channel formation starts in the higher humidity case later than the other two cases since the ice is thinner, and when it does, has a slower release rate, since it is thinner than the two other cases when it starts, as shown in figure 5.67. The total salt release by brine channels, shown in figure 5.68, happens faster in the higher humidity case, but, because it starts later, after 48 hours, the total salt released by the brine channels is still lower.

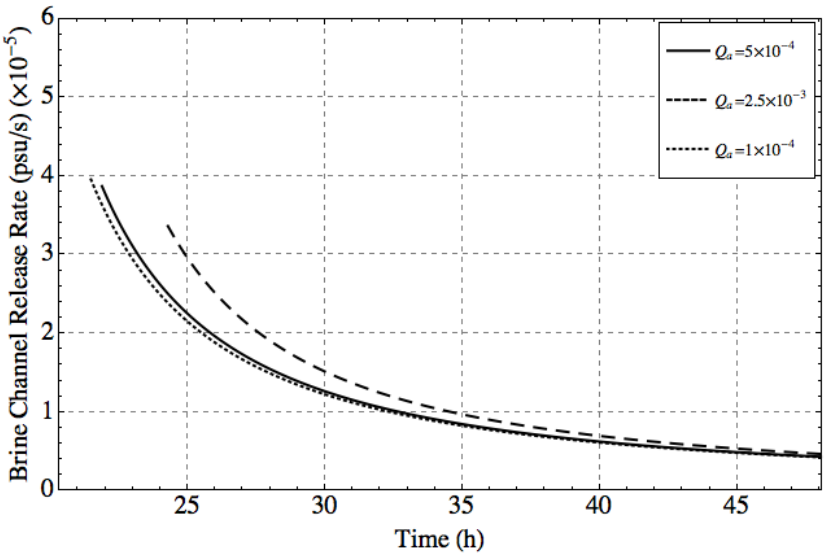

Figure 5.67: Brine channel release rate until two days of simulation.

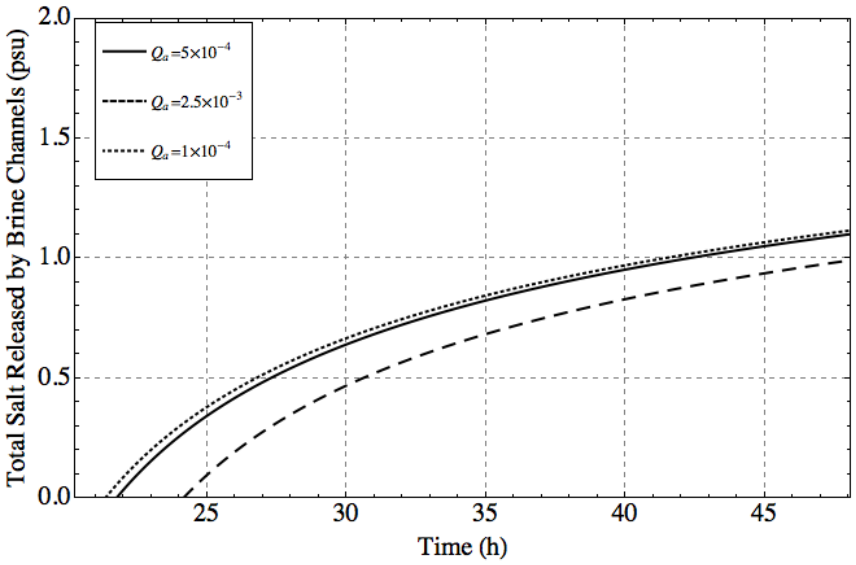

Figure 5.68: Total brine channel release until two days of simulation.

The rate of salt released by congelation ice is approximately constant for all three cases as shown in figure 5.69, with the higher humidity case with the lowest rate, since the growth rate is smaller. Since the higher humidity case starts later and has a smaller rate, again in figure 5.70, the total salt released by congelation ice is the smallest after 48 hours in that case.

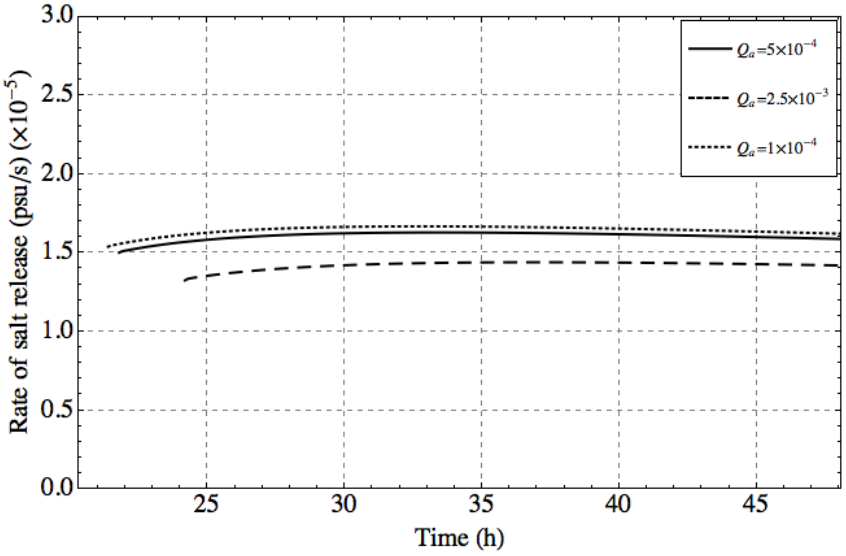

Figure 5.69: Rate of salt released from congelation ice until two days of simulation.

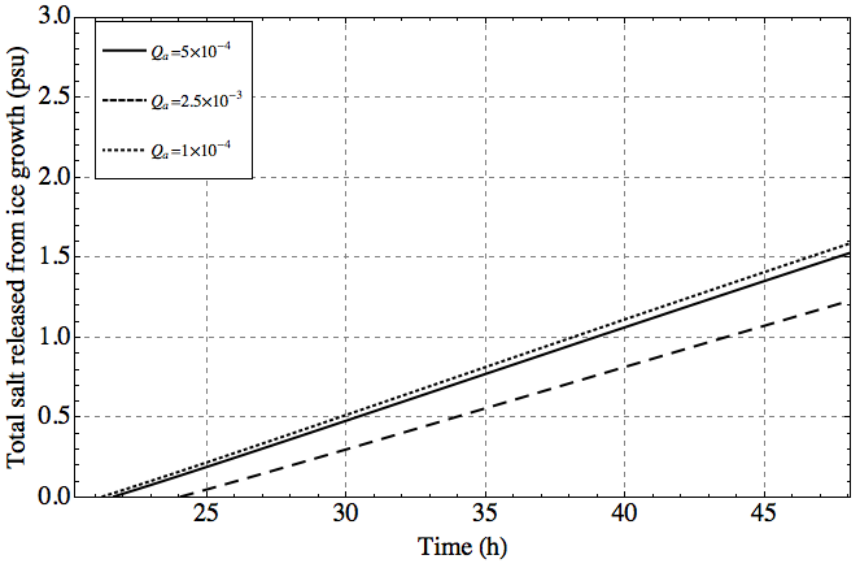

Figure 5.70: Total salt released from congelation ice formation until two days of simulation.

5.7 Summary

As shown by the majority of the sensitivity studies, ice does indeed grow faster during the frazil ice stage. This is because there is a lot more contact between the crystals and the water, and the heat loss at the open surface is so much greater. This in agreement with the theory that frazil ice formation is a major source of new ice, and demonstrates the impact leads and polynyas have on the polar regions.

We have explored a range of typical values of forcing choices and, although these are somewhat arbitrary, we can argue that wind speed seems to have the largest effect on the amount of ice formed, with the total ice thickness in the higher wind speed case more than double the total ice thickness in the lower wind speed case. This is because there are two mechanisms that are affected by wind speed. Firstly, higher wind speed increases the heat flux at the surface, which in turn leads to more ice creation. Secondly, higher wind speed creates a larger build-up of ice at the edge, or collection depth, and so forces the frazil ice formation stage to last longer, which, as already mentioned, increases the total amount of ice.

These seem to be two main processes which affect frazil ice formation, by the thermodynamics at the surface of the water, and by the collection depth at the edge. In this study, the thermodynamics was affected by wind speed, air temperature, longwave radiation and air humidity. The collection depth was affected by wind speed and lead width. Changing water salinity does not directly affect either of these processes, but as the study shows, varying it has little effect on the results.

To summarise, higher heat fluxes at the surface and a larger collection depth both increase the amount of ice created, and with wind speed affecting both of these, we conclude that frazil ice formation is more sensitive to wind speed variation that other typical variations in forcing.

6 Concluding Remarks

The aim of this PhD was to create a model of how frazil ice forms in the Arctic, specifically in leads and polynyas. By doing so, we wanted to check what effect frazil ice has on new ice formation in these areas, and what physical drivers affect the amount of ice formed. Looking at the bigger picture, we wanted to see if we could build a model which could be used in a GCM to more accurately predict frazil ice formation and hence the initial stages of sea ice formation. The motivation for this were studies which showed that sea ice formation was underestimated in GCMs and also that frazil ice formation accounts for a larger amount of new sea ice production than previously thought.

Our model was based on that of Holland & Feltham (H&F) (2005), which was of frazil ice formation under an ice shelf. The predictions of the H&F frazil dynamics model were in agreement with observations; the model itself was based on previous models such as Smedsrud & Jenkins (2004) and Jenkins & Bombosch (1995). We now briefly discuss the main changes and additions we made to H&F to create our model (the mathematical formulations are described in Chapter 2).

The first main change we made was the inclusion of salinity as a model variable. Since we are interested in the evolution of the sea ice after an ice cover has formed, salinity becomes an interesting variable due to the desalination of sea ice. During the initial frazil ice formation, as the crystals grow they release salt, affecting the ambient water salinity. We also consider in our model the mixed layer, which is the upper layer of the ocean which, due to stirring from waves/wind, has a relatively constant temperature and salinity. We allow the mixed layer bottom to move, which depends heavily on the temperature and salinity of the water.

With regards to the frazil crystal dynamics, we kept most of the assumptions from H&F as they had achieved results which appeared to be realistic. The frazil precipitation formulation was kept the same as H&F, even though we were now dealing with open water, since

the depth of the viscous layer used in H&F was within the bounds of that of an ice-ocean interface, and since the wind at the surface was already included elsewhere in the model. One area in which we made changes were the crystal rising velocities due to buoyancy. We used the study of Morse & Richard (2009) to investigate different parameterizations. These were later found to be wrong, and smaller than they should have been. The correct figures would have affected our results, since higher rising velocities would have forced an ice layer to form at the surface sooner. The qualitative results wouldn't have changed, but the overall times would have. The formulation for secondary nucleation was also altered.

Relative to the difference in the area we were modelling compared to H&F, the main difference is the upper boundary condition of our system. Since our water is in contact with the open atmosphere, the heat loss is a lot larger, and it is this heat loss which is the main contributing factor towards rapid ice formation. Since we were considering an Arctic winter scenario, we looked at an average air temperature of -25° C. This, compared to the average water temperature, near to freezing temperature of -2° C, means the heat loss to the air is large.

Once enough frazil ice has formed we depart from the model of H&F by letting a layer of grease ice form. To calculate at which point this happens, we looked at the study of Smedsrud (2011), which gives a parameterization of the collection depth, which is the maximum depth grease ice will collect to at the edge of a lead. Once enough ice has formed to create a full layer of ice at the collection depth, we treat the mixture as a granular layer, and we stop the frazil ice formation, allowing the escaping heat at the surface to increase the solid fraction of the granular ice layer until it reaches 90%, which is where we define the cut-off point, after which it becomes a solid ice layer. During this time, since more ice is forming in the granular layer, salt is being released into the surrounding water, which eventually leads to areas of very salty water known as brine pockets.

Once we have a solid layer of ice, the growth mechanism changes again and congelation ice starts to grow downwards, increasing the ice layer depth. We describe this growth

stage using the mushy layer equations. It is during this time that brine channels form, which carry salt water from brine pockets within the ice layer to the ocean beneath. This, together with salt being released solely from congelation ice growth, is responsible for the desalination of sea ice. This stage is important to model accurately, as salt being released from the ice layer lowers the bulk salinity of the ice, which in turn affects the growth rate of the ice. This is the last stage in our study, and concludes the initial stages of sea ice formation. All the model runs in our work simulate two days of real time, by which point they have all reached this last stage.

The ice formation model and equation solution procedures were built in stages into a Fortran 90 code, with the help of NAG (Numerical Algorithms Group) routines. (See Appendix for code). The first solutions we looked at in Chapter 3 were those of a well-mixed layer, where we simplified the problem by removing all space variables and consider a well-mixed box. This was also done in H&F, and was a necessary exercise to check whether our solving mechanism was accurate. Since the results were the same as H&F, we were confident in proceeding with the same method.

The next chapter, Chapter 4, saw us solve the full one dimensional model with all the formulations from chapter 2 included. This stage of the work was done in stages, adding new parameterizations and solving the full system to check the validity of the results. This took up the bulk of the work in the PhD since the programming sometimes became cumbersome, which required days of debugging at times. All throughout this process, one way we used to check if our results were realistic was to measure the total amounts of heat and salinity and check whether they had been conserved within the system.

Once the full model had been built and the solution procedures verified, we wanted to analyse the full results using a reference run. For this we needed realistic initial conditions and forcings for an Arctic winter scenario, obtained from the literature. It is this reference run which is shown in the second half of Chapter 4. All plots we thought were worth investigation are also included. Following on from this, we have a case study which uses

the full model solution and forcings from Dmitrenko el al (2010) to compare our model results to those observed in the paper. The results were found to be similar enough to believe our model is realistic.

In the next chapter, Chapter 5, we used the reference run from the previous chapter as a basis about which to conduct some sensitivity studies. We varied six different forcings/parameters in the model: wind speed, air temperature, water salinity, lead width, longwave radiation and air humidity. For each of these, we did a detailed analysis of the reference run and two runs, with a larger and lower value of the respective parameter. One issue we found whilst analysing the results was that the a_{nuc} parameter in the formulation we used for the secondary nucleation was too low. This caused, in some of the cases, a delay in the amount of time it took for ice to first start forming. To confirm that this was indeed due to the secondary nucleation parameter, we ran the same cases with a larger value of a_{nuc} and found the delay disappeared or was severely dampened in most cases. In the end, we decided to keep the original value, since it was the one we had used throughout the study, but we remained aware whilst analysing the results that the any 'delay' before the onset of strong secondary nucleation found in the results could possibly not be physical.

We now discuss the results of the model solution, the case studies and the sensitivity studies, and try to make some comments on the implications for frazil ice and sea ice modelling, their inclusion into GCMs, and future climate research.

One major conclusion which was made from the sensitivity studies was that the two main drivers of the amount of ice formed in the initial stages of sea ice formation are heat flux at the surface and the collection depth at the edge of the lead/polynya. The heat flux drive means that more heat being lost at the surface means more ice is formed, and the collection depth drive means that a larger collection depth implies the lead/polynya remains uncovered for longer and more ice is formed. From this we can see why the wind speed is the parameter the model is the most sensitive to, since increasing wind speed increases the heat flux and increases the collection depth, meaning the ice formation rate

is larger and it lasts for longer.

As mentioned in Chapter 1, current GCMs predictions of sea ice from year to year are not accurate e.g. they have underestimated the reduction in sea ice summer extent greatly. It's reasonable to assume that it is important to model frazil ice production accurately if we are to improve sea ice models. The complexity and uncertainty in frazil ice formation has lead to significant simplifications in models, and we hope that our study and future works will improve this.

Current global climate models underestimate the amount of sea ice which is of granular origin, which mostly is formed in leads and polynyas. We suggest that increasing the realism of lead/polynya refreezing in these models would improve this. Since GCMs use a spatial discrete grid, we could create a version of the model which would be valid only within a single unit of the grid. The main change would be how to model the collection depth at the edge of the lead/polynya, but we could use the direction of the wind to advect frazil ice into neighbouring grid elements. The parameters needed for the model (wind speed, heat fluxes, air temperature, water temperature, water salinity) are already present in climate models so could just be used to estimate the rate of frazil ice production.

With changing climate conditions, the average air temperature in the polar regions is expected to increase. This implies, as has been observed, that less ice will be present at the poles. In our model, similarly, if the winter air temperature increases, the heat flux at the surface will decrease and hence less ice will form. This is shown in the sensitivity study where we increase and decrease the air temperature. As shown in the sensitivity studies, the parameter the model is most sensitive to is wind speed. With changing climate conditions, it is possible that the average wind speed could decrease. Our model suggests that if this happens, less ice will form, and if the average air temperature is also increasing, there could be a compounding effect on the amount of ice formed. If our model were to be included in a GCM, we would therefore expect estimates of sea ice formation rates to decrease in the future, hence making modelled values closer to observed values.

As discussed in Chapter 1, sea ice affects the thermohaline circulation. One way in which this happens is by the formation of dense water, hence being denser, which sinks near the poles and travel equatorward. Frazil ice formation, by releasing salt into the ocean, accounts for a sizeable amount of dense water formed in the Antarctic. It is believed to be a major contributor to High Salinity Shelf Water (HSSW) in the Filchner-Ronne continental shelf. Our model suggests that under changing climate conditions less frazil ice may form in leads and polynyas, which will in turn lead to lower dense water formation rates. This is predicted to create a slowdown of the thermohaline circulation, which could lead to major consequences in the Earth's climate.

Granular ice of frazil origin is believed to be the most common type of ice found in the Antarctic (Weeks & Ackley 1986). As previously mentioned, current GCMs underestimate the amount of sea ice which is granular. We suggest that incorporating our model into global climate models would increase the amount of frazil ice that forms, hence increasing the amount of sea ice which is granular.

The main limitation of our model is that it is one-dimensional. Inclusion of horizontal dimensions would permit horizontal advection of scalars such as frazil ice, however the scaling analysis in chapter 2 show these terms to be negligible compared to the turbulent mixing. The most important feature to be captured by including a horizontal dimension is the wind-driven herding of frazil to collect as grease ice at the lead/polynya edge. Such an extension of our work would likely lead to new insight into the processes controlling the formation of new sea ice in leads and polynyas.

7 References

Arakawa, K. (1955), Studies of the freezing of water III, *J. Faculty of Science, Hokkaido University, Series 2, 4*, 355-357

Carstens, T. (1966), Experiments with supercooling and ice formation in flowing water, *Geofys. Publikasj., 26(9)*, 1-18

Daly, S. F. (1994), Frazil Ice Dynamics, *CRREL Spec. Rep. 94-23*, 19-24

Daly, S. F. Colbeck, S. C. (1986), Frazil ice measurements in CRREL's flume facility, *IAHR86, 8th International Symposium on Ice, 18-22 August 1986, Iowa City, Iowa. Proceedings*, Iowa City, IA, International Association for Hydraulic Research, 427-438

Dmitrenko, I. A., Wegner, C., Kassens, H. Kirillov, S. A., Krumpen, T., Heinemann, G., Helbig, A., Schroder, D., Holemann, J. A., Klagge, T., Tyshko, K. P. & Busche, T. (2010), Observations of supercooling and frazil ice formation in the Laptev Sea coastal polynyas, *Journal of Geophysical Research - Oceans, 115*, C05015

Dorn, W., Dethloff, K, Rink, A., Frickenhaus, S., Gerdes, R., Karcher, M. Kauker, F. (2007), Sensitivities and uncertainties in a coupled regional atmosphere-ocean-ice model with respect to the simulation of Arctic sea ice, *J. Geophys. Res., 112*, D10118

Ebert, E. & Curry, J. A. (1993), An intermediate one-dimensional thermodynamic sea ice model for investigating ice-atmosphere interactions, *J. Geophys. Res., 98*, 10085-10109

Feltham, D. L., Untersteiner, N., Wettlaufer, J. S. Worster, M. G. (2006), Sea ice is a mushy layer, *Geophys. Res. Lett., 33*, L14501

Fletcher, N. H. (1968), Ice nucleating behaviour of silver iodide smokes containing a

soluble content, *Journal of Atmospheric Sciences*, 25

Flocco D. & Feltham D. L. (2007), A continuum model of melt pond evolution on Arctic sea ice, *J. Geophysical Research, 112*, C08016

Gosink, J. P. & Osterkamp, T. (1986), Frazil ice nucleation by ejecta from supercooled water, *Proceedings, Internation Association for Hydraulic Research Symposium on Ice*

Holland, P. R. & Feltham, D. L. (2005), Frazil dynamics and precipitation in a water column with depth-dependent supercooling, *J. Fluid Mech, 530*, 101-124

Houghton, J. T., L. G. Meira Filho, B. Lim, K. Treanton, I. Mamaty, Y. Bonduki, D. J. Griggs & B. A. Callander (1997), Revised 1996 Guidelines for National Greenhouse Gas Inventories. IPCC/OECD/IEA

Jenkins, A. & Bombosch, A. (1995), Modelling the effects of frazil ice crystals on the dynamics and thermodynamics of Ice Shelf Water plumes, *J. Geophysical Research, 100*, 148-227

Kumai, M. & Itagaki, K. (1953), Cinematographic study of ice crystal formation in water, *J. Faculty of Science, Hokkaido University, Series 2, 4*, 235-246

Lepparanta, M. (1993), A review of analytical sea ice growth models, *Atmosphere-Ocean, 31*, 123-138

Lindow S. E., Arny, C. D., Upper, C. D. & Barchett W. R. (1978), The role of bacteria ice nuclei in frost injury to sensitive plants, *Plant Cold Hardiness and Freezing Stress-Mechanisms and Crop Implications, New York: Academic Press*, 249-263

Kivisild, H. R. (1970), River and lake ice terminology, *Proceedings of IAHR Symposium*

on Ice and Its Action on Hydraulic Structures, Paper 1.0

Maykut, G. A. (1982), Large-scale heat exchange and ice production in the central Arctic, *J. Geophysical Research: Oceans, 87*(C10), 7971-7984

Maykut, G. A. (1986), The surface heat and mass balance, *in Untersteiner, N. ed. The geophysics of sea ice.* New York, Plenum Press, 395-463

Miller P. A., Laxon S. W., Feltham D. L. & Cresswell D. J. (2006), Optimization of a Sea Ice Model Using Basinwide Observations of Arctic Sea Ice Thickness, Extent and Velocity, *J. Climate, 19*, 1089-1108

Morse, B. & Richard, M. (2009), A field study of suspended frazil ice particles, *Cold Regions Sci. and Tech., 55*, 86-102

Mossop, S. C. (1955), The Freezing of Supercooled Water, *Proc. Phys. Soc., B 68*, 193

Notz, D. & Worster, M. G. (2008), In situ measurements of the evolution of young sea ice, *J. Geophys. Res., 113*, C03001

Osterkamp, T. E., Benson, C. S., Gilfilian, R. E. & Ohtake, T. (1973), Winter history of an Alaska stream, *in Annual Report of the Geophysical Institute, University of Alaska, Fairbanks*

Osterkamp, T. E., Ohtake, T. & Warniment, D. C. (1974), Detection of airborne ice crystals near a supercooled stream, *Journal of Atmospheric Sciences*, 31

Smedsrud, L. H. & Jenkins, A. (2004), Frazil ice formation in an Ice Shelf Water plume, *J. Geophys. Res, 109*, C03025

Smedsrud, L. H. (2011), Grease ice thickness parameterization, *Annals of Glaciology, Volume 52, Issue 57*, 77-82

Stroeve, J., Holland, M. M., Meier, W., Scambos, T. & Serreze, M. (2007), Arctic sea ice decline: Faster than forecast, *Geophysical Research Letters, 34*

Svensson, U. & Omstedt, A. (1994), Simulation of super cooling and size distribution in frazil ice dynamics, *Cold Regions Science and Tech., 22*, 221-233

Svensson, U. & Omstedt, A. (1998), Numerical simulation of frazil ice dynamics in the upper layer of the ocean, *Cold Regions Science and Technology, 28*, 29-44

Toggweiler, J. R. & Key R. M. (2003), Ocean Circulation/Thermohaline Circulation, *Encyclopedia of Atmospheric Sciences, Vol. 4*, 1549-1555

Tsang, G. & Hanley, T. O. (1985), Frazil formation in water of different salinities and supercoolings, *Journal of Glaciology, Vol. 31, No. 108*, 74-85

Ushio, S & Wakatsuchi, M. (1993), A laboratory study on supercooling and frazil ice production processes in winter coastal polynyas, *J. Geophysical Research, 98*, 148-227

Vancoppenolle, M., Fichefet, T., Goosse, H., Bouillon, S., Madec, G. & Morales Maqueda, M. A. (2009), Simulating the mass balance and salinity of Arctic and Antarctic sea ice, *Ocean Modelling, 27*, 33-53

Vihma, T. & Haapala, J. (2009), Geophysics of sea ice in the Baltic Sea - a review, *Progress in Oceanography, 80*, 129-148

Wadhams, P., Lange, M. A. & Ackley, S. F. (1987), The ice thickness distribution across the Atlantic sector of the Antarctic Ocean in mid-winter, *Journal of Geophysical*

Research, 92(C13), 14,535-14,552

Wadhams, P., Wilkinson, J. P. & Wells, S. C. S. (1996), The European Subpolar Programme: Sea ice-ocean interaction, Scott Polar Res. Inst., Cambridge, UK

Weeks, W. F. & Ackley, S. F. (1986), The growth, structure and properties of sea ice, *The geophyics of sea ice, 146*, 9-164

Wells A. J., Wettlaufer, J. S. & Orszag, S. A. (2011), Brine fluxes from growing sea ice, Geophys. Res. Lett., Volume 38, Issue 4), L04501

Wettlaufer, J. S., Worster, M. G. & Huppert, H. E. (1997), The phase evolution of young sea ice, *Geophys. Res. Lett., 23*, 1251-1254

Willamson, R. B. & Chalmers, B. (1966), Morphology of ice solidified in undercooled water, *Crystal Growth (H.S. Peiser, Ed), New York: Pergamon Press*

Wu, J. (1984), Viscous Sublayer Below a Wind-Disturbed Surface, *Journal of Physical Oceanography, Vol. 14*, 138-144

Appendix A Program Code

We attach the source Fortran code that we wrote to solve the equations of our model, described in Chapter 4.

In this code, we first define all the variables and parameters of the model, including the independent variables of depth and time, and the dependent variables of concentration, temperature and salinity. The depth variable is defined as an array UX with 1001 points (defined as a depth of 100 m with 0.1 m step size). The dependent variables are defined in the form of a two-dimensional array UW(12,1001), where the first dimension are the 10 concentration size classes, the temperature and the salinity, and the second dimension are the 1001 depth points. We then populate the data array UW with the initial conditions, using functions and subroutines we have written for this.

We then define the equations that govern the system, including the boundary conditions. To simplify the solution procedure, we used numerical algorithms from the Numerical Algorithms Group (NAG), namely D03PCA and D03PZF, which are both used in solving systems of partial differential equations. To use the NAG routines, we must input into these subroutines the initial conditions array and parameters. The routines solve the system for one time step (1s in our case) and populate the dependent variable data array with the solution after that time step. This is then used as the initial condition in the next call to the NAG routine. By using a FOR loop we run the model for the required number of time steps (172,000 in our case), and solve the system for each one.

To output data from the model, we write the necessary data to external data files (the .dat files), which are then analysed separately. To do this, and since the amount of data is large, we only write the model solution every 360 times steps (i.e. 6 minutes of real time). This is resolution is sufficiently fine that over 2 days of run time, our solution curves are smooth.

```
PROGRAM FRAZIL_REF


IMPLICIT NONE


!WATER VARIABLES 1


INTEGER                      NPDEW, MW, NPTSW, INTPTSW, ITYPEW, NWW,
NIWW, ITASKW, ITRACEW, INDW, IUSERW(1), IWSAVW(505), IFAILW, NEQNW, NWKW


PARAMETER              (NPDEW=12, NPTSW=1001, INTPTSW=1001, ITYPEW=2,
NEQNW=NPDEW*NPTSW, NIWW=NEQNW+24, NWKW=(10+6*NPDEW)*NEQNW,
NWW=NWKW+(21+3*NPDEW)*NPDEW+7*NPTSW+54)

DOUBLE PRECISION       TSW, TOUTW, UW(NPDEW, NPTSW), UPW(NPDEW, INTPTSW,
ITYPEW), XW(NPTSW), XPW(INTPTSW), ACCW, WW(NWW), RUSERW(1), RWSAVW(1100)

DOUBLE PRECISION       UL(NPDEW, NPTSW), DUL(NPDEW, NPTSW)

INTEGER                      IWW(NIWW)

LOGICAL                      LWSAVW(100)

CHARACTER*80                 CWSAVW(10)

EXTERNAL               PDEDEFW, BNDARYW, UINITW



!WATER VARIABLES 2


INTEGER                      NPDEWW, MWW, NPTSWW, INTPTSWW, ITYPEWW,
NWWW, NIWWW, ITASKWW, ITRACEWW, INDWW, IUSERWW(1), IWSAVWW(505), IFAILWW,
NEQNWW, NWKWW

PARAMETER              (NPDEWW=2, NPTSWW=1001, INTPTSWW=1001, ITYPEWW=2,
NEQNWW=NPDEWW*NPTSWW, NIWWW=NEQNWW+24, NWKWW=(10+6*NPDEWW)*NEQNWW,
NWWW=NWKWW+(21+3*NPDEWW)*NPDEWW+7*NPTSWW+54)

DOUBLE PRECISION       TSWW, TOUTWW, UWW(NPDEWW, NPTSWW), UPWW(NPDEWW,
INTPTSWW, ITYPEWW), XWW(NPTSWW), XPWW(INTPTSWW), ACCWW, WWW(NWWW),
RUSERWW(1), RWSAVWW(1100)

DOUBLE PRECISION       ULW(NPDEWW, NPTSWW), DULW(NPDEWW, NPTSWW)

INTEGER                      IWWW(NIWWW)
```

```
LOGICAL                     LWSAVWW(100)

CHARACTER*80                CWSAVWW(10)

EXTERNAL              PDEDEFWW, BNDARYWW



!ICE VARIABLES


INTEGER                     NPDEI, MI, NPTSI, INTPTSI, ITYPEI, NWI,
NIWI, ITASKI, ITRACEI, INDI, IUSERI(1), IWSAVI(505), IFAILI, NEQNI, NWKI

PARAMETER             (NPDEI=1, NPTSI=201, INTPTSI=201, ITYPEI=2,
NEQNI=NPDEI*NPTSI, NIWI=NEQNI+24, NWKI=(10+6*NPDEI)*NEQNI,
NWI=NWKI+(21+3*NPDEI)*NPDEI+7*NPTSI+54)
DOUBLE PRECISION TSI, TOUTI, UI(NPDEI, NPTSI), UPI(NPDEI, INTPTSI,
ITYPEI), XI(NPTSI), XPI(INTPTSI), ACCI, WI(NWI), RUSERI(1), RWSAVI(1100)

INTEGER                     IWI(NIWI)

LOGICAL                     LWSAVI(100)

CHARACTER*80                CWSAVI(10)

EXTERNAL              PDEDEFI, BNDARYI, UINITI



!GENERAL VARIABLES


INTEGER                     I, IT, TSTEPS, COUNTER, AA, NNN, J

DOUBLE PRECISION      RAD(10), W(10), HW, HI, RHO(NPTSW), UII, BRINE,
T0, CBULK, UA, KT, PA, CA, LLEAD, VGRE

DOUBLE PRECISION      KICE, KEFF, KWAT, VT, P0, CP, COV, DH, DHDT, H,
T1, T2, TOTTIME, VTT, BS, BT, FLUXES, LL

PARAMETER             (TSTEPS=172800)

DOUBLE PRECISION      CTOT, DCTOT, PREC, PRECIP(10), TOTPRECIP, COVER,
INTERACTION, TF, PRECTOP, TEMP0, TOTBRINE, TOTSALT

EXTERNAL              D03PCA, D03PZF
```

```
COMMON /BLOCK1/             UL, DUL, COVER
COMMON /BLOCK2/             H, DH
COMMON /BLOCK3/             ULW, DULW
COMMON /BLOCK4/             UII
COMMON /BLOCK5/             TEMP0
COMMON /BLOCK6/             CBULK


!WATER PARAMETERS

MW=0
ACCW=1.0D-8
HW=0.1D0
TSW=0.0D0
TOUTW=1.0D0
ITRACEW=0
INDW=0
ITASKW=1


!WATER PARAMETERS 2

MWW=0
ACCWW=1.0D-8
ITRACEWW=0
INDWW=0
ITASKWW=1
```

```
!ICE PARAMETERS

MI=0

ACCI=1.0D-6

HI=0.0001D0

TSI=0.0D0

TOUTI=1.0D0

ITRACEI=0

INDI=0

ITASKI=1



!GENERAL PARAMETERS

COUNTER=0

COVER=0.0D0

TOTPRECIP=0.0D0

VT=1.0D-2

P0=1030.0D0

CP=3974.0D0

BS=7.86D-4

BT=3.87D-5

AA=0

CBULK=10.35D0

UA=5.0D0

KT=100.0D0

PA=1.4D0

CA=1.3D-3
```

```
LLEAD=150.0D0

VGRE=0.0D0

LL=3.35D5

TOTBRINE=0.0D0

TOTSALT=0.0D0



!CRYSTAL RADIUS AND RISE VELOCITIES


RAD=(/0.01D-3, 0.05D-3, 0.15D-3, 0.3D-3, 0.4D-3, 0.5D-3, 0.6D-3, 0.8D-3,
1.0D-3, 2.0D-3/)

W=(/3.56775D-6, 0.0000484646D0, 0.000287633D0, 0.000884725D0,
0.00141037D0, 0.002025D0, 0.00272131D0, 0.00422272D0, 0.005702D0,
0.012604D0/)



!OPEN DATA FILE


OPEN(30,file='1frazil.dat')

OPEN(31,file='1frazilice.dat')

OPEN(32,file='1frazilice2.dat')

OPEN(33,file='1frazilprec.dat')

OPEN(34,file='1fraziltc.dat')

OPEN(35,file='1frazilsalt.dat')

OPEN(36,file='1frazilbrine.dat')

OPEN(37,file='1frazilt0.dat')

OPEN(38,file='1frazilgrease.dat')

OPEN(39,file='1frazilcbulk.dat')
```

```
!SET DEPTH DATA POINTS

DO I=1,NPTSW
      XW(I)=(I-1)*HW
      XPW(I)=(I-1)*HW
      XWW(I)=(I-1)*HW
      XPWW(I)=(I-1)*HW
END DO

DO I=1,NPTSI
      XI(I)=(I-1)*HI
      XPI(I)=(I-1)*HI
END DO

!CALL INITIAL CONDITIONS

CALL UINITW(UW, XW, NPTSW)
CALL UINITI(UI, XI, NPTSI)

!WRITE INITIAL CONDITIONS

WRITE (30,*), UW(1:10,:)
WRITE (34,*), UW(11:12,:)
WRITE (31,*), UI(:,:)
WRITE (32,*), H, DH
```

```
WRITE (33,*), PRECTOP, TOTPRECIP

WRITE (38,*), VGRE

WRITE (39,*), CBULK


!START RUN



DO IT=1,TSTEPS

CALL CPU_TIME(T1)


      IF (COVER .LT. 1.0D0) THEN

            UL(:,:)=UW(:,:)

            DUL(:,:)=UPW(:,:,2)


            CTOT=0.0D0

            DCTOT=0.0D0


            DO I=1,NPDEW-2

                  CTOT=CTOT+UW(I,NPTSW)

                  DCTOT=DCTOT+UPW(I,NPTSW,2)

            END DO


            DO I=1,NPDEW-2

      PRECIP(I)=PREC(W(I),RAD(I),UW(I,NPTSW),UPW(I,NPTSW,2),CTOT,DCTOT,IN
TERACTION(I,RAD,W,UW(:,NPTSW),TF(100.0D0,UW(NPDEW,NPTSW))))

                  TOTPRECIP=TOTPRECIP-PRECIP(I)
```

```
            END DO


            PRECTOP=0.0D0

            DO I=1,NPDEW-2
                  PRECTOP=PRECTOP-PRECIP(I)
            END DO



      COVER=(((3.0D0/2.0D0)*((TOTPRECIP*LLEAD/0.25D0)/UA)*SQRT(KT/(PA*CA)
))**(2.0D0/3.0D0))/LLEAD


            VGRE=VGRE+PRECTOP-(FLUXES(UW(11,1001))*CP*COVER/LL)



            CALL D03PCA(NPDEW, MW, TSW, TOUTW, PDEDEFW, BNDARYW, UW,
NPTSW, XW, ACCW, WW, NWW, IWW, NIWW, ITASKW, ITRACEW, INDW, IUSERW,
RUSERW, CWSAVW, LWSAVW, IWSAVW, RWSAVW, IFAILW)

            CALL D03PZF(NPDEW, MW, UW, NPTSW, XW, XPW, INTPTSW, ITYPEW,
UPW,  IFAILW)


            TOUTW=TOUTW+1.0D0

            COUNTER=COUNTER+1


            IF(MOD(COUNTER,360) .EQ. 0) THEN

                  WRITE (30,*), UW(1:10,:)

                  WRITE (34,*), UW(11:12,:)

                  WRITE (31,*), UI(:,:)

                  WRITE (32,*), H, DH

                  WRITE (33,*), PRECTOP, TOTPRECIP

                  WRITE (38,*), VGRE
```

```
            WRITE (39,*), CBULK
      ELSE
      END IF

      PRINT*, "A"

ELSEIF (AA .EQ. 0) THEN

      UWW(:,:)=UW(11:12,:)
      UPWW(:,:,:)=UPW(11:12,:,:)

      TEMP0=-1.89365D0

      H=TOTPRECIP/0.25D0

      DO I=1,NPDEW-2
            DO J=1,NPTSW
                  H=H+0.1D0*UW(I,J)
            END DO
      END DO

      TSWW=TSW
      TOUTWW=TOUTW

      VGRE=VGRE-(FLUXES(UW(11,1001))*CP*COVER/LL)

      IF (VGRE/(4.0D0*TOTPRECIP) .GE. 0.7D0) THEN
            AA=AA+1
      ELSE
```

```
            END IF

            COUNTER=COUNTER+1

            IF(MOD(COUNTER,360) .EQ. 0) THEN

                  WRITE (34,*), UW(11:12,:)

                  WRITE (31,*), UI(:,:)

                  WRITE (32,*), H, DH

                  WRITE (33,*), PRECTOP, TOTPRECIP

                  WRITE (38,*), VGRE

                  WRITE (39,*), CBULK

            ELSE

            END IF


            PRINT*, VGRE*100/(4.0D0*TOTPRECIP)

            PRINT*, "B"

      ELSE


            ULW(:,:)=UWW(:,:)

            DULW(:,:)=UPWW(:,:,2)

            UII=UI(1,101)


            CALL D03PCA(NPDEWW, MWW, TSWW, TOUTWW, PDEDEFWW, BNDARYWW,
     UWW, NPTSWW, XWW, ACCWW, WWW, NWWW, IWWW, NIWWW, ITASKWW, ITRACEWW,
     INDWW, IUSERWW, RUSERWW, CWSAVWW, LWSAVWW, IWSAVWW, RWSAVWW, IFAILWW)
```

```
            CALL D03PZF(NPDEWW, MWW, UWW, NPTSWW, XWW, XPWW, INTPTSWW,
ITYPEWW, UPWW, IFAILWW)


            INDWW=0

            TOUTWW=TOUTWW+1.0D0



            DO I=1,NPTSW
                  RHO(I)=BS*UWW(2,I)-BT*UWW(1,I)
            END DO


            DO J=1,10000

                  NNN=0

                  DO I=1,NPTSW-1

                        IF (RHO(I+1) .GT. RHO(I)) THEN

                              UWW(1,I+1)=(UWW(1,I+1)+UWW(1,I))/2.0D0
                              UWW(1,I)=UWW(1,I+1)
                              UWW(2,I+1)=(UWW(2,I+1)+UWW(2,I))/2.0D0
                              UWW(2,I)=UWW(2,I+1)

                              RHO(I)=BS*UWW(2,I)-BT*UWW(1,I)
                              RHO(I+1)=BS*UWW(2,I+1)-BT*UWW(1,I+1)
                        ELSE
                              NNN=NNN+1
                        END IF
                  END DO
```

```
            IF (NNN .EQ. 1000) THEN
                  EXIT
            ELSE
            END IF

      END DO



      COVER=1.0D0

      CALL D03PCA(NPDEI, MI, TSI, TOUTI, PDEDEFI, BNDARYI, UI,
NPTSI, XI, ACCI, WI, NWI, IWI, NIWI, ITASKI, ITRACEI, INDI, IUSERI,
RUSERI, CWSAVI, LWSAVI, IWSAVI, RWSAVI, IFAILI)

      CALL D03PZF(NPDEI, MI, UI, NPTSI, XI, XPI, INTPTSI, ITYPEI,
UPI, IFAILI)

      TOUTI=TOUTI+1.0D0

      KICE=KEFF(271.256D0)

      KWAT=VT*P0*CP

      COV=1.0D0-CBULK/(34.5D0)

      DH=DHDT(H,UI(1,1),UWW(1,981),UWW(2,981))

      H=H+DH

      DO I=1,NPTSI
            XI(I)=(I-1)*(H/200.0D0)
            XPI(I)=(I-1)*(H/200.0D0)
      END DO

      BULK=CBULK-(BRINE(H,UII,CBULK)/H)
```

```
            TOTBRINE=TOTBRINE+BRINE(H,UII,CBULK)
            TOTSALT=TOTSALT+UWW(2,1001)*(1.0D0-(CBULK/34.5D0))*DH

            TEMP0=T0(DH,UWW(2,981))


            COUNTER=COUNTER+1


            IF(MOD(COUNTER,360) .EQ. 0) THEN
                  WRITE (34,*), UWW(:,:)
                  WRITE (31,*), UI(:,:)
                  WRITE (32,*), H, DH

                  WRITE(35,*), (1.0D0-(10.0D0/34.5D0))*DH*UWW(2,1001)
                  WRITE(36,*), BRINE(H,UII,CBULK)
                  WRITE(37,*), T0(DH,UWW(2,981))

                  WRITE (38,*), VGRE
                  WRITE (39,*), CBULK
            ELSE
            END IF
      END IF


CALL CPU_TIME(T2)


PRINT*, IT, COVER
      PRINT*, VGRE/(4.0D0*TOTPRECIP)
PRINT*, H, UII, CBULK
      PRINT*, BRINE(H, UII, CBULK)
```

```
PRINT*, TOTBRINE, TOTSALT
      PRINT*, "----------"


END DO


CALL CPU_TIME(T2)


PRINT*, "TOTAL TIME", T2


END PROGRAM



!---------- WATER EQUATIONS DEFINITIONS PART1----------


SUBROUTINE  PDEDEFW(NPDE, T, X, U, UX, P, Q, R, IRES, IUSER, RUSER)


INTEGER                      I, J, NPDE, IRES, IUSER(1)

DOUBLE PRECISION       T, X, U(NPDE), UX(NPDE), P(NPDE, NPDE), Q(NPDE),
R(NPDE), RUSER(1)

DOUBLE PRECISION       INTERACTION, TOTINTER, RAD(10), W(10), TF, PI, P0,
LL, C0, VT, VTT1, BS, BT

PARAMETER              (PI=920.0D0, P0=1030.0D0, LL=3.35D5, C0=3974.0D0,
VT=1.0D-2, BS=7.86D-4, BT=3.87D-5)



RAD=(/0.01D-3, 0.05D-3, 0.15D-3, 0.3D-3, 0.4D-3, 0.5D-3, 0.6D-3, 0.8D-3,
1.0D-3, 2.0D-3/)

W=(/3.56775D-6, 0.0000484646D0, 0.000287633D0, 0.000884725D0,
0.00141037D0, 0.002025D0, 0.00272131D0, 0.00422272D0, 0.005702D0,
0.012604D0/)



DO I=1,NPDE
```

```
      DO J=1,NPDE
            IF (I .EQ. J) THEN
                  P(I,J)=1.0D0
            ELSE
                  P(I,J)=0.0D0
            END IF
      END DO
END DO


TOTINTER=INTERACTION(1,RAD,W,U,TF(X,U(12)))+INTERACTION(2,RAD,W,U,TF(X,U(
12)))+INTERACTION(3,RAD,W,U,TF(X,U(12)))+INTERACTION(4,RAD,W,U,TF(X,U(12)
))+INTERACTION(5,RAD,W,U,TF(X,U(12)))+INTERACTION(6,RAD,W,U,TF(X,U(12)))+
INTERACTION(7,RAD,W,U,TF(X,U(12)))+INTERACTION(8,RAD,W,U,TF(X,U(12)))+INT
ERACTION(9,RAD,W,U,TF(X,U(12)))+INTERACTION(10,RAD,W,U,TF(X,U(12)))


DO I=1,10
      Q(I)=-INTERACTION(I,RAD,W,U(1:11),TF(X,U(12)))
END DO

Q(NPDE-1)=(PI/P0)*TOTINTER*(TF(X,U(12))-U(11)-(LL/C0))
Q(NPDE)=-(PI/P0)*TOTINTER*U(12)


DO I=1,10
      R(I)=VTT1(BS*UX(12)-BT*UX(11),X)*UX(I)-W(I)*U(I)
END DO

R(NPDE-1)=VTT1(BS*UX(12)-BT*UX(11),X)*UX(NPDE-1)
R(NPDE)=VTT1(BS*UX(12)-BT*UX(11),X)*UX(NPDE)


END SUBROUTINE
```

```
!---------- WATER EQUATIONS DEFININITIONS PART2----------


SUBROUTINE  PDEDEFWW(NPDE, T, X, U, UX, P, Q, R, IRES, IUSER, RUSER)


INTEGER                      I, J, NPDE, IRES, IUSER(1)

DOUBLE PRECISION       T, X, U(NPDE), UX(NPDE), P(NPDE, NPDE), Q(NPDE),
R(NPDE), RUSER(1)

DOUBLE PRECISION       INTERACTION, TOTINTER, RAD(10), W(10), TF, PI, P0,
LL, C0, VT, VTT2, BS, BT

PARAMETER              (PI=920.0D0, P0=1030.0D0, LL=3.35D5, C0=3974.0D0,
VT=1.0D-2, BS=7.86D-4, BT=3.87D-5)



DO I=1,2

      DO J=1,2

            IF (I .EQ. J) THEN

                  P(I,J)=1.0D0

            ELSE

                  P(I,J)=0.0D0

            END IF

      END DO

END DO


Q(1)=0.0D0

Q(2)=0.0D0


R(1)=VTT2(BS*UX(2)-BT*UX(1),X)*UX(1)
R(2)=VTT2(BS*UX(2)-BT*UX(1),X)*UX(2)
```

```
END SUBROUTINE



!---------- ICE EQUATION DEFINITION ----------

SUBROUTINE PDEDEFI(NPDE, T, X, U, UX, P, Q, R, IRES)

INTEGER                      NPDE, IRES

DOUBLE PRECISION       T, X, U(NPDE), UX(NPDE), P(NPDE,NPDE), Q(NPDE),
R(NPDE), CEFF, KEFF

P(1,1)=CEFF(U(1)+273.15D0)

Q(1)=0.0D0

R(1)=KEFF(U(1)+273.15D0)*UX(1)

END SUBROUTINE

!---------- WATER BOUNDARY CONDITIONS ----------

SUBROUTINE  BNDARYW(NPDE, T, U, UX, IBND, BETA, GAMMA, IRES, IUSER,
RUSER)

INTEGER                      I, NPDE, NPTS, IBND, IRES, IUSER(1), NPDEW

PARAMETER              (NPTS=1001, NPDEW=12)

DOUBLE PRECISION T, U(NPDE), UX(NPDE), BETA(NPDE), GAMMA(NPDE), RUSER(1)
```

```
DOUBLE PRECISION UL(NPDEW, NPTS), DUL(NPDEW,NPTS), RAD(10), W(10),
INTERACTION, TF, CTOT, DCTOT, VT

DOUBLE PRECISION PREC, FLUXES, COVER, VTT, BS, BT, COV, H, DH

PARAMETER              (VT=1.0D-2, BS=7.86D-4, BT=3.87D-5)


COMMON /BLOCK1/        UL, DUL, COVER

COMMON /BLOCK2/        H, DH

COMMON /BLOCK6/        CBULK

COV=1.0D0-(CBULK/34.5D0)



RAD=(/0.01D-3, 0.05D-3, 0.15D-3, 0.3D-3, 0.4D-3, 0.5D-3, 0.6D-3, 0.8D-3,
1.0D-3, 2.0D-3/)

W=(/3.56775D-6, 0.0000484646D0, 0.000287633D0, 0.000884725D0,
0.00141037D0, 0.002025D0, 0.00272131D0, 0.00422272D0, 0.005702D0,
0.012604D0/)



CTOT=UL(1,NPTS)+UL(2,NPTS)+UL(3,NPTS)+UL(4,NPTS)+UL(5,NPTS)+UL(6,NPTS)+UL
(7,NPTS)+UL(8,NPTS)+UL(9,NPTS)+UL(10,NPTS)

DCTOT=DUL(1,NPTS)+DUL(2,NPTS)+DUL(3,NPTS)+DUL(4,NPTS)+DUL(5,NPTS)+DUL(6,N
PTS)+DUL(7,NPTS)+DUL(8,NPTS)+DUL(9,NPTS)+DUL(10,NPTS)



IF (IBND .EQ. 0) THEN


      DO I=1,NPDE

            BETA(I)=1.0D0

            GAMMA(I)=0.0D0

      END DO

ELSE

      DO I=1,NPDE-2

            BETA(I)=0.0D0

            GAMMA(I)=(-U(I)+UL(I,NPTS))+(W(I)*UL(I,NPTS)-
VT*DUL(I,NPTS)+INTERACTION(I,RAD,W,UL(:,NPTS),TF(100.0D0,UL(NPDEW,NPTS)))
```

```
+PREC(W(I),RAD(I),UL(I,NPTS),DUL(I,NPTS),CTOT,DCTOT,INTERACTION(I,RAD,W,U
L(:,NPTS),TF(100.0D0,UL(NPDEW,NPTS)))))

      END DO


      BETA(NPDE-1)=1.0D0

      GAMMA(NPDE-1)=(1.0D0-COVER)*FLUXES(UL(11,1001))

      BETA(NPDE)=1.0D0

      GAMMA(NPDE)=0.0D0


END IF



END SUBROUTINE



!---------- WATER BOUNDARY CONDITIONS 2 ----------


SUBROUTINE  BNDARYWW(NPDE, T, U, UX, IBND, BETA, GAMMA, IRES, IUSER,
RUSER)


INTEGER                      I, NPDE, NPTS, IBND, IRES, IUSER(1), NPDEW

PARAMETER              (NPTS=1001, NPDEW=2)

DOUBLE PRECISION T, U(NPDE), UX(NPDE), BETA(NPDE), GAMMA(NPDE), RUSER(1)

DOUBLE PRECISION UL(NPDEW, NPTS), DUL(NPDEW,NPTS), INTERACTION, TF, CTOT,
DCTOT, VT

DOUBLE PRECISION PREC, FLUXES, COVER, VTT, BS, BT, COV, H, DH, BRINE,
TEMP0, CBULK

PARAMETER              (VT=1.0D-2, BS=7.86D-4, BT=3.87D-5)

COMMON /BLOCK3/        UL, DUL

COMMON /BLOCK2/        H, DH

COMMON /BLOCK4/        UII
```

```
COMMON /BLOCK5/        TEMP0
COMMON /BLOCK6/        CBULK

COV=1.0D0-(CBULK/34.5D0)

IF    (IBND .EQ. 0) THEN
      BETA(1)=1.0D0
      GAMMA(1)=0.0D0
      BETA(2)=1.0D0
      GAMMA(2)=0.0D0
ELSE
      BETA(1)=0.0D0
      GAMMA(1)=U(1)-TEMP0
      BETA(2)=1.0D0
      GAMMA(2)=U(2)*COV*DH+BRINE(H,UII,CBULK)
END IF

END SUBROUTINE



!---------- ICE BOUNDARY CONDITIONS ----------

SUBROUTINE BNDARYI(NPDE, T, U, UX, IBND, BETA, GAMMA, IRES)

INTEGER                      NPDE, IBND, IRES
DOUBLE PRECISION T, U(NPDE), UX(NPDE), BETA(NPDE), GAMMA(NPDE)
DOUBLE PRECISION PI, CPI, FLW, EPSILON, SIGMA, KEL, FSENSI, FLATI, KICE,
H, KEFF, TEMP0
```

```
PARAMETER              (FLW=168.3D0, EPSILON=0.99D0, SIGMA=5.67D-8,
KEL=273.15D0, PI=917.0D0, CPI=2050.0D0, KICE=1.0D-6)

COMMON /BLOCK2/        H

COMMON /BLOCK5/        TEMP0



IF (IBND .EQ. 0) THEN

      BETA(1)=0.0D0

      GAMMA(1)=KEFF(U(1)+273.15D0)*(U(1)+1.89365D0)/H-(EPSILON*(FLW-
SIGMA*((U(1)+KEL)**4.0D0))+FSENSI(U(1)+KEL)+FLATI(U(1)+KEL))

ELSE

      BETA(1)=0.0D0

      GAMMA(1)=U(1)-TEMP0

END IF



END SUBROUTINE




!---------- WATER INITIAL CONDITIONS ----------



SUBROUTINE  UINITW(U, X, NPTS)



INTEGER                      I, J, NPTS, NPDE

PARAMETER              (NPDE=12)

DOUBLE PRECISION X(NPTS), U(NPDE, NPTS)



DO J=1,NPTS

      DO I=1,NPDE-2

            U(I,J)=4.0D-9*(1.0D0-((ERF(90.0D0-X(J))+1.0D0)/2.0D0))
```

```
      END DO

      U(NPDE-1,J)=-1.89365D0+0.001D0*(100.0D0-X(J))+((ERF(90.0D0-
X(J))+1.0D0)/2.0D0)

      U(NPDE,J)=34.5D0+0.01D0*(100.0D0-X(J))+((ERF(90.0D0-
X(J))+1.0D0)/2.0D0)

END DO


END SUBROUTINE




!---------- ICE INITIAL CONDITIONS ----------


SUBROUTINE UINITI(U, X, NPTS)


INTEGER                      NPTS, I

DOUBLE PRECISION U(1, NPTS), X(NPTS)


DO I=1,NPTS

      U(1,I)=-1.89365D0

END DO


END SUBROUTINE







! INTERACTION TERMS
```

```
!----------CRYSTAL INTERACTION TERM----------


FUNCTION INTERACTION(I,R,W,U,TF)


INTEGER                       I, N, NPDE

PARAMETER               (N=10, NPDE=12)

DOUBLE PRECISION INTERACTION, GROWTH, MELT, NUCLEATION, R(N), W(N),
U(N+1), H, TF, HE,

CT

H=HE(TF-U(N+1))


CT=U(1)+U(2)+U(3)+U(4)+U(5)+U(6)+U(7)+U(8)+U(9)+U(10)



IF (I .EQ. 1) THEN

      INTERACTION=(1.0D0-H)*MELT(R(I),U(I),U(N+1),TF)-
(R(I)**3/(R(I+1)**3-R(I)**3))*((1.0D0-
H)*MELT(R(I+1),U(I+1),U(N+1),TF)+H*GROWTH(R(I),U(I),U(N+1),TF))-
NUCLEATION(R(2),W(2),U(2),CT)-NUCLEATION(R(3),W(3),U(3),CT)-
NUCLEATION(R(4),W(4),U(4),CT)-NUCLEATION(R(5),W(5),U(5),CT)-
NUCLEATION(R(6),W(6),U(6),CT)-NUCLEATION(R(7),W(7),U(7),CT)-
NUCLEATION(R(8),W(8),U(8),CT)-NUCLEATION(R(9),W(9),U(9),CT)-
NUCLEATION(R(10),W(10),U(10),CT)

ELSE IF (I .EQ. 10) THEN

      INTERACTION=(R(I)**3/(R(I)**3-R(I-1)**3))*((1.0D0-
H)*MELT(R(I),U(I),U(N+1),TF)+H*GROWTH(R(I-1),U(I-
1),U(N+1),TF))+NUCLEATION(R(I),W(I),U(I),CT)

ELSE

      INTERACTION=(R(I)**3/(R(I)**3-R(I-1)**3))*((1.0D0-
H)*MELT(R(I),U(I),U(N+1),TF)+H*GROWTH(R(I-1),U(I-1),U(N+1),TF))-
(R(I)**3/(R(I+1)**3-R(I)**3))*((1.0D0-
H)*MELT(R(I+1),U(I+1),U(N+1),TF)+H*GROWTH(R(I),U(I),U(N+1),TF))+NUCLEATIO
N(R(I),W(I),U(I),CT)

END IF
```

```
END FUNCTION


!----------CRYSTAL GROWTH TERM----------

FUNCTION GROWTH(R,C,T,TF)
DOUBLE PRECISION GROWTH, R, C, T, TF, C0, NU, KT, LL
PARAMETER              (C0=3974.0D0, NU=1.0D0, KT=1.4D-7, LL=3.35D5)

GROWTH=(C0*NU*KT/LL)*(TF-T)*(2.0D0/(R**2.0D0))*C

END FUNCTION


!----------CRYSTAL MELTING TERM----------

FUNCTION MELT(R,C,T,TF)

DOUBLE PRECISION MELT, R, C, T, TF, C0, NU, KT, LL
PARAMETER              (C0=3974.0D0, NU=1.0D0, KT=1.4D-7, LL=3.35D5)

MELT=(C0*NU*KT/LL)*(TF-T)*(52.0D0/(R**2.0D0))*C

END FUNCTION
```

```
!----------SECONDARY NUCLEATION----------


FUNCTION NUCLEATION(R,W,C,CT)


DOUBLE PRECISION NUCLEATION, R, W, C, CT, RE, AR, EP, V0, WI, ANUC


PARAMETER              (EP=7.4D-7, V0=1.95D-6, AR=0.02D0, ANUC=1.0D-6)


RE=R*((3.0D0*AR/2.0D0)**(1.0D0/3.0D0))
WI=SQRT((4.0D0*EP/(15.0D0*V0))*(RE**2.0D0)+(W**2.0D0))

NUCLEATION=-ANUC*C*WI*CT/RE


END FUNCTION



!---------- FREEZING TEMPERATURE ----------


FUNCTION TF(X,S)


DOUBLE PRECISION TF, X, S, BS, BT, T0

PARAMETER              (T0=0.0832D0, BS=-0.0573D0, BT=-7.61D-4)


TF=T0+S*BS+(100.0D0-X)*BT


END FUNCTION



!---------- HEAVISIDE FUNCTION ----------
```

```
FUNCTION    HE(X)


DOUBLE PRECISION HE, X


IF (X .LE. 0.0D0) THEN

      HE=0.0D0

ELSE

      HE=1.0D0

END IF


END FUNCTION







! PRECIPITATION TERMS



!----------PRECIPITATION TERM----------


FUNCTION PREC(W,R,C,DCDZ,CT,DCTDZ,S)


DOUBLE PRECISION PREC, TPREC, LPREC, RICH, W, C, R, DCDZ, S, D, RIC, CT,
DCTDZ

PARAMETER              (D=8.0D0, RIC=0.25D0)


PREC=TPREC(W,C,R)+((LPREC(W,C,DCDZ,S)-
TPREC(W,C,R))/2.0D0)*(1+ERF(D*(RICH(CT,DCTDZ)-RIC)))
```

```
END FUNCTION



!----------TURBULENT PRECIPITATION----------


FUNCTION TPREC(W,C,R)


DOUBLE PRECISION TPREC, P0, PI, G, R, RE, CD, W, C, U, UT, HE, AR

PARAMETER              (P0=1030.0D0, PI=920.0D0, G=9.81D0, CD=1.5D-3,
UT=0.06D0, U=0.055D0, AR=0.02D0)


RE=R*(3.0D0*AR/2.0D0)**(1.0D0/3.0D0)

UCI2=0.05D0*(P0-PI)*G*2.0D0*RE/(P0*CD)

TPREC=-W*C*(1-((U**2.0D0+UT**2.0D0)/UCI2))*HE(1-
((U**2.0D0+UT**2.0D0)/UCI2))


END FUNCTION



!----------LAMINAR PRECIPITATION----------


FUNCTION LPREC(W,C,DCDZ,S)


DOUBLE PRECISION LPREC, W, C, VT, DCDZ, S, HE

PARAMETER              (VT=1.0D-2)


LPREC=(-W*C+VT*DCDZ-S)*HE(-(-W*C+VT*DCDZ-S))
```

```
END FUNCTION



!----------RICHARDSON NUMBER----------


FUNCTION RICH(C,DCDZ)


DOUBLE PRECISION RICH, G, V, C, PM, P0, PI, V0, DCDZ, CD, U, K

PARAMETER              (G=9.81D0, P0=1030.0D0, PI=920.0D0, V0=1.95D-6,
CD=1.5D-3, U=0.055D0, K=0.41D0)

V=((0.02D0-V0)/0.47D0)*C+V0


PM=P0+C*(PI-P0)


RICH=-((G*(V**2.0D0))/(PM*(V0**2.0D0)))*((PI-
P0)*DCDZ)*((35.0D0*V0*K/(CD*(U**2.0D0)))**2.0D0)


END FUNCTION







! WATER SURFACE HEAT FLUXES


!----------HEAT FLUXES WATER---------


FUNCTION FLUXES(T0)
```

```
DOUBLE PRECISION FLUXES, FLW, EPS, SIG, T0, KEL, FSENSW, FLATW, P0, CP

PARAMETER              (FLW=168.3D0, EPS=0.99D0, SIG=5.67D-8,
KEL=273.15D0, P0=1030.0D0, CP=3974.0D0)


FLUXES=(EPS*(FLW-SIG*((T0+KEL)**4.0D0))+FSENSW(T0)+FLATW(T0))/(P0*CP)


END FUNCTION




!----------WATER LATENT HEAT---------


FUNCTION FLATW(T0)


DOUBLE PRECISION FLATW, T0, PA, LL, CT, VV, QV, PATM, PV, RV, PAT, QAT,
KEL

PARAMETER              (PA=1.275D0, LL=2.501D6, CT=1.235D-3, VV=5.0D0,
PATM=1013.25D0, RV=461.7D0, KEL=273.15D0)


PV=6.112*EXP((LL/RV)*((1.0D0/273.1D0) - (1.0D0/(T0+KEL))))

PAT=6.112*EXP((LL/RV)*((1.0D0/273.1D0) - (1.0D0/248.7)))


QV=0.622D0*PV/(PATM-0.387D0*PV)

QAT=0.622D0*PAT/(PATM-0.387D0*PAT)


FLATW=PA*LL*CT*VV*(QAT-QV)


END FUNCTION
```

```
!----------WATER SENSIBLE HEAT----------


FUNCTION FSENSW(T0)


DOUBLE PRECISION FSENSW, PA, CA, CT, VV, TA, T0, KEL

PARAMETER              (PA=1.275D0, CA=1005.0D0, CT=1.235D-3, VV=5.0D0,
TA=248.7D0, KEL=273.15D0)


FSENSW=PA*CA*CT*VV*(TA-(T0+KEL))


END FUNCTION







! SPECIFIC HEAT CAPACITY AND CONDUCTIVITY


!----------VOLUMETRIC SPECIFIC HEAT----------


FUNCTION CEFF(T)


DOUBLE PRECISION CEFF, T, TFR, LL, CBULK, CI, CEFFB, CEFFI

PARAMETER              (LL=3.35D5, CBULK=20.0D0, CI=0.0D0,
CEFFB=4.08572D6, CEFFI=1.87985D6)


CEFF=CEFFI-LL*((TFR(CBULK)-TFR(CI))/((T-TFR(0.0D0))**2.0D0))


END FUNCTION
```

```
!----------LIQUIDUS CURVE----------


FUNCTION TFR(C)

DOUBLE PRECISION TFR, C, GAMMA, T0

PARAMETER              (GAMMA=0.0573D0, T0=273.15D0)

TFR=T0-C*GAMMA

END FUNCTION



!----------CONDUCTIVITY----------


FUNCTION KEFF(T)

DOUBLE PRECISION KEFF, T, TFR, CI, CBULK, KI, KBI, KB, KA, VA

PARAMETER              (CI=0.0D0, CBULK=20.0D0, KA=0.03D0, VA=0.025D0)

KI=1.16D0*(1.91D0-8.66D-3*(T-TFR(0.0D0))+2.97D-5*((T-TFR(0.0D0))**2.0D0))

KBI=((2.0D0*KI+KA-2*VA*(KI-KA))/(2.0D0*KI+KA+VA*(KI-KA)))*KI

KB=0.4184D0*(1.25D0+0.03D0*(T-TFR(0.0D0))+0.00014D0*((T-
TFR(0.0D0))**2.0D0))

KEFF=KBI-(KBI-KB)*((TFR(CBULK)-TFR(CI))/(T-TFR(0.0D0)))

END FUNCTION
```

```
! STEFAN CONDITION


!----------STEFAN CONDITION----------


FUNCTION DHDT(H,TS,TINF,SINF)


DOUBLE PRECISION DHDT, H, TS, TINF, SINF

DOUBLE PRECISION A, B, C, D, E, F, AA, BB, CC

DOUBLE PRECISION RHO, LL, PHI, UU, KI, AH, TREF, AS, DEL, CP

PARAMETER              (RHO=1028.0D0, LL=3.35D5, UU=0.015D0, KI=2.0D0,
AH=0.0058D0, TREF=0.0832D0, AS=2.0D-4, DEL=0.054D0, CP=3974.0D0)

PHI=1.0D0-(10.0D0/34.5D0)


A=PHI*RHO*LL

B=KI

C=RHO*CP*AH*UU

D=PHI

E=AS*UU

F=DEL


AA=-A*D*H


BB=A*E*H+B*D*TREF-B*D*TS-C*D*TINF*H+C*D*H*TREF


CC=-B*E*TREF+F*E*B*SINF+B*E*TS+C*E*TINF*H-C*E*TREF*H+C*E*F*SINF*H


DHDT=(-BB+SQRT(BB*BB-4.0D0*AA*CC))/(2.0D0*AA)
```

```
END FUNCTION




!----------INTERFACE TEMPERATURE


FUNCTION T0(DH,SINF)


DOUBLE PRECISION T0, DH, SINF, TREF, AS, UU, PHI, DEL
PARAMETER              (TREF=0.0832D0, AS=2.0D-4, UU=0.015D0,
DEL=0.054D0)


PHI=0.7D0

T0=TREF-((DEL*AS*UU*SINF)/(AS*UU-PHI*DH))


END FUNCTION







! ICE HEAT FLUXES


!---------ICE TRANSFER COEFFICIENT---------


FUNCTION CTI(T)
```

```
DOUBLE PRECISION CTI, T, CT0, B, C, RI, DZ, UA, G, TA

PARAMETER              (CT0=1.3D-3, B=20.0D0, DZ=10.0D0, UA=5.0D0,
G=9.81D0, TA=248.7D0)


C=1961.0D0*B*CT0


RI=G*(TA-T)*DZ/(TA*UA**2)


CTI=CT0*(1.0D0-((2.0D0*B*RI)/(1.0D0+C*(DABS(RI)**(0.5D0)))))


END FUNCTION



!----------ICE SENSIBLE HEAT----------


FUNCTION FSENSI(T)


DOUBLE PRECISION FSENSI, T, PA, CA, CTI, VV, TA

PARAMETER              (PA=1.275D0, CA=1005.0D0, VV=5.0D0, TA=248.7D0)


FSENSI=PA*CA*CTI(T)*VV*(TA-T)

END FUNCTION




!----------ICE LATENT HEAT----------


FUNCTION FLATI(T)


DOUBLE PRECISION FLATI, T, PA, LL, CTI, VV, QV, PATM, PV, RV, PAT, QAT

PARAMETER              (PA=1.275D0, LL=2.501D6, VV=5.0D0, PATM=1013.25,
RV=461.7)


PV=6.112*EXP((LL/RV)*((1.0D0/273.1D0) - (1.0D0/T)))
```

```
PAT=6.112*EXP((LL/RV)*((1.0D0/273.1D0) - (1.0D0/248.7)))

QV=0.622D0*PV/(PATM-0.387D0*PV)

QAT=0.622D0*PAT/(PATM-0.387D0*PAT)

FLATI=PA*LL*CTI(T)*VV*(QAT-QV)

END FUNCTION




! DEPTH DEPENDENT TURBULENT DIFFUSIVITY


!----------DEPTH DEPENDENT TURBULENT DIFFUSIVITY 1----------

FUNCTION VTT1(Z,X)

DOUBLE PRECISION VTT1, X, ERF, Z

IF (X .LE. 90.0D0) THEN
      VTT1=1.0D-4+0.9999D0*((ERF(1.0D8*Z)+1.0D0)/2.0D0)
ELSE
      VTT1=1.0D-2+0.9999D0*((ERF(1.0D8*Z)+1.0D0)/2.0D0)
END IF

END FUNCTION
```

```
!----------DEPTH DEPENDENT TURBULENT DIFFUSIVITY 2----------


FUNCTION VTT2(Z,X)


DOUBLE PRECISION VTT2, X, ERF, Z


IF (X .LE. 90.0D0) THEN

      VTT2=1.0D-4

ELSE

      VTT2=1.0D-2

END IF


END FUNCTION


!     BRINE CHANNELS FORMATION


!----------BRINE CHANNELS----------


FUNCTION BRINE(H,T,CBULK)


DOUBLE PRECISION BRINE, H, T, CBULK

DOUBLE PRECISION RM, RC, RHO, G, B, CE, C0, PI, NU, K, GAMMA, ALPHA, CS,
PHI

PARAMETER              (RC=10.0D0, RHO=1028.0D0, G=9.81D0, B=7.86D-4,
C0=34.5D0, NU=1.787D-3, K=1.4D-7, ALPHA=0.023D0)
```

```
CE=T/-0.0573D0

CS=C0/(CE-C0)

GAMMA=ALPHA*CS


PHI=1.0D0-(CBULK/C0)


PI=3.0D-8*((1.0D0-PHI)**3.0D0)


RM=RHO*G*B*(CE-C0)*PI*(H/2.0D0)/(NU*K)


IF (RM .LE. RC) THEN
      BRINE=0.0D0
ELSE
      BRINE=GAMMA*RHO*B*((CE-C0)*(CE-C0))*PI*(RM-RC)/(NU*RM)
END IF


END FUNCTION
```